Towards a
Six Degree-of-Freedom Resistive Force Sensor
device design and bonding technique

Simon Reuvekamp
Transducer Science and Technology
University of Twente

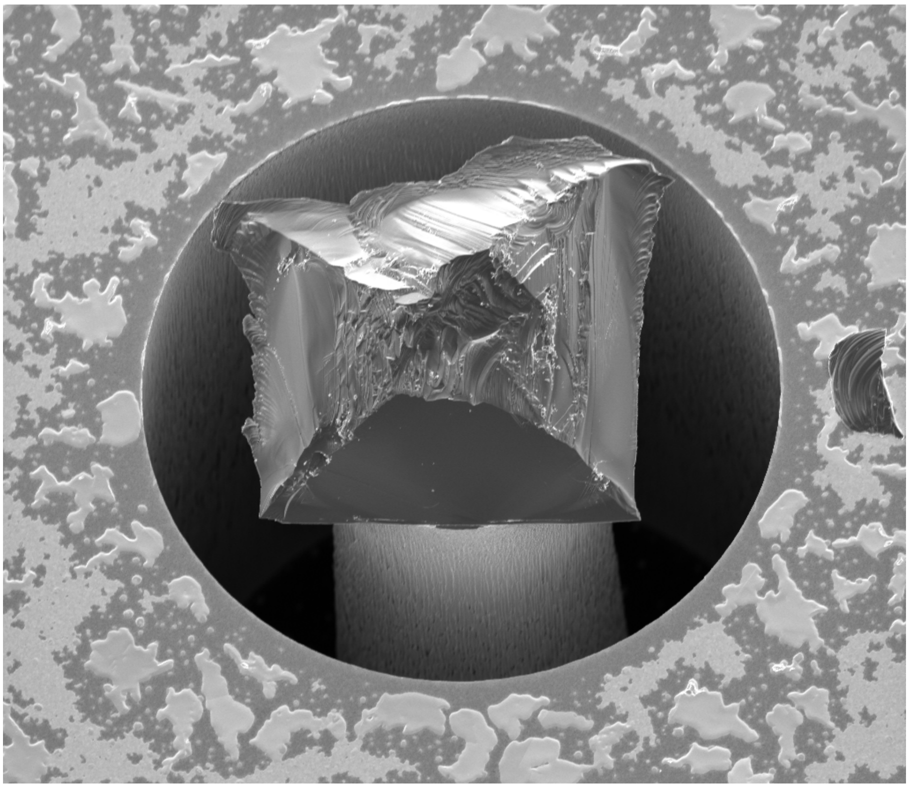

Supervised by:
Prof. dr. ir. G. J. M. Krijnen
Dr. ir. R. J. Wiegerink
Dr. ir. H. V. Jansen
Ing. J. W. Berenschot
Ir. R. A. Brookhuis
Prof. dr. ir. J. G. E. Gardeniers

Master thesis in the field of Electrical Engineering
August 2011 – May 2012.

May 3, 2012

Abstract

The design of a six degree-of-freedom force and moment sensor, using resistive read-out methods is presented in this thesis. An overview of resistive force sensors form the last two decades is given, in which key aspects in sensor design and measuring techniques are compared and discussed. Specific design requirements impose that the sensor should work in a force range higher then presented before in a multi-axis sensor. The design features a mechanical load reduction method, whereby the applied force is translated into a displacement to be measured by the sensing structures. Separate sensing structures for the normal and shear force are placed on the device in an array, enabling temperature compensation, differential measurement and a higher sensitivity.

Eutectic bonding is proposed as the bonding technique for the sensor fabrication, allowing low-temperature processing and deposition of the strain gauges and bonding material in the same processing step. A study is presented into the research published about eutectic bonding and a summary is given of the scientific knowledge of this technique. Several experiments are conducted to find the optimal processing conditions and eutectic bond strength for various metal layer configurations. Results show various, never before published, fracture patterns and bond interfaces. Average bond strengths of up to 106 MPa are found, depending on the deposited metal layers. This work enables future development of a high-load resistive multi-axis force sensor and strong low-temperature wafer-to-wafer bonding.

Contents

Chapter 1

Introduction

This thesis presents the design of a resistive force sensor measuring 6 degrees-of-freedom and the investigation into the method of eutectic wafer-to-wafer bonding. In this chapter, a general introduction into the application is given and the requirements are defined after which the outline of this thesis is discussed.

1.1 Introduction to the Powersensor

In physical labor, interactions with the environment need to be performed within safe limits of body loading. In rehabilitation, people who had a stroke need to relearn functional motor tasks involving physical interaction with their environment. In sports, motor tasks are trained to the ultimate, maximizing force and/or endurance and optimizing coordination. Robots become more and more versatile, performing varying tasks in physical interaction with the environment. All of these examples involve the physical interaction between two bodies, a human body or robot and the environment. In all of these cases, this dynamic interaction is to be optimized or improved. For this purpose, it is essential to asses this interaction quantitatively in terms of force and movement at the interface, power transfer and timing, work performed and effective dynamics of both the human body or robot and the environment during the performance of functional tasks in the environment in which these tasks are performed in daily life.

To measure the interactions between the human body and its environment, miniature sensors can be used measuring acceleration and force. Force times velocity yields power, i.e the amount of energy that is transferred per unit time. Integrating power over time yields work performed on the environment. The relation between force and velocity characterizes the effective dynamics of both the human body and the environment during their interaction. Essential for the application of this principle during free motions is the ability to reconstruct the movement at the interface between body and environment, specifically velocity, position, angular velocity and orientation as a function of time. Orientation and angular velocity can be estimated for indefinite periods of time. Change of position with time can be estimated for movements of limited durations, typically several seconds. For longer periods of time the estimate becomes increasingly erroneous. Fortunately, most human interactions with the environment in which both velocity and force are unequal to zero, and thus work performed, are of limited duration or approximately cyclical. This may make accurate power estimation for most human movements feasible [1].

In Figure 1.1, a schematic image is given of a glove with several sensors incorporated to measure the acceleration of the hand and the force it exerts on the objects it holds, in this case a ball. This is one of the possible applications to find the energy that is exchanged with the environment and its the current goal of the Powersensor project [2, 3]. Currently, research is conducted into the development of the multi-axis force sensor to be incorporated in such a glove [4], using capacitive readout. However, capacitive read-out requires complicated measurement electronics and is susceptible to capacitive coupling to the material applying the force. Therefore,

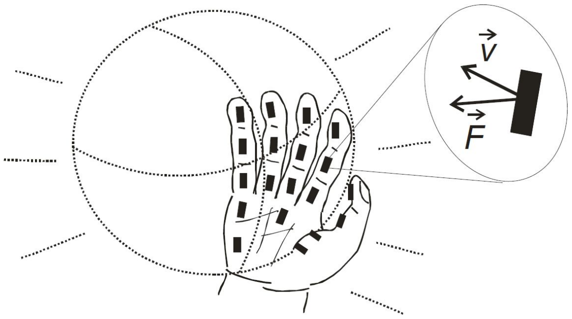

Figure 1.1: Image taken from the project proposal [2]: The Powersensor glove, in which several force and acceleration sensors are incorporated to measure the energy transfer between the human body and its environment.

alternative methods of sensing are sought after. One possibility is the use of resistive sensing methods. Resistive sensing provides clear advantages as it is insusceptible to capacitive coupling and can be used in direct voltage measurement. Disadvantages of resistive sensing are drift and temperature dependence. However, when the sensor is used to measure forces of limited duration, as it is here, drift has no significant influence. In this thesis, an investigation is presented into the design and development of a multi-axis force sensor using resistive sensing methods.

1.2 Requirements

For the design of the force and moment sensor, the following requirements are stated. As the sensors are to be incorporated into a glove, the sensors should be small. Therefore, the effective area of the sensor should be no larger than 5 x 5 mm. The sensor should be able to measure the forces that are exerted by the hand during daily activities such as gripping and holding objects, but also catching or throwing during for instance sport activities. This requires a large range of force that can be measured, but high sensitives so that also fine movements with small forces, such as holding a glass, can be measured accurately. It is therefore determined that the sensor should be able to to measure up to 50 N of normal force and up to 10 N of shear force, with a accuracy of 1%.

1.3 Thesis outline

This thesis will start with a investigation into earlier work on three and six component force and moment sensors, based on (piezo)resistive sensing methods, in chapter 2. An overview of the different designs and devices presented over the years is given and the key aspects of the sensors are discussed and compared. Based on these findings, the design of a six component force and moment sensor is presented in chapter 3. First, a conceptual design will be introduced, after which the different sensing structures are discussed. Then, the dimensions of the structures on the device are established. At the end of the chapter, options on wiring and readout are given.

One very important aspect of the design of the sensor is the bond that is created between two wafers. The method of eutectic bonding is proposed, for which the accumulated experience and scientific knowledge is scarce. Therefore, a study into the scientific papers presented over the years on eutectic bonding is presented in chapter 4. In chapter 5, several experiments are presented that are conducted to give insight in the process of eutectic bonding and to provide qualitative and quantitative knowledge about the achieved bond strength. Conclusions on these findings are presented in chapter 6, where the suitability of the proposed bonding method in the design and fabrication of the sensor is discussed. This then leads to the recommendations given on future work.

Chapter 2

Piezoresistive force and moment sensors

This chapter gives an overview of the force and moment sensors presented in literature over the years. For each sensor, typical aspects such as size, force range and sensitivity are discussed. These key aspects are then compared and a summary of the work on piezoresistive force and moment sensors is presented.

2.1 Introduction

The electrical resistance (R) of a homogeneous material is a function of its dimensions and resistivity (ρ), $R = \frac{\rho l}{a}$, with l the length of the material and a its cross-sectional area [5]. When a material is subjected to a force, the change in resistance originates from changes in geometry and changes in resistivity. The proportion in which the cross-sectional area of a material reduces in respect to longitudinal strain is given by the Poisson's ratio, ν, with the theoretical lower and upper limits for ν in isotropic materials being -1.0 and 0.5. Materials commonly used have a Poisson's ratio between 0 and 0.5. Most metals have a Poisson's ratio between 0.20 and 0.35, while in anisotropic silicon the effective directional Poisson's ratio ranges from 0.06 to 0.36.

The gauge factor (GF) of a strain gauge is defined as $GF = \frac{\Delta R/R}{\epsilon}$ where ϵ is the strain and $\Delta R/R$ is the fractional resistance change with strain, due to both geometric effect $(1 + 2\nu)$ and the fractional change in resistivity $(\Delta\rho/\rho)$ of the material, $\frac{\Delta R}{R} = (1+2\nu)\epsilon + \frac{\Delta\rho}{\rho}$. Geometric effects alone provide a GF of approximately 1.4 to 2.0, and the change in resistivity, $\Delta\rho/\rho$, for a metal is small, on the order of 0.3 [6]. However, for silicon and germanium in certain directions, $\Delta\rho/\rho$ is 50-100 times larger than the geometric term. For a semiconductor, elasticity and piezoresistivity are direction-dependent under specified directions of loads (stress, strain) and fields (potentials, currents). Piezoresistivity shows a linear dependence on the strain up to a strain of 0.1. The sensitivity (S) of a piezoresistive strain gauge is usually measured as a the fractional change in resistance per unit force, $S = \frac{\Delta R/R}{F}$, with F the force on the gauge. Note that since the force is a vector with three components and the piezoresistivity of a material can vary in different directions, the sensitivity also varies in different orientations.

2.2 Sensors

Piezoresistive force sensors are made with silicon micro-technology for decades now. Available in different sizes and degrees-of-freedom, examples include: cantilever force sensors; pressure membranes; shear force sensors; and three and six-axial sensors. Below an overview is given of the various groups working on three and six dimensional force sensors. Typical aspects such as size, force range and sensitivity are investigated and a comparison of the sensors key-aspects is given.

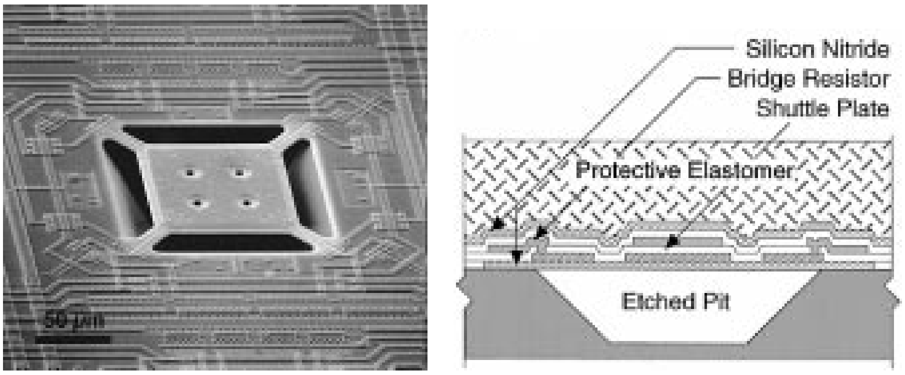

(a) (b)

Figure 2.1: The traction stress sensor from Kane et al.: (a) Scanning electron micrograph of a single sensor; (b) Cross section of the sensing structure.

2.2.1 Kane et al. — Suspended Shuttle Plate

In 1996, Kane et al. published a three-component CMOS-compatible traction stress sensor to be used on robotic systems, in tasks such as grasp-force determination and control; recording texture and curvature data for surface and shape recognition; and detecting the occurrence of slip and rolling at the contact interface [7]. The sensor uses a suspended shuttle plate connected by four bridges, which measures 80 μm x 80 μm, with the total sensor structure less than 300 μm x 300 μm. Each of the bridges features one polysilicon piezoresistor as a strain gauge, which acts as one of the two resistors in a half-bridge configuration providing a direct voltage measure. On top of the structure, a protective and load-transmitting elastomer is placed.

The sensor was tested up to 170 kPa normal stress and 150 kPa shear stress and showed a linearity coefficient of 0.999 with no crosstalk. The sensor has a sensitivity of 51 mV kPa^{-1} for normal stress and 12 mV kPa^{-1} for shear stress. Its minimum resolvable stress is 0.07 kPa for normal stress and 0.29 kPa for shear stress, limited by the noise floor of the measurement setup.

The device was incorporated into an array of 64 x 64 sensors in 2000 [8]. With this array and using an improved measurement setup, Kane et al. found a normal stress sensitivity of 1.59 mV kPa^{-1} and a shear stress sensitivity of 0.32 mV kPa^{-1}. Resolutions are 0.23 kPa for normal stress and 1.0 kPa for shear stress. Modal crosstalk was found to be 2.1%. The temperature coefficient was also measured and was found to be -0.83 mV C^{-1}, which correspond to -0.52 kPa °C^{-1} when measuring normal stress. Figure 2.1 shows the sensor and its cross section.

2.2.2 Jin et al. — Polysilicon Cross-beam

In 1998 Jin and Mote published a three component force sensor, consisting of a 300 μm x 300 μm polysilicon cross-beam as elastic element [9] As such, their design was the first sub-millimeter three-component force sensor. The sensor uses twelve piezoresistors in three Wheatstone bridges to measure the three orthogonal components of force. As, it was stated, it is difficult to control generation and application of forces with known magnitude and orientation on the structure with conventional methods, the design includes an aluminum cross on top of the cross-beam which is used to calibrate the sensor. To exert a force on the sensor, the sensor is placed in a magnetic field an a current is driven through the aluminum cross, to produce a Lorentz force. With this calibration method, resolutions of 10 μN for normal force and 3 μN for shear forces were achieved, with no detectable crosstalk. Figure 2.2 shows a schematic view of the sensor design and calibration method.

The cross-beam design was later extended to a configuration with four diaphragms to be able to measure all six components [10]. The device measures 4.5 mm by 4.5 mm. Each diaphragm features eight piezoresistors in full-bridge configuration, coming to a total of eight Wheatstone

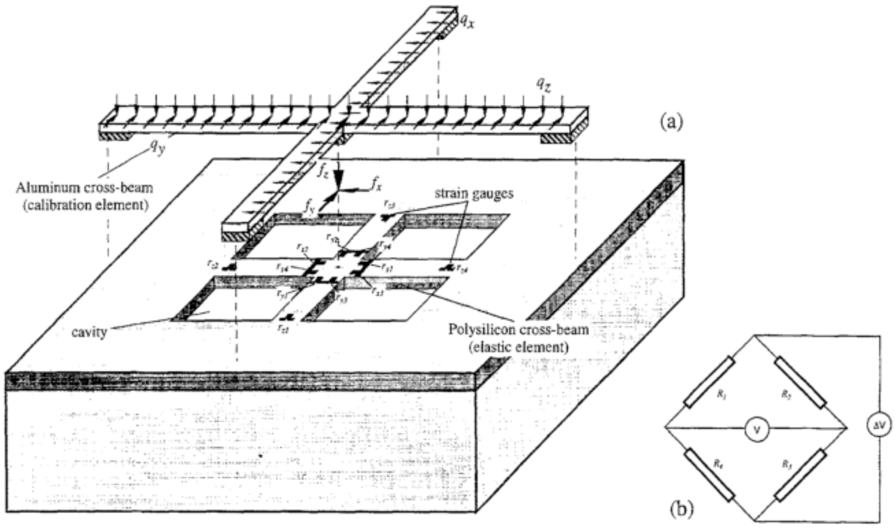

Figure 2.2: Schematic view of the Jin et al. sensor design and calibration method: (a) structure; (b) composition of the Wheatstone bridge.

bridges. Again Lorentz forces were used to calibrate the sensor and resolutions of 1 mN for force components and 2 mN for moment components were found. Figure 2.3 shows the design, cross section and Wheatstone configuration of the extended sensor.

2.2.3 Mei et al., Kim et al. — Tactile Sensor Array

In 2000, Mei and Li published a three-dimensional tactile sensor which has, in contrast with earlier sensors, an extended force range [11]. The sensor has a maximum of 50 N in the vertical direction and 10 N in the horizontal directions. The design consists of an array of four by eight sensing cells, with a size of 16 mm x 32 mm. Each cell measures 4 mm x 4 mm and consists of a square membrane with a force concentrating column on top. A rubber surface is glued on top of the force concentrating columns. To increase the maximum applicable force, each cell features an overload protection. Eight piezoresistors in half-bridge configuration are used to measure the forces in each sensing cell. While the total array can measure op to 50 N of normal force and 10 N of shear force, the maximum force of the single cell is 5 N for normal force and 1 N for shear force. Individual cells showed sensitivities of 13 mV N^{-1} for normal force and 2.3 mV N^{-1} for shear force. See Figure 2.4 for the cross section of the sensing cell and a photograph of the sensor array.

Kim et al. published a three-component force sensor design in 2002 [12]. The sensor consisted of a square membrane, size 2.4 mm x 2.4 mm and thickness 45 μm, with a silicon loading block on top of the membrane. An overload protection block is placed underneath the membrane. As such, the device followed the design of Mei et al., but to increase sensitivity the number of piezoresistors was increased to twelve, and they were connected in full-bridge configuration to enable temperature compensation. See Figure 2.5 for the design of the sensor.

However, in the fabricated sensor presented in 2006, the overload protection block had been discarded and the number of piezoresistors was reduced to four [13]. The 9.5 mm x 9.5 mm sensing array consisted of four by four sensors which are mounted on flexible PCB. The total array is then covered with two-component silicon rubber as a protective layer. The sensor was subjected to forces in the range of 0–2 N and showed resistance variations of 2.1% for normal force and 0.5% for shear force. Also, the fracture strength of a single cell was found to be 3 N. Figure 2.6 shows the location of the piezoresistors and flexible array.

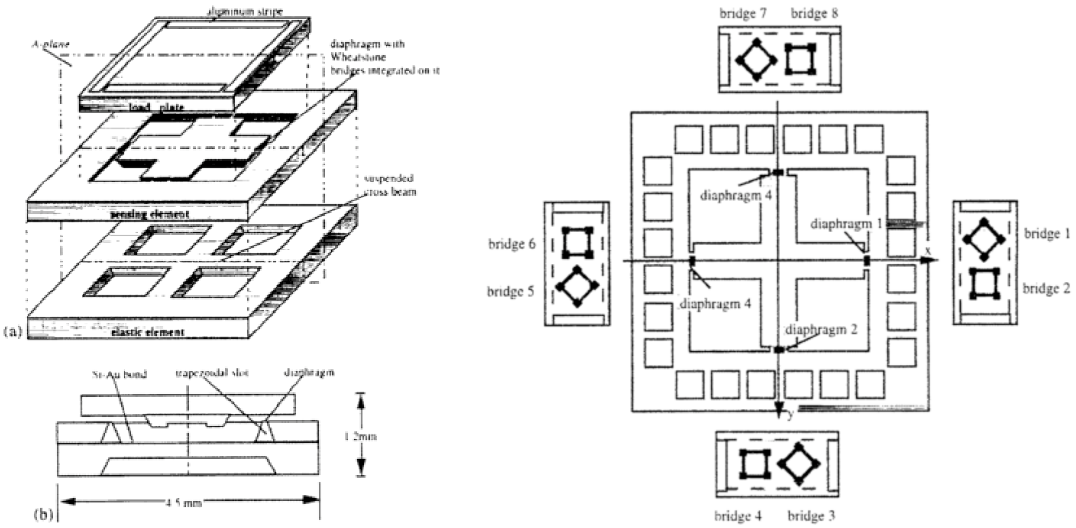

(a) (b)

Figure 2.3: The second sensor from Jin et al.: (a) design and cross-sectional view; (b) diaphragms and Wheatstone bridges on the sensing element.

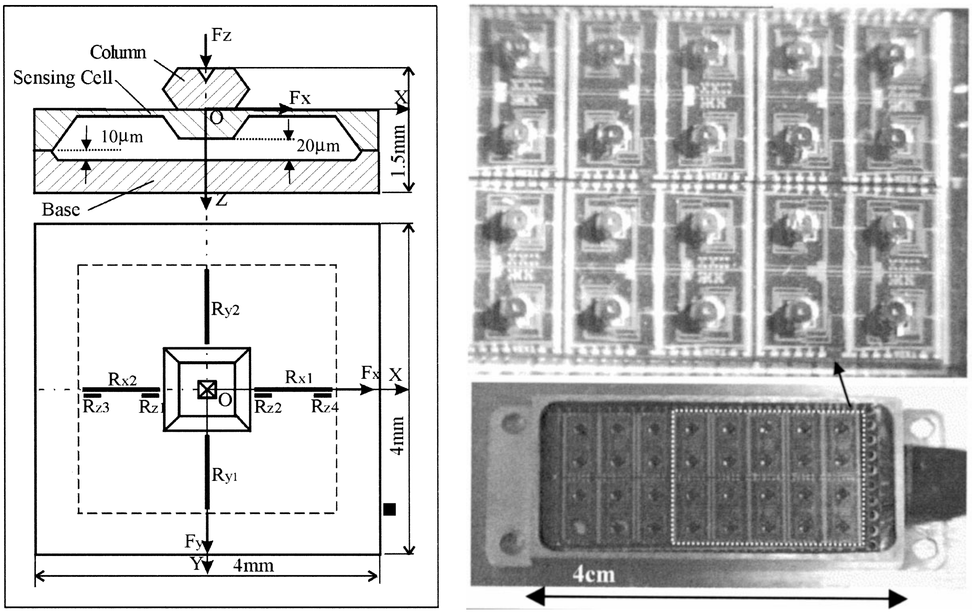

(a) (b)

Figure 2.4: The sensor from Mei et al.: (a) mechanical structure and piezoresistor locations of a single sensing cell; (b) photograph of the tactile sensor without the rubber surface.

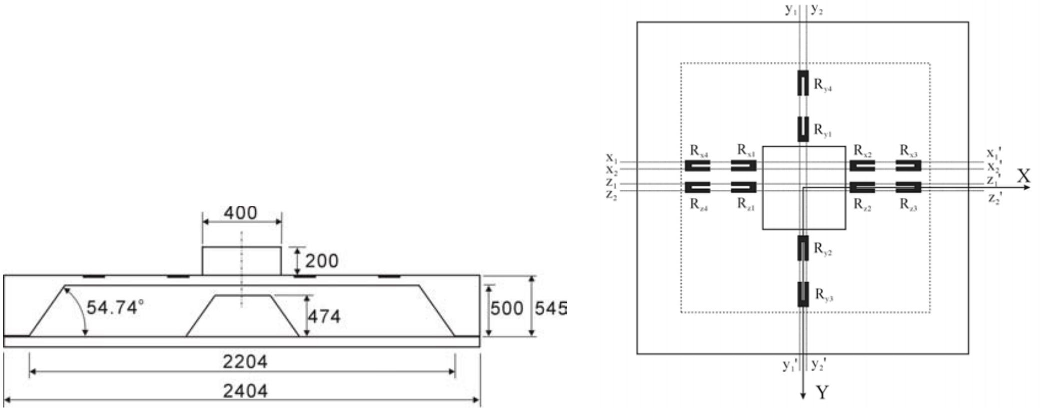

(a) (b)

Figure 2.5: Design of the force sensor from Kim et al.: (a) schematic cross section; (b) location of the piezoresistors.

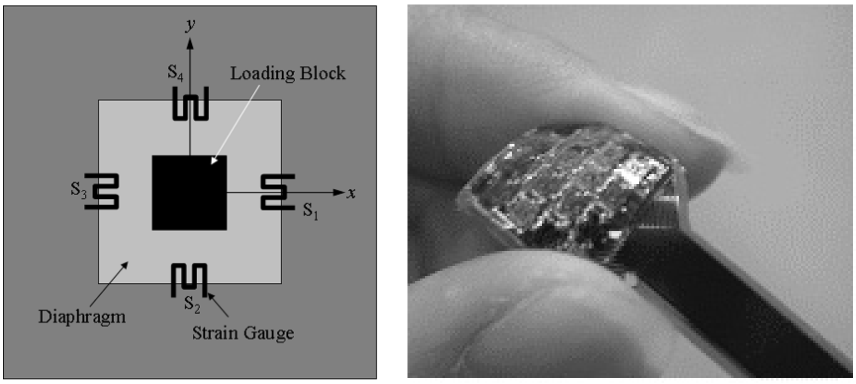

(a) (b)

Figure 2.6: The Kim et al. sensor array: (a) structure top view with the location of the piezoresistors; (b) 4 x 4 sensor cells mounted on flexible PCB.

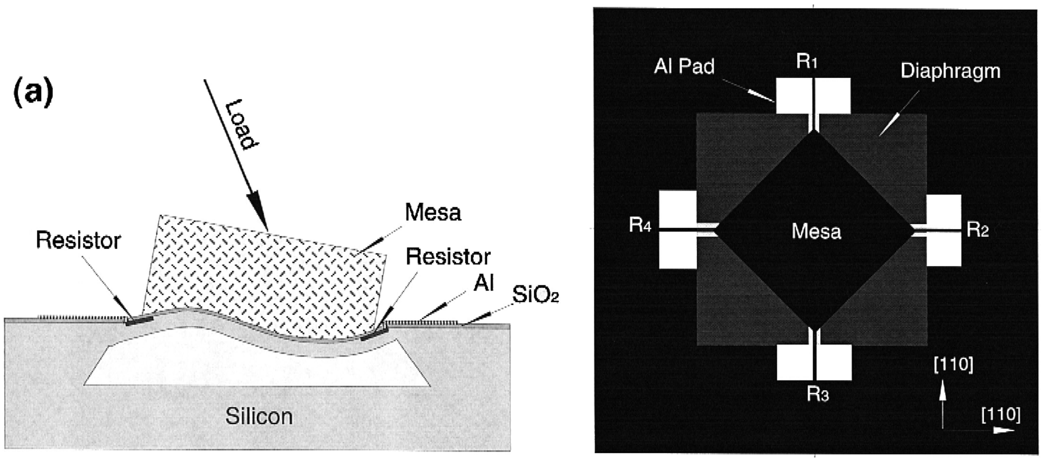

(a) (b)

Figure 2.7: Schematic structure of the sensor from Wang et al.: (a) cross-section view showing diaphragm deflection due to an applied force; (b) top view showing typical placement of the four piezoresistors with respect to the diaphragm and mesa.

2.2.4 Wang et al. — Square Diaphragm

Wang and Beebe published a three-component force sensor in 2000 [14]. Their design was the first to use the four piezoresistors as independent sensing elements because, as they stated, in order to resolve the three components of an arbitrary spatial force, a sensor should have at least three independent sensing elements. The sensor features four ion-implanted piezoresistors embedded on a silicon diaphragm. The diaphragm measures 1.9 mm x 1.9 mm and has a thickness of 50 μm. A photo-resist epoxy structure is placed on the diaphragm as a mesa to distribute stress, measuring 1.3 mm x 1.3 mm with a height of 600 μm. The piezoresistors are placed at the corners of the mesa for maximum sensitivity, with each piezoresistor connected into a separate Wheatstone bridge. The remaining dummy resistors, having the same resistor value, are placed well outside the diaphragm area in the silicon bulk. The sensor was subjected to forces of 0-3 N at various angles and showed a linearity coefficient of 0.98 and a standard deviation of 3%. Figure 2.7 shows the cross-section and top view of the sensor. In 2002, another study of the sensor was published. The sensor now measured 5–40 N of shear force and 0–30 N of normal force [15]. The sensor showed a standard deviation of approximately 1.77 N over the shear-force range of 9–35 N and an average error of 12.1%.

2.2.5 Bütefisch, Nesterov, Tibrewala et al. — Boss Membrane

In 2001, Bütefish et al. published a three-axial force sensor consisting of a square membrane with a boss, to measure forces in the μN – mN range in confined spaces [16]. Possible applications are the determination of spring characteristics of micro-mechanical structures and the measurement of the force exerted by a micro-actuator. The 20 μm thick membrane measures 3 mm x 3 mm and the total device has a size of 5 mm x 5 mm with a height of 0.36 mm. Twenty-four piezoresistors are diffused into the backside of the membrane. Three Wheatstone bridges, each consisting of eight piezoresistors, are used to measure the orthogonal components of the applied force. On top of the boss, a 4 mm long stylus is glued with epoxy resin, on which a glass sphere with diameter 120 μm is attached as tactile element. See Figure 2.8a for the design an piezoresistor location.

To achieve an equal stiffness in the three orthogonal directions, a new design was presented in 2005 [17]. This design is based on two parallel silicon boss membranes attached to each other, see Figure 2.9. Several types of membranes were presented for this configuration, as shown in Figure 2.10. Analytical calculations showed that with these designs equal stiffness in all three directions is possible.

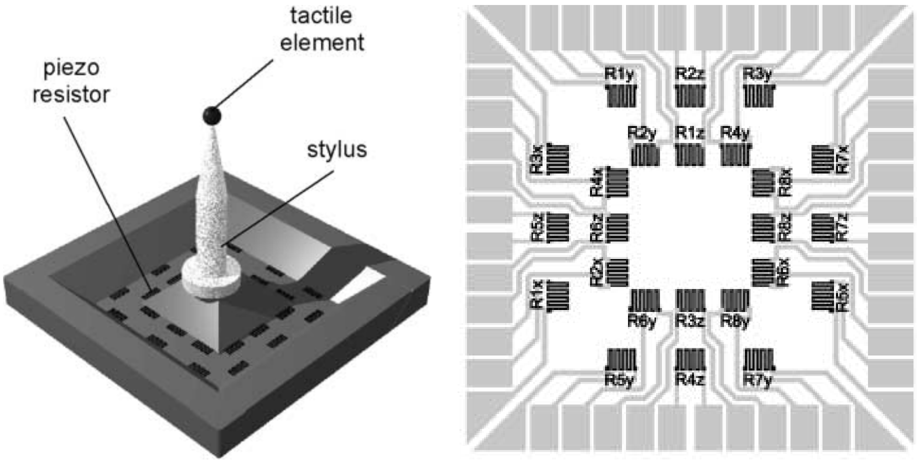

(a) (b)

Figure 2.8: The sensor from Bütefisch et al.: (a)schematic view; (b) piezoresistor location.

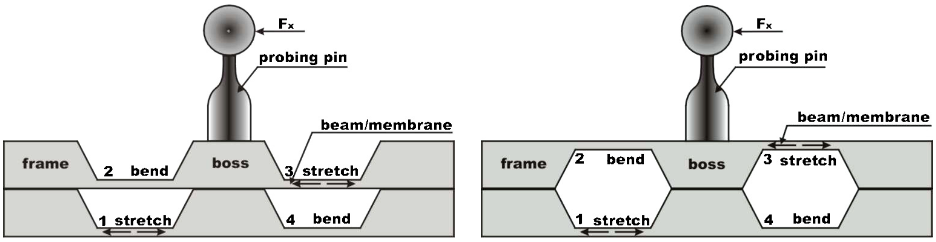

(a) (b)

Figure 2.9: The double wafer design from Nesterov et al.: (a) parralel twin design; (b) inverse twin design.

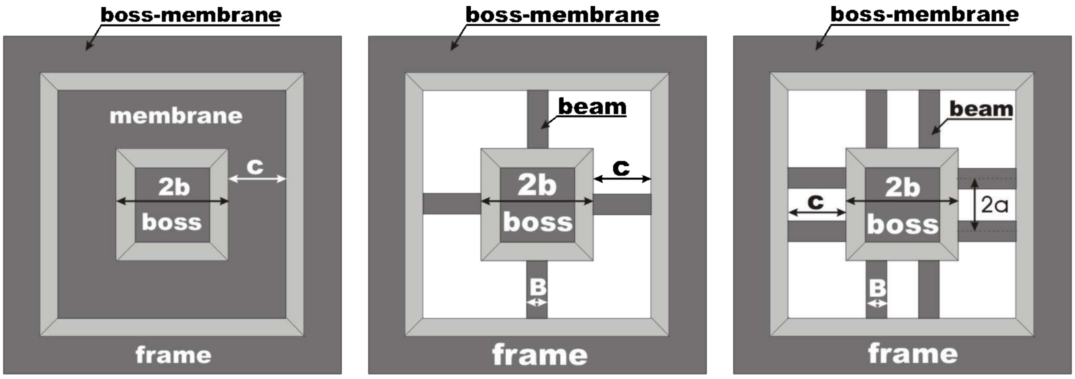

(a) (b) (c)

Figure 2.10: Top view of the different boss-membrane configurations: (a) full boss-membrane; (b) four beams stripe boss-membrane; (c) eight beams stripe boss-membrane.

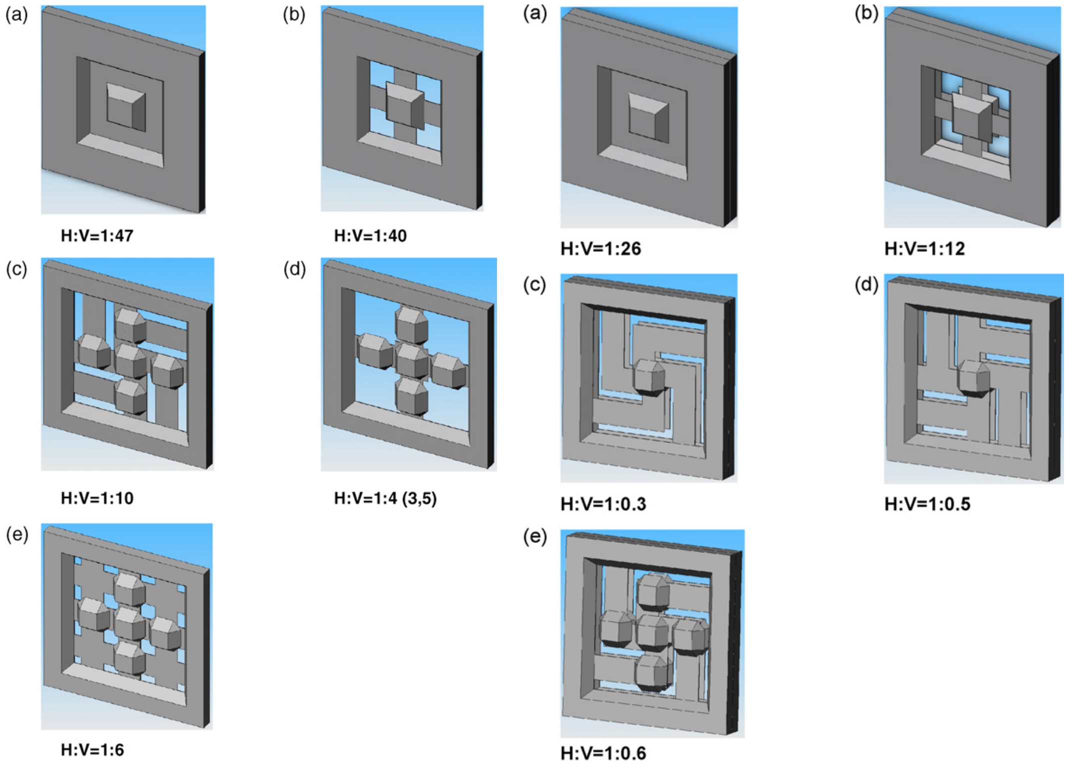

(a) (b)

Figure 2.11: Simulations of different membrane designs along with horizontal vs. vertical deflection ratio, from Tibrewala et al.: (a) single membrane; (b) twin membrane.

This idea was later used in 2008, when Tibrewala et al. simulated several membrane and boss configurations with finite-element packages, including cross-beam structures with multiple bosses to concentrate the stress [18]. Figure 2.11 shows the different membrane simulations with their horizontal versus vertical deflection ratio. In the same article, the authors incorporated sixteen piezoresistive elements on a square membrane to present four different piezoresistor designs, see Figure 2.12a. The membrane has a size of 3 mm x 3 mm and a thickness of 25 μm. The boss has a size of 1.6 mm x 1.6 mm. The sensor was subjected to forces in the range of 0–25 mN for normal force and 0–6 mN for shear force. The T-form configuration showed the best sensitivities, 0.74 mV $V^{-1}mN^{-1}$ for normal force and 2.92 mV $V^{-1}mN^{-1}$ for shear force. An overall temperature coefficient was found of 0.018 mV $V^{-1}K^{-1}$.

In 2009, the different piezoresistor configurations were again tested, this time not on a square membrane but on several cross-beam structures of different width [19]. Figure 2.12b shows the piezoresistor configuration and the accompanying cross-beam widths. For each of the design, the cross-beam has a thickness of 25 μm and a 5 mm long stylus with a ruby ball is attached to the boss. The longitudinal configuration showed the highest sensitivities, with 3.01 mV $V^{-1}mN^{-1}$ for normal force and 11.29 mV $V^{-1}mN^{-1}$ for shear force. Besides the different piezoresistor configurations, a cross-beam structure with one boss was compared to a cross-beam structure with five bosses, shown in Figure 2.13. The transversal piezoresistor configuration was used. The five-boss design was loaded up to 25 μN and showed sensitivities of 2.18 mV $V^{-1}mN^{-1}$ for normal forces and 0.264 mV $V^{-1}mN^{-1}$ for shear forces. The cross-talk was found to be less then 2.5%.

2.2.6 Dao et al. — Force-moment Sensor

Dao et al. presented a six-degree of freedom micro force-moment sensor in 2002, to measure the turbulent flow of sediment particles to be able to improve the simulation technology of geophysical

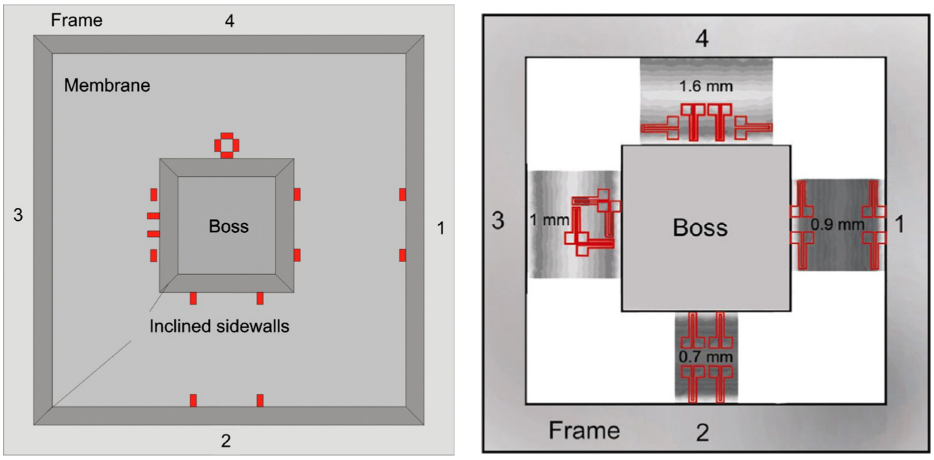

(a) (b)

Figure 2.12: Schematic designs of the sensors with different piezoresitor configuration: 1. transversal; 2. longitudinal; 3. quadratic; 4. T-shaped: (a) boss membrane; (b) cross-beam structure, with varying widths.

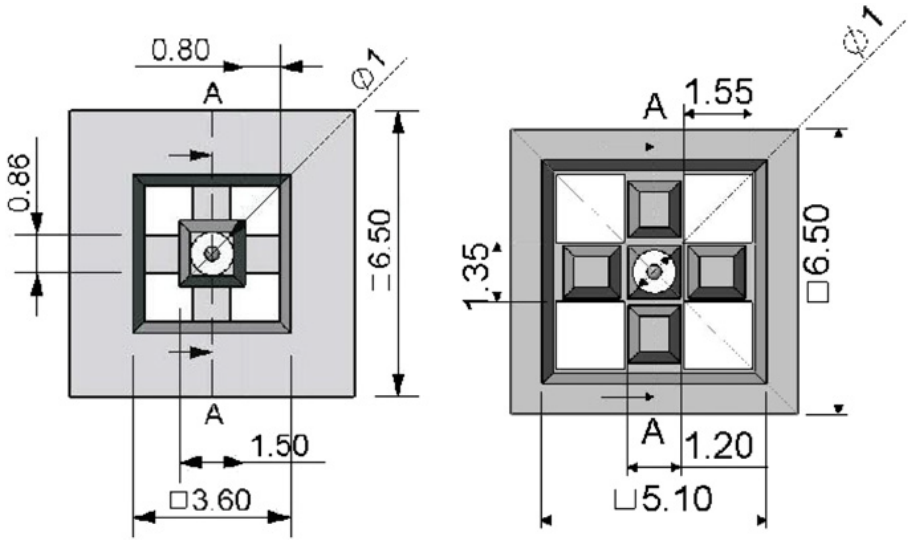

Figure 2.13: Top view of the cross-beam structures: (a) one boss; (b) five bosses.

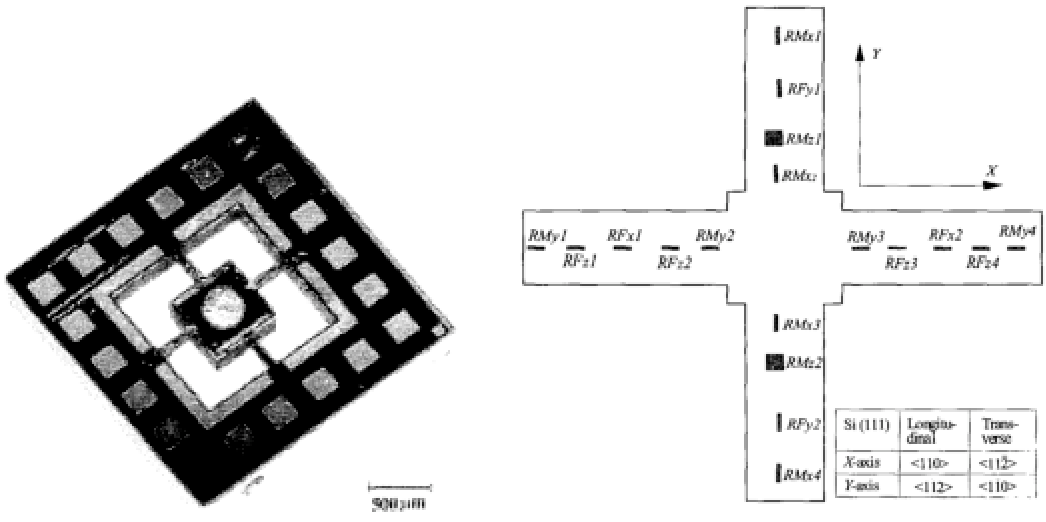

(a) (b)

Figure 2.14: The force-moment sensor from Dao et al.: (a) sensing chip; (b) piezoresistor arrangement on the crossbeam.

micro-mechanics of erosion and transport [20]. The sensing chip is located inside a polyethylene ball with a diameter of 8 mm to be used as a test particle which is subjected to the six components of force and moment. The sensing structure consists of a cross-beam with a central plate. The central plate measures 700 μm x 700 μm with a thickness of 400 μm, while each arm of the structure has a size of 500 μm x 120 μm with a thickness of 40 μm. The overall size of the chip is 3 mm x 3 mm with height 400 μm. A total of eighteen piezoresistors is placed on the cross-beam, sixteen conventional and two shear piezoresistors. The sensor was calibrated up to 50 nN and showed sensitivities of 1.15 mV mN^{-1} for normal force, 0.11 mV mN^{-1} for shear force, 3.4 μV mN$^{-1}\mu$m^{-1} for lateral moments and 0.46 μV mN$^{-1}\mu$m^{-1} for vertical moments. Figure 2.14 shows the sensing chip and the piezoresistor arrangement.

2.2.7 Ádám, Vázsonyi, Vásárhelyi, Molnar et al. — Load Transmitting Rod

A group from Budapest presented a three-dimensional tactile sensor in 2004 made of porous silicon [21, 22]. Using porous silicon, the authors were no longer bound to crystalline orientations when etching the structures, but could benefit from the well-known material properties and piezoresistivity of single-crystalline Silicon. The design featured a cross-beam structure with a central plate, measuring 300 μm x 300 μm. Four piezoresistors are connected in half-bridge Wheatstone configuration. The sensor is loaded with normal forces up to 2 mN and showed a sensitivity of 4–6 mV nN^{-1} V^{-1}. Then, the sensor is covered with silicon rubber, with thicknesses of 220 μm and 500 μm. The first layer highly decreased the sensors sensitivity but dit not alter the linear characteristics. The second, thicker, rubber decreased the sensitivity even more, up to a factor 30, and introduced a higher order exponential-like response, due to the nonlinear behaviour of the protective layer. A further enhancement is the addition of an epoxy load transmitting rod to the center of the crossbeam. See Figure 2.15 for the cross-beam design and a cross-section view of the covering. The force transmitting rod proved promising, and in 2005 the group published a novel etching technique to create a monolithic silicon sensor, in which the rod is created in the silicon at the same moment as the cross-beam structure [23]. In 2006 the effects of elastic covers were presented [24].

In 2011, Molnár et al. compared several membrane designs, all with a silicon rod as load

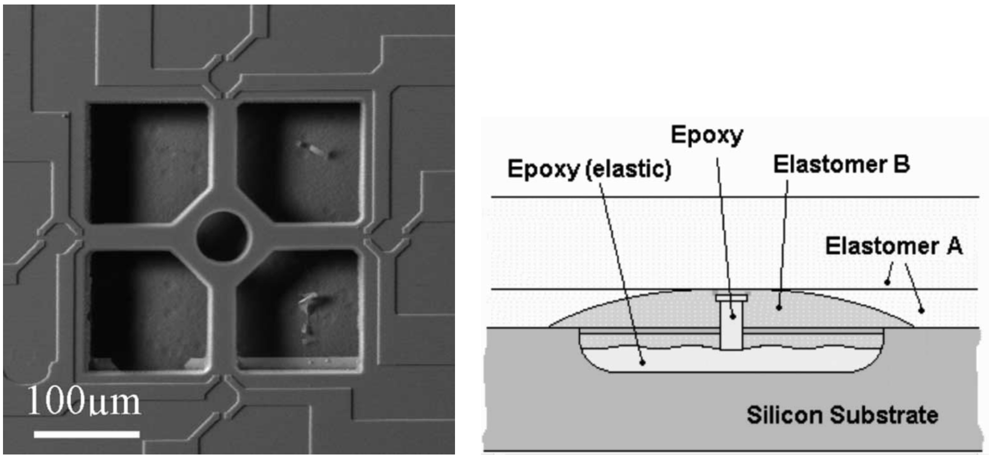

(a) (b)

Figure 2.15: The force sensor from Ádám, Vázsonyi, Vásárhelyi et al.: (a) scanning electron micrograph; (b) cross-section of the sensing structure with load transmitting rod and protective covering.

transmitter [25]. Circular and square membranes were compared and variations in membrane thickness and fill factor were tested. In each design, Four piezoresistor are placed at the edges of the membrane and connected in half-bridge Wheatstone configuration. When loaded with normal forces in the range 0–2.5 N, a sensitivity was found of 5.98 mV $V^{-1}N^{-1}$. A square membrane, size 940 μm x 940 μm and thickness 162 μm, is used with a square rod, size 200 μm x 200 μm and height 310 μm.

2.2.8 Beccai, Valdastri, Sieber et al. — Hybrid Force Sensor

Beccai et al. published a hybrid three-axial force sensor to be used in a flexible smart interface for biomechanical measurements in 2005 [26]. The sensor uses a 525 μm high silicon mesa on a cross-beam structure and four piezoresistors are incorporated to measure three components of force. The sensor showed a sensitivity of 32 mV $V^{-1}N^{-1}$ when loaded with normal forces in the range of 0–2 N, with a linearity of 0.997. When subjected to shear forces in the range of 0–0.7 N, the sensor showed a sensitivity of 32.3 mV $V^{-1}N^{-1}$ and a linearity of 0.981. Further characterization showed a breaking load of 3 N for normal forces and less then 1 N for shear forces [27]. In 2008, Sieber et al. published a flip chip assembly of the sensor to reduce package size and to improve the packaging process [28]. Figure 2.16 shows the Sant'Anna sensor and its design.

2.3 Summary and conclusions

Looking at the developments in piezoresistive sensor design and fabrication, two trends become apparent. First, there is the goal of miniaturization, to create smaller devices and be able to measure ever smaller forces with higher sensitivities and resolution. To create smaller devices, sensors usually consist of only one sensing structure, which in turn is mostly found to be a crossbeam, to maximize the stresses at the locations of the piezoresistors. Examples of this trend are Kane et al., Jin et al., Bütefisch, Nesterov, Tibrewala et al. and Dao et al.

The second trend is created by the goal of extending the applicable force range, to create robust sensors, which can be used in many, more industrial, applications. To be able to withstand greater forces, several tactics are applied. Some sensors incorporate overload-protection blocks in their silicon design or use arrays of sensing devices to distribute a total load. Also, when looked at the sensing structures, usually a membrane is used instead of a crossbeam, because the stresses become smaller when there is a bigger area to distribute the force over. Examples are Mei et al. and Kim et al., Wang et al. and to some extend Beccai, Valdastri, Sieber et al.

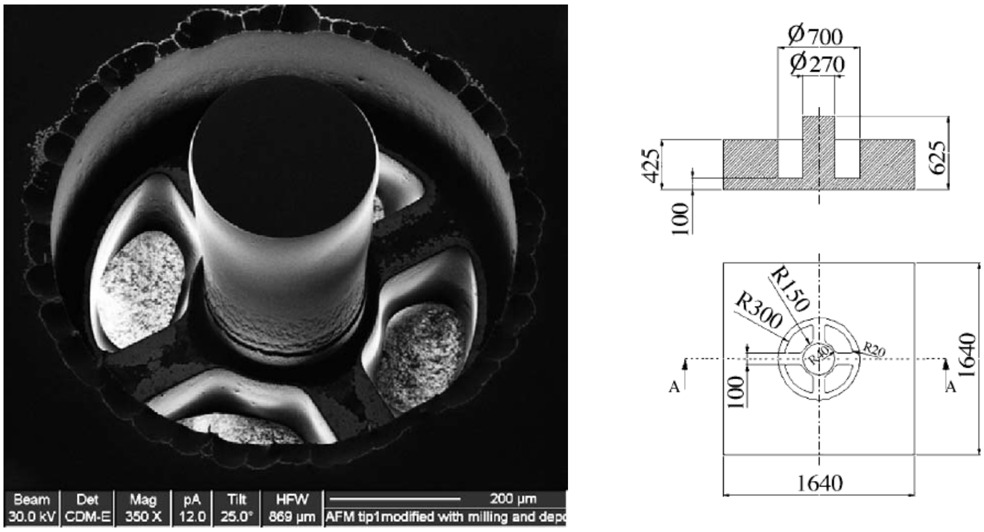

(a) (b)

Figure 2.16: The force sensor from Beccai, Valdastri, Sieber et al.: (a) focused ion beam view; (b) detailed drawing of the sensor and its dimensions.

Packaging and application-wise, one application in particular stands out, the tactile sensor to be used with robotic systems. Kane et al., Mei et al., Kim et al. and Wang et al. all present a desire to improve tactile registrations during automated grasping. Many designs featured some sort of softer material, such as rubber or polymer, on top of the sensing structure to improve the sensitive area of the devices. Other applications include micro-actuator force registration, turbulent particle flow sensing and biomechanical characterization.

Several articles aspired to improvements in research and technology. Jin et al. showed a new way to calibrate their micro-sensor using the Lorentz forces exerted by a current through the incorporated metal cross when the chip was placed in an magnetic field. Nesterov, Tibrewala et al. conducted an extensive study to find optimal mechanical configurations. Ádám, Vázsonyi, Molnar et al. used porous silicon in their designs so that they were no longer affected by crystal orientation but still could benefit of the material properties of single crystalline silicon, where Vásárhelyi studied the effects of elastic covers.

Using piezoresistivity as the sensing method, all devices show excellent linearity and now that many groups have shown a successful sensing structure, some shift the focus of their research from the mechanical structure towards incorporating wiring and read-out methods onto the same chip. Examples are Kim et al. and Beccai, Valdastri, Sieber et al.

Table 2.1: Comparison of the key-aspects of the presented piezoresistor sensors.

Article	Principle	No. of Axes	Size	No. of P.resistors	Wheatstone Configuration	Force Range (Normal/Shear)	Sensitivity (Normal/Shear)	Temperature Compensation
Kane et al. [7]	Suspended plate	3	300 x 300 [μm]	4	Half-bridge	0,07–170 / 0,29–150 [kPa]	12 / 51 [mV/kPa]	Yes
Jin et al.[9]	Cross-beam	3	300 x 300 [μm]	12	Full-bridge	/	/	Yes
Jin et al. [10]	Cross-beam	6	4,5 x 4,5 [mm]	24	Full-bridge	/	/	Yes
Mei et al. [11]	Membrane	3	4 x 4 [mm]	8	Half-bridge	0–5 / 0–1 [N]	13 / 2,3 [mV/N]	No
Kim et al. [12]	Membrane	3	2,4 x 2,4 [mm]	12	Full-bridge	/	/	Yes
Wang et al. [14, 15]	Membrane	3	1,9 x 1,9 [mm]	4	Quarter-bridge	0–30 / 5–40 [N]	/	No
Bütefisch et al. [16]	Membrane	3	5 x 5 [mm]	24	Full-bridge	0–100 / 0–10 [mN]	/	Yes
Tibrewala et al. [18]	Membrane	3	3 x 3 [mm]	16	Full-bridge	0–25 / 0–6 [mN]	0,74 / 2,92 [mV/V/mN]	Yes
Dao et al. [20]	Cross-beam	6	3 x 3 [mm]	16	Half-bridge	0–50 / 0–50 [mN]	1,15 / 0,11 [mV/mN]	Yes
Ádám et al. [21, 22]	Cross-beam	3	300 x 300 [μm]	4	Half-bridge	0–2 / [mN]	4–6 / [mV/V/mN]	Yes
Molnár et al. [25]	Membrane	3	940 x 940 [μm]	4	Half-bridge	0–2,5 / [N]	5,98 / [mV/V/N]	Yes
Beccai et al. [26, 27]	Cross-beam	3		4	Quarter-bridge	0–2 / 0–0,7 [N]	32 / 32,3 [mV/V/N]	No

Chapter 3

Design

This chapter presents the design of the force sensor with six degrees-of-freedom. First, the conceptual design of the sensor is introduced. Then, the sensing structures are established and the geometry and number of structures are calculated. After this, options on wiring and readout are presented.

3.1 Conceptual design

The sensor should be able to measure up to 50 N of normal force and 10 N of shear force, with an effective area of 5 mm^2. From earlier sensors presented in section 2.2 it is clear that it is hard to measure such large forces using single sensing structures. Examples of an array of sensing cells however, quickly become larger than the required area. To be able to measure large forces on a small area, it is necessary to provide some mechanical force reduction so that the measurements can be done by small structures. The proposed structure consists of two wafers bonded together with load-bearing pillars, as presented earlier by Wiegerink et al. [29] and Brookhuis et al. [4]. A schematic cross-section is given in Figure 3.1. As a force is applied on the top wafer, the load is transmitted to the pillars, which will subsequently deform. This then leads to a displacement of the top wafer that can be measured by the sensing structures in the bottom wafer. Variations in the geometry of the pillars allow somewhat individual tuning of the normal and shear force constants.

The sensing structures consist of beams in the bottom wafer that are fixed to the top wafer. On the beams, strain gauges are deposited. A displacement of the top wafer leads to stress, and thus strain, in the beams which will also invoke strain in the strain gauges. With this design, the horizontal and vertical displacements are measured using different structures, so the structures can be individually tuned. As can be seen in Figure 3.1b, when a horizontal load is applied, the stress is spread over the whole length of the beams and to get as much signal as possible, the strain gauges should be applied over the whole beam. When a vertical load is applied, see Figure 3.1c, the beams bend such that the top surface experiences both compressive and tensile stress. The strain gauges should therefore not be longer than half the beam, as the two strains would cancel each other. To get more signal when only half the beam can be used, the beams measuring the vertical deflection can be made wider, or several beams can be placed parallel. This would drastically increase the stiffness in horizontal direction, so the top wafer should not be attached directly to the beams measuring the vertical displacement, as they would prevent the top wafer moving in horizontal directions. Therefore these structures are connected via a pillar similar to the load bearing pillars.

The structures measuring the horizontal displacement can only measure one component, x or y, so at least two of these structures have to be placed perpendicular to each other in the bottom wafer. This means that the structure measuring the x-deflection should not be too stiff in the y-direction and vice versa, as it would prevent the top wafer from moving. Connecting the

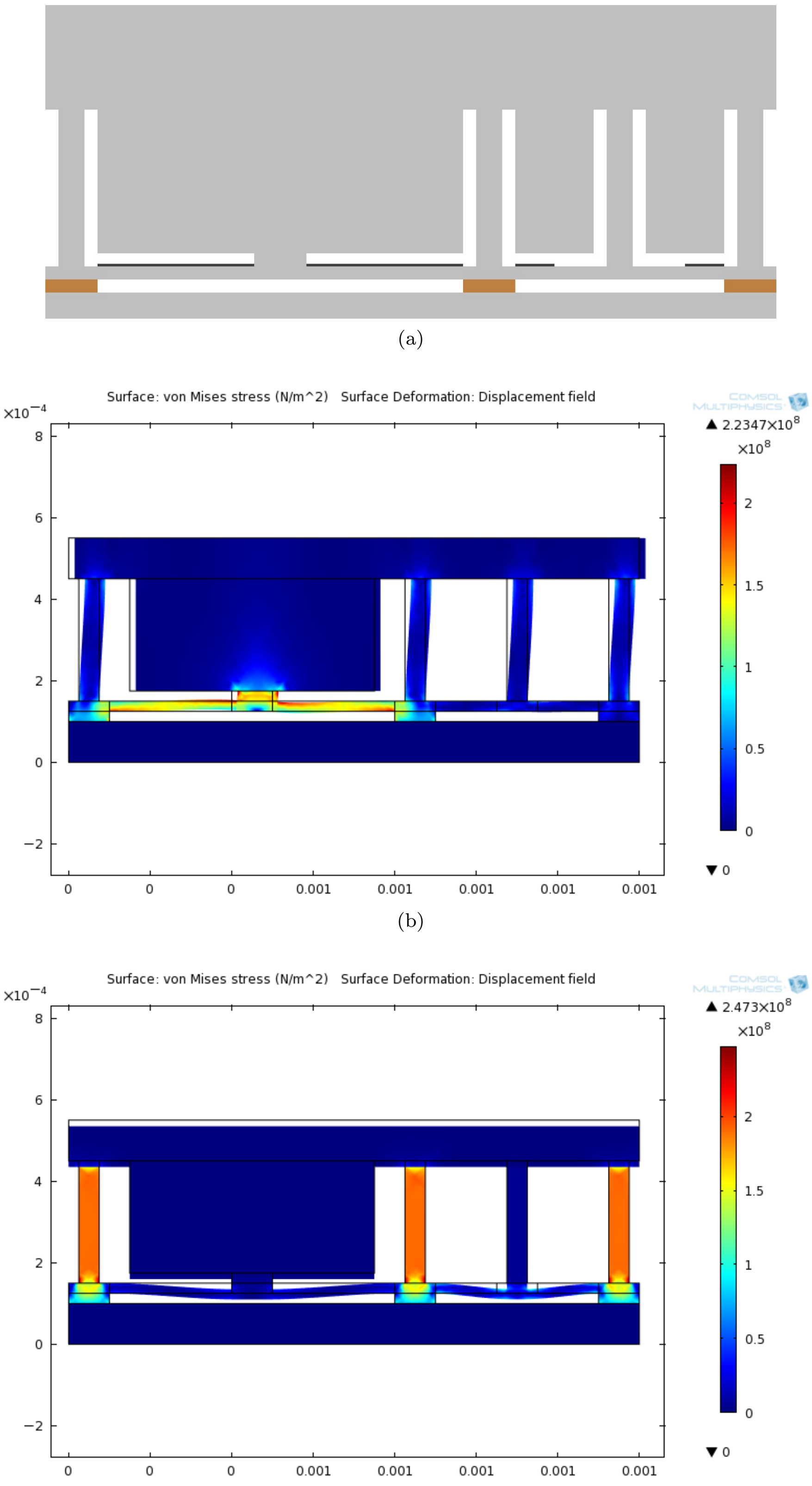

(a)

(b)

(c)

Figure 3.1: Cross-sections of the (a) sensor; (b) horizontal displacement; (c) vertical displacement.

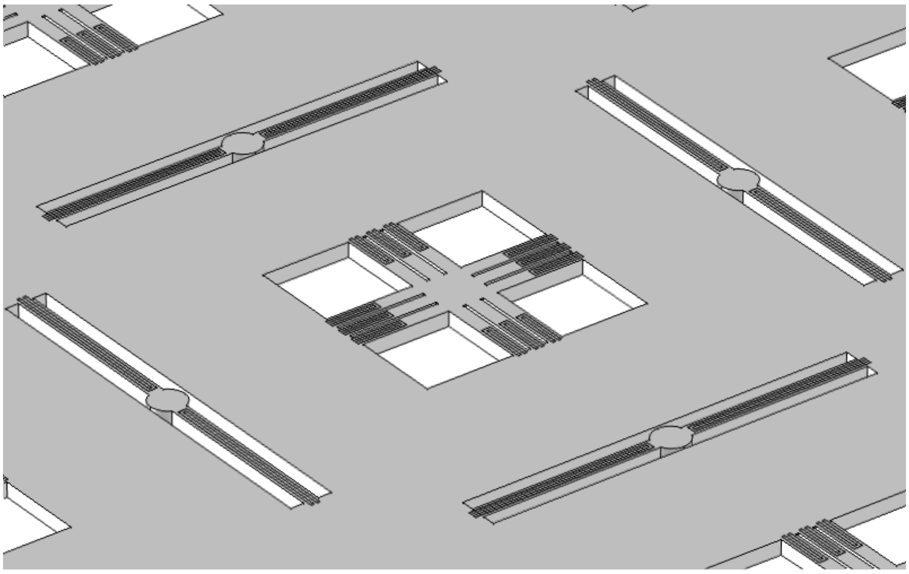

Figure 3.2: Schematic image of a sensing cell, with the cross-beam structure to measure the vertical displacement and the axially loaded beams to measure the horizontal displacements.

horizontal load sensing structures to the top wafer via a slender pillar would not result in a working configuration, as the pillar would deflect too much and very little stress, and therefore strain, would be transfered to the beams. Therefore, the beams measuring the horizontal displacement are attached directly to the top wafer and should be long enough so that they provide no significant stiffness in the directions perpendicular to the beams. Figure 3.2 shows a schematic image of the sensing structures incorporated into the bottom wafer. While three structures as one sensing cell are sufficient to measure the three components, several cells can be distributed over the device to increase sensitivity and create a more uniform sensing characteristic.

3.2 Dimensioning

Following the initial concept, the geometry and size of the different structures are determined, based on structural mechanics as well as fabrication process limitations. This section begins with a short overview of the mechanics of materials used in dimensioning this design.

3.2.1 Theory

The pillars and beams used in this design are subjected to various forces, resulting in axial load and bending. Therefore, the formulas are given relating the stress and strain to the force and displacement. Also given is the formulas for buckling, to make sure the structures do not fail, and the derivation of the strain gauge factor, to calculate the change in resistance from the strain gauges when the sensor is subjected to loading.

Axially loaded beams

The stress on a axially loaded beam is given by [30, p. 25]:

$$\sigma = \frac{F}{A} \tag{3.1}$$

in which σ is the stress, measured in Pa, F the force in N and A the cross-section of the beam, in m^2. The stress is related to the strain of the material of the beam via [30, p. 94]:

$$\sigma = E \cdot \epsilon \quad \text{or} \quad \epsilon = \frac{\sigma}{E} \tag{3.2}$$

where E is the material's Young's modulus given in Pa and ϵ the strain of the beam defined by $\epsilon = \Delta L/L$ [30, p. 87]. The change in length of the beam can now be defined as a function of the geometry and applied force [30, p. 125]:

$$\Delta L = \epsilon \cdot L = \frac{FL}{EA} \tag{3.3}$$

This equation gives the relation between force and displacement $F = \frac{EA}{L}\Delta L$ from which the spring constant of the beam is found:

$$k_{axial} = \frac{EA}{L} \tag{3.4}$$

For a beam with a rectangular cross-section with width w and height h, such as the beams measuring the horizontal displacement, the spring constant becomes:

$$k_{axial,rectangular} = \frac{Ewh}{L} \tag{3.5}$$

while for a circular beam with cross-section πr^2, such as the load-bearing pillars, the spring constant is given by:

$$k_{axial,circular} = \frac{E\pi r^2}{L} \tag{3.6}$$

Bending

The maximum stress for a bending beam is given by [30, p. 297]:

$$\sigma_{max} = \frac{Mc}{I} \tag{3.7}$$

with M the moment working on the beam, given in Nm, c the distance from the neutral plane of the beam in m and I the moment of inertia, where $I = \frac{wh^3}{12}$ for a rectangular cross-section and $I = \frac{\pi r^4}{4}$ for a circular beam [30, p. 799]. For a clamped-guided beam, the moment on the beam is:

$$M = \frac{FL}{2} \tag{3.8}$$

with F the force in N and L the length the of the beam in m. The maximum stress relates to the force via:

$$\sigma_{max} = \frac{FLc}{2I} \tag{3.9}$$

and thus for a rectangular beam becomes:

$$\sigma_{max,rectangular} = \frac{3FL}{wh^2} \tag{3.10}$$

and for a circular beam:

$$\sigma_{max,circular} = \frac{2FL}{\pi r^3} \tag{3.11}$$

The lateral displacement of a clamped-guided beam is given by [31, p. 189]:

$$\delta = \frac{FL^3}{12EI} \tag{3.12}$$

When this is written as $F = \frac{12EI\delta}{L^3}$, the following spring constant is found:

$$k_{bending} = \frac{12EI}{L^3} \tag{3.13}$$

which leads to the following spring constant for a rectangular beam:

$$k_{bending,rectangular} = \frac{Ewh^3}{L^3} \tag{3.14}$$

and the spring constant for a circular cross-section becomes:

$$k_{bending,circular} = \frac{3E\pi r^4}{L^3} \tag{3.15}$$

The displacement relates to the maximum stress via:

$$\delta = \frac{\sigma_{max} L^2}{6Ec} \tag{3.16}$$

Buckling

The critical load, or maximum load on a column just before it begins to buckle, is given by [30, p. 673]:

$$F_{cr} = \frac{\pi^2 EI}{L^2} \tag{3.17}$$

with E the material's Young's modulus, I the moment of inertia and L the length of the column. Substitution of the moment of inertia leads to the following for a rectangular column:

$$F_{cr,rectangular} = \frac{\pi^2 Ewh^3}{12L^2} \tag{3.18}$$

and for a circular column:

$$F_{cr,circular} = \frac{\pi^3 Er^4}{4L^2} \tag{3.19}$$

Strain gauges

The deformation of the length of a material is given by the strain ϵ. When a body is under axial load, it becomes longer (or shorter) and at the same time thinner (thicker). The contraction in directions normal to the axial force is described by the Poisson's ratio ν [30, p. 107]:

$$\frac{\Delta w}{w} = \frac{\Delta h}{h} = -\nu \frac{\Delta L}{L} = -\nu\epsilon \tag{3.20}$$

The electrical resistance of a metal piece is dependent on its size and shape [5, p. 112]:

$$R = \rho \frac{L}{A} \tag{3.21}$$

with ρ the electric resistivity of the metal, L the length and A the cross-section of the body. If now the dimensions of the body change, the resistance will also change:

$$\mathrm{d}R = \frac{\partial R}{\partial L}\mathrm{d}L + \frac{\partial R}{\partial A}\mathrm{d}A = \frac{\rho}{A}\mathrm{d}L - \frac{\rho L}{A^2}\mathrm{d}A \tag{3.22}$$

the strain defines:

$$\mathrm{d}L = L\epsilon = L\frac{\sigma}{E} \tag{3.23}$$

and via the Poisson's ratio is found:

$$\mathrm{d}A = (w + \mathrm{d}w)(h + \mathrm{d}h) - wh \approx w\mathrm{d}h + h\mathrm{d}w = wh(\frac{\mathrm{d}w}{w} + \frac{\mathrm{d}h}{h}) = -2\nu\epsilon A = -2\nu A\frac{\sigma}{E} \tag{3.24}$$

Therefore (3.22) becomes:

$$\mathrm{d}R = \frac{\rho}{A}L\epsilon + \frac{\rho L}{A^2}2\nu\epsilon A = \rho\frac{L}{A}(1 + 2\nu)\epsilon = R(1 + 2\nu)\epsilon \quad \text{or} \quad \frac{\mathrm{d}R}{R} = (1 + 2\nu)\epsilon \tag{3.25}$$

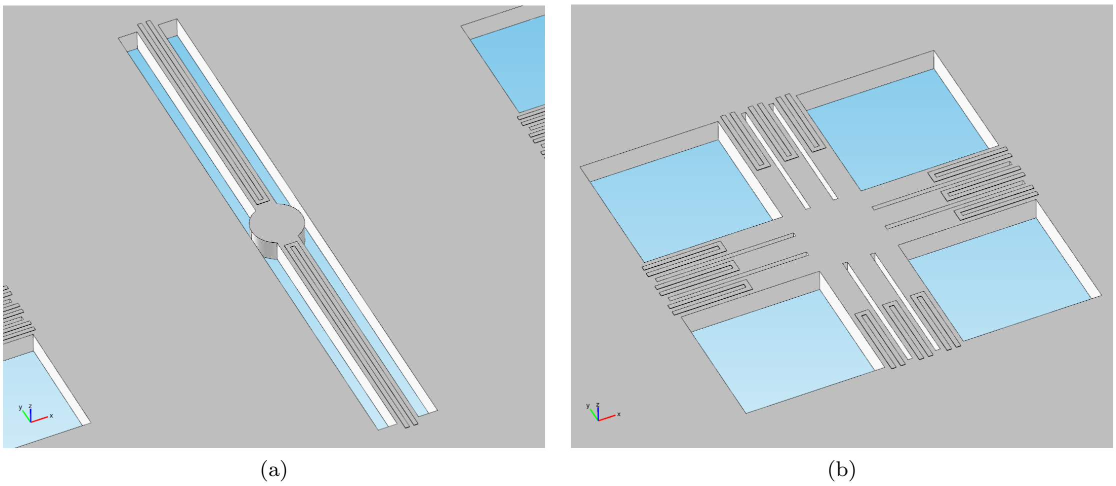

Figure 3.3: The proposed sensing structures: (a) The axially loaded beams to measure the horizontal displacement; (b) The cross-beam structure to measure the vertical displacement.

3.2.2 Sensing structures

Separate structures are used to measure the horizontal and vertical displacements and these structures can be designed individually. However, fabrication process parameters impose some limitations on the sizes of the beams and strain gauges.

Strain gauges

As the strain gauges, a gold metal line is deposited on the beams. The change in length of the beams also changes the length of the gold line, subsequently changing its resistance. The change in resistance is proportional to L/A (3.25), so the strain gauges should be as long as possible and at the same time as thin and small as possible. Fabrication parameters for the used micro-machining technology state that the minimum width of patterned structures is 5 μm. To make sure that the metal lines do not crack under strain, a layer of sufficient thickness has to be deposited. The Au strain gauges are therefore designed to have a width of 5 μm and a thickness of 100 nm. With a minimum resistivity ρ of Au of $2.0 \cdot 10^{-8}$ this leads to a resistance of 40 kΩ/m.

Horizontal displacement sensing beams

To measure the horizontal displacements, two beams are connected to a midsection to which the top wafer is attached (Figure 3.3a). Movement in the directions of the beams leads to the elongation of one and shortening of the other beam. To be able to deposit at least one line of Au back and forth over the length of the beam, the beam should have a minimum width of 25 μm. The height of the beam is chosen to be the same, as a thicker beam would be stiffer in the vertical than the horizontal direction and bending the beam would likely result in torsion of the beam. A beam with a thickness less than its width would be very stable under bending, but would provide a higher stiffness in the horizontal direction perpendicular to the beam which is undesirable as explained in section 3.1

Very long beams seem advantageous, as they permit long strain gauges which have a higher resistivity which would also measure more resistivity change. However, two conditions limit the length of the beams, since long beams become weak in bending, as found via (3.14). First, during fabrication, the beams are freed by wet-etching the material underneath the beams. When the wafers are dried, the capillary pressure of the liquid under the beams results in a force on the beam towards the substrate. If the beams are weak and therefore able to stick to the substrate, the device would not work as it is very hard to release the beams after stiction. Second, when axially

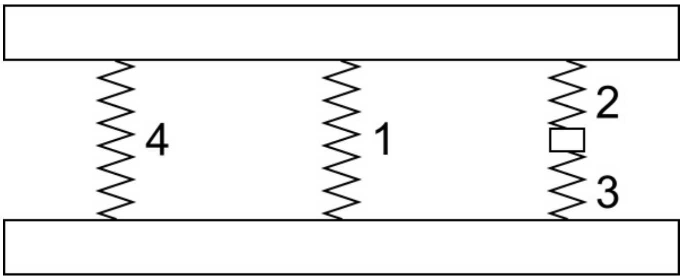

Figure 3.4: Schematic image of the equivalent springs for the mechanical structure of the device: 1, the load-bearing pillars; 2, the displacement-transmitting pillars; 3, the cross-beam structure; 4, the axial springs measuring the horizontal displacements

loaded, the beams should be prevented from buckling. As can be seen from (3.18), increasing the length of the beam severely decreases the maximum axial load on the beam. Therefore, the length of the beam is initially taken to be 300 μm.

Vertical displacement sensing cross

To measure the vertical displacement, a cross-beam structure is proposed (Figure 3.3b). As the strain gauges should only be deposited over half the length of the beams to be able to measure the bending, multiple beams are placed parallel to increase the sensitivity. The stiffness in horizontal directions increases by using multiple parallel beams, but this provides no disadvantage as the cross-beam is attached to the top wafer via a pillar that enables horizontal movement. The width and height of the of the beams of the cross-beam are chosen the same as for the axially loaded beams, 25 μm. The length of the beams is initially taken to be 150 μm. The definitive length should be determined in concordance with the dimensioning of the load bearing pillars, as they determine the maximum vertical deflection of the top wafer. The arms of the cross-beam should be designed such that this vertical deflection results in the maximum allowable stress in the beams, as given via (3.16). The maximum allowable stress in the silicon is taken as 250 MPa, well below the fracture strength of Si to enable a robust design [32, 33].

3.2.3 Equivalent spring constants

To further design and configure the geometry and number of the load-bearing pillars and sensing structures, a model can be made in which each component is represented by its spring constant for normal and shear forces. This will give the resulting forces and displacements in vertical and horizontal directions under applied load for each structure, from which the stress and strain of the material can be calculated. Four types of springs can be identified from the design: 1, the load-bearing pillars, connecting the top wafer to the bottom wafer; 2, the displacement-transmitting pillars, that connect the top wafer to the cross-beam structures measuring the vertical displacement; 3, the cross-beam structure itself; 4, the axial springs measuring the horizontal displacements, as shown in Figure 3.4. As the axial springs are directly connected to the bulk of the top wafer, no spring is placed in between. While the axial springs may only be used to measure one component of horizontal displacements, their structure does work as a spring for normal forces and shear forces perpendicular the the beam, influencing the total spring constant of the sensor and the displacement of the top wafer. When the all the spring constants of the structures of the sensor are combined, two total spring constants are found, one for forces in the vertical directions, $k_{z,total}$ and one for the forces in the horizontal directions, $k_{x,total}$.

Horizontal spring constant

To calculate $k_{x,total}$, the spring constants in the horizontal directions are determined for the separate structures first. The spring constant of the load-bearing pillars is found by using (3.15) and multiplying by the total number of these pillars on the sensor:

$$k_{x,1} = \frac{3n_1 E\pi r_1^4}{l_1^3} \tag{3.26}$$

where n_1 is the number of load-bearing pillars. To find the spring constant of the displacement-transmitting pillars (3.15) is used again, this time multiplied by the number of these pillars:

$$k_{x,2} = \frac{3n_2 E\pi r_2^4}{l_2^3} \tag{3.27}$$

with n_2 the number of displacement-transmitting pillars.

The cross-beam structure normally has arms on four sides, but each side can have multiple arm parallel. For a horizontal force in either the x or the y direction this means that on two of the sides beams are being axially loaded, while the beams on the other two sides are bend. To find the horizontal spring constant for the cross-beam (3.5) and (3.14) are combined:

$$k_{x,3} = (\frac{2Eh_3w_3}{l_3} + \frac{2Eh_3w_3^3}{l_3^3})n_3n_c = \frac{2n_3n_cEh_3w_3}{l_3}(1 + \frac{w_3^2}{l_3^2}) \tag{3.28}$$

where n_c is the number of beams on each side of the cross-beam and n_3 is the number of cross-beam structures on the sensor. Notice that since the beams are bend in the horizontal direction, it is the width w that is taken to the third power.

The axial springs measuring the horizontal displacements consist of two axial beams, one of which elongates and the other shortens as a force is applied. The spring constant of this combination is found by the taking the spring constant of two axially loaded beams in parallel. To measure the horizontal displacements in both the x and y direction, two axial spring structures are placed orthogonal to each other. This means that the axial springs also add a spring constant in the direction perpendicular to the beams. The horizontal spring constant of the axial springs is therefore similar to the spring constant of the cross-beam, with two beams axially loaded and two beams bend:

$$k_{x,4} = \frac{n_4}{2}(\frac{2Eh_4w_4}{l_4} + \frac{2Eh_4w_4^3}{l_4^3}) = \frac{2n_4Eh_4w_4}{l_4}(1 + \frac{w_4^2}{l_4^2}) \tag{3.29}$$

whit n_4 the total number of axial springs of the device.

When these spring constants are combined, the equivalent horizontal spring constant is found. As the force-transmitting pillars are placed upon the cross-beam structure, their spring constants are taken in series. This combined spring constant is then placed parallel to the load-bearing pillars and axial springs:

$$k_{x,total} = \frac{1}{\frac{1}{k_{x,2}} + \frac{1}{k_{x,3}}} + k_{x,1} + k_{x,4} \tag{3.30}$$

Vertical spring constant

To find $k_{z,total}$, the spring constants of the separate structures in the vertical direction are used. The spring constant of an axially loaded pillar is given by (3.6). To find the spring constant of all the load-bearing pillars, the formula is multiplied by the number of pillars:

$$k_{z,1} = \frac{n_1 E\pi r_1^2}{l_1} \tag{3.31}$$

with n_1 the number of load-bearing pillars. The spring constant of the displacement-transmitting pillars is based on the same formula but now multiplied with the number of these pillars:

$$k_{z,2} = \frac{n_2 E\pi r_2^2}{l_2} \tag{3.32}$$

with n_2 the number of displacement-transmitting pillars.

The spring constant of the cross-beam structure can be found using the formula for a bending beam (3.14) and multiplying it for the number of arms of the cross. The vertical spring constant of all cross-beam structures is found by multiplying by the number of these structures on the sensor:

$$k_{z,3} = \frac{4n_3n_cEw_3h_3^3}{l_3^3} \tag{3.33}$$

with n_3 the number of cross-beam structures and n_c the number of arms on each side of the structure. The axial spring consists of two beams and the vertical spring constant is found by using (3.14) again, times two and multiplying by the total of axial springs on the device:

$$k_{z,4} = \frac{2n_4Ew_4h_4^3}{l_4^3} \tag{3.34}$$

with n_4 the number of axial springs.

The equivalent vertical spring constant is composed from the previously found equations. First, the displacement-transmitting pillars and cross-beam structures are taken in series. Then, these are placed parallel to the load-bearing pillars and axial springs:

$$k_{z,total} = \frac{1}{\frac{1}{k_{z,2}} + \frac{1}{k_{z,3}}} + k_{z,1} + k_{z,4} \tag{3.35}$$

With these two spring constants, it is possible to relate the displacements to the applied force. Using the formulas for stress and strain, the structures can be dimensioned such that maximum strain is accomplished but none of them exceed their maximally allowed stress.

3.2.4 Dimensions

Based on the equivalent spring constants, an analytical model is made using Maple to find the stresses and strains in the different structures (given in appendix A). A working configuration is found with the following number and sizes of the structures. An array of 5 x 5 sensing cells is created on the device, with 25 cross-beam structures in total. As the axial beam structures are shared between adjacent sensing cells, their total comes to 60, 30 for the x-direction and 30 for the y-direction. 100 load-bearing pillars are used, with a radius of 25 μm and a height of 300 μm. The load transmitting pillars have the same height and radius and 25 are placed, one on each cross-beam structure. The beams on the axial springs have width and height 25 μm and a length of 300 μm. The arms of the cross-beam have the same width and height but a length of 150 μm. Three beams are placed in parallel on each side of the cross-beam.

When loaded with 50 N of normal force, this results in a total vertical deflection of the top wafer of 487 nm. A shear force of 10 N results in a horizontal deflection of 467 nm. The stress stays below the maximum of 250 MPa in all the structures, but the strain is maximized for the positions of the strain gauges. The stress in the axially loaded beams becomes 233 MPa, with a strain of 0.0016. Given that the strain in the gold strain gauge follows the strain in the silicon, this lead to a change in resistance of 0.029 Ω per deposited strain gauge. The strains in the strain gauges deposited on the cross-beam structure are harder to estimate, as the stresses are not uniformly distributed over the beams when they are bend. However, the maximum stress in the arms of the cross-beam reaches 200 MPa, indicating that significant strain will be achieved. The structures' dimensions, the forces working on each structure and the stresses in the structure are given in table 3.1

3.3 Wiring and readout

The resistance of the strain gauges on the various structures changes under strain. To measure this change, an electrical circuit has to be made, so that the change in resistance results in a change

Structure	Horizontal force (mN)	Horizontal stress (MPa)	Vertical force (mN)	Vertical stress (MPa)
Load-bearing pillars - height: 300 μm - radius: 25 μm	9,54	116,64	477,82	243,35
Load-transmitting pillars - height: 300 μm - radius: 25 μm	9,49	116,02	83,65	42,60
Cross-beam arms - height: 25 μm - width: 25 μm - length: 150 μm	-	-	83,65	200,75
Axial beams - height: 25 μm - width: 25 μm - length: 300 μm	291,59	233,27	2,11	30,42

Table 3.1: The dimensions, forces and stresses of the various structures of the device.

of voltage at some point where it can be measured. The resistance of a metal strain gauge is not only dependent on the strain of the material. One of the most influencing factors of the resistance in a metal is temperature. Variations in temperature may lead to differences in resistance in the order of and even bigger than the changes in resistance due to strain. Therefore, strain gauges are usually connected in such a way that the influence of temperature is compensated.

To cancel the influence of temperature, the strain gauges can be connected in a Wheatstone bridge configuration. Figure 3.5a shows the schematic image of a Wheatstone bridge. For instance, if the values of R_1, R_2 and R_3 are known, whereas the value R_4 is varied, the voltage difference measured at V_0 changes. However, if the temperature changes, al four resistors are affected equally and V_0 does not change. To increase the measured signal, two of the resistors can be used as varying resistors. If now not only R_4 but also R_1 is a strain gauge with a resistance changing under load, the change in voltage V_0 doubles. This is called a half Wheatstone bridge. Sometimes, all four resistors have varying values. Then the resistors on the same leg (R_1 and R_3 or R_2 and R_4) should be connected opposed, so that an increase in one is accompanied by a decrease in the other. This is known as a full Wheatstone bridge and results in the best signal. It is required though, that all resistors have the same initial value and linear characteristic.

3.3.1 Local Wheatstone bridge

The structures measuring the horizontal forces in each sensing cell are very suitable to create local Wheatstone bridges for each cell, as the cell cell consists of two structures with each two opposing strain gauges. A full Wheatstone bridge can be made for both horizontal directions, as shown in Figure 3.5b. The voltage difference between V_1 and V_3 would measure the force in the x-direction, whereas the difference between V_2 and V_4 would measure the force in the y-direction. The strain gauges on the cross beam all have the same characteristic under load, so a full Wheatstone bridge is not possible. Therefore, this structure is connected as a simple voltage divider (only one leg of the Wheatstone bridge) and a dummy resistor is placed next to the cross as the non-changing resistor. This dummy resistor is placed close to the strain gauges so that the temperature is the same as for the resistors.

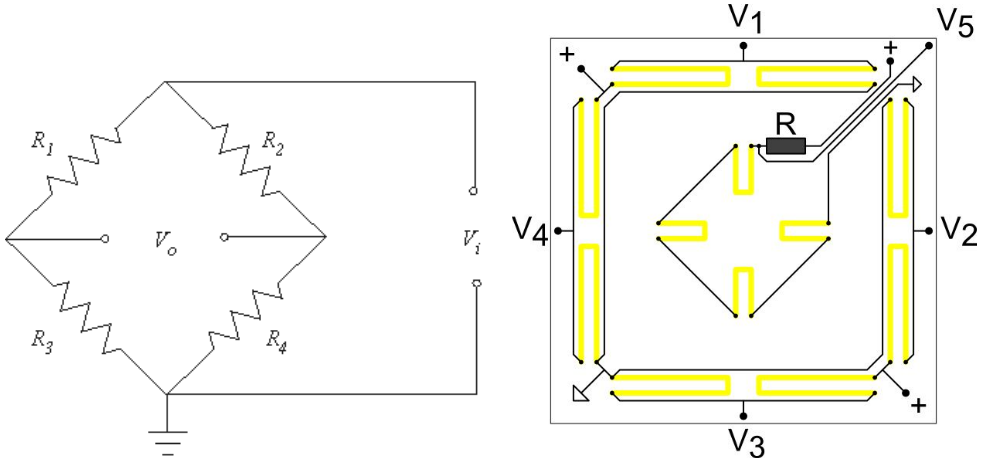

(a) Schematic image of the resistors connected in a Wheatstone bridge.

(b) Configuration possibility to connect the various structures in such a way that full Wheatstone bridges are formed in a single sensing cell.

Figure 3.5

3.3.2 Combined Wheatstone bridges

Creating local Wheatstone bridges for each cell would however, require many connections on the chip and wires to the readout electronics. To decrease the wiring, the structures measuring the same component of force in several cells can be taken together and connected in series. Figure 3.6a shows the different structures distributed over the device and there corresponding component of force. Additionally, using several cells makes it possible to measure not only the three components of the applied force, but also the three possible moments applied to the sensor. A configuration that would measure all 6 components is shown in Figure 3.6b.

To measure the x-component, the red structures are used. Each structure consists of two opposing strain gauges. Each of these strain gauges is connected in series with corresponding strain gauges on the other structures. Due to limitations in wiring, not all red structures can be connected, but two blocks are created. However, in this way a full Wheatstone bridge is created again, as both blocks act as one leg of the circuit. The green structures to measure the y-component are connected in the same way. The z-component is measured with the blue structures in the middle of the device. These structures are connected in series to create one big strain gauge, to measured in a direct voltage configuration.

The rotation around the z-axis, M_z is measured with the light-blue structures. As the displacement from a rotation is larger for increasing radius, these structures are placed on the outside of the device. Opposing strain gauges on two sides are connected in series to create the legs of a full Wheatstone configuration. The rotation around the x-axis, M_x, is measured using two sets of cross-beam structures, shown in yellow, as an applied moment would lead to a difference in the vertical force between the two sides of the device. Three structures are connected in series to create two combined strain gauges that are connected in a half Wheatstone bridge configuration. To measure M_y, the rotation around the y-axis, the pink structures are connected in a similar fashion. Photomask designs for the complete sensor are created using CleWin, incorporating the configuration as stated above which are given in appendix B.

3.4 Summary

In this chapter, the design of the force sensor is presented. The sensor uses pillar structures to provide a mechanical load reduction. Working from an initial concept, the sensing structures are established using the equivalent spring constants. The sensing structures are designed to

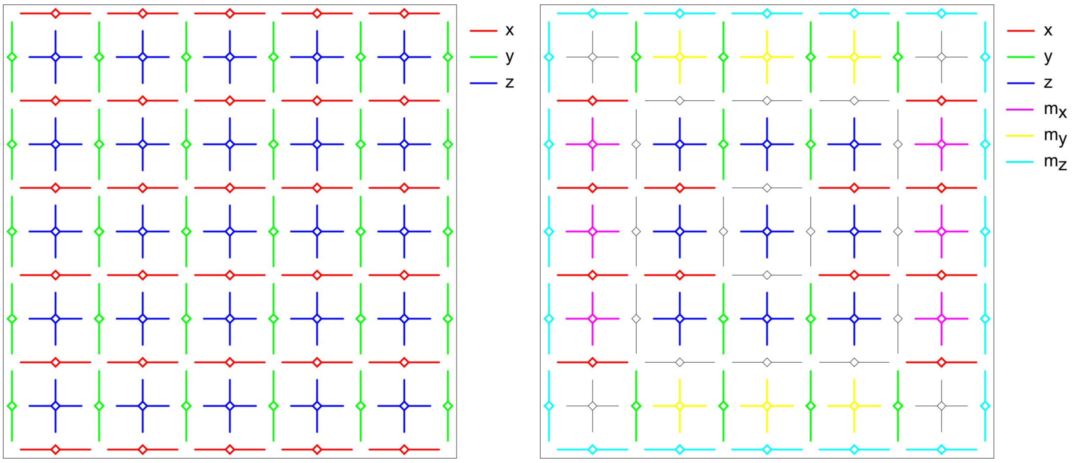

(a) (b)

Figure 3.6: The sensing structures of the device that can be used to measure the various components of the applied force. (a) The structures measuring three components of force; (b) Configuration able to measure six components of force and moment.

approach the maximum allowable stress, to maximize the strain measured by the strain gauges. A quick analysis shows a maximum strain of 0.0016 results in a change of resistance of 29 mΩ per strain gauges, which have an initial resistance of 12 Ω. Several options are given to connect the various strain gauges, compensating for temperature influences and optimizing the measured signal. Lastly, a photomask designs for the complete sensor is created using CleWin.

Chapter 4

Eutectic bonding

In this chapter the principle of eutectic bonding is presented and the current scientific knowledge of this method is discussed. The design of the force sensor presented in chapter 3, uses two wafers that are bonded together. Key aspect of the design is that the forces on and subsequent displacement of the top wafer are transmitted to the sensing structures in the bottom wafer via the wafer-to-wafer bond. As the sensing structures are dimensioned to approach the maximum allowable stress, the bond strength required should approach the fracture bulk strength of the Si structures. Various methods of bonding are available, such as anodic bonding, fusion bonding and eutectic bonding. Fusion and anodic bonding require very high processing temperatures, above the melting temperature of most metals and specifically Au. Since Au is used as the metal of the strain gauges and the bonding occurs after the deposition of the metal layer, low temperature processing required in order not to deteriorate the deposited strain gauges. Therefore the use of eutectic bonding is proposed, as its processing temperatures lay well below the melting temperature of Au. A subsequent advantage is that the strain gauges and the bonding use the same metal layer, which can be deposited in the same processing step.

4.1 Introduction

The emerging techniques in silicon micromachining become ever complexer such that the potential benefit from these developments often exceeds the performance limits of these technologies when applied to a single wafer. Wafer-to-wafer bonding offers the designer an extra degree of flexibility and has been used to create various structures such as power devices, integrated sensors and silicon-on-insulator (SOI) wafers. Eutectic die bonding is basically the de facto industry standard on die bonding and the application in silicon wafer to wafer bonding seems like an obvious extension.

The key aspect of eutectic bonding is the decreased melting temperature of the mixture in comparison to the original materials. The melting points of Au and Si are around 1064 °C and 1414 °C, but the eutectic melting temperature is 363 °C, for 19 at.% Si and 81 at.% Au (Figure 4.1). The eutectic liquid will solidify when the temperature decreases below the eutectic temperature or when the concentration ratio of the mixture drops below the liquid line. Because in most cases Si is coming from the substrate, and its availability is unlimited, the solidification starts with the mismatch of eutectic mixture at a certain temperature.

4.2 Literature

Eutectic bonding has been a standard industry process for years, used to fixate and encapsulate semiconductor dies. Scientific knowledge, however, remains fractured, contradictory and therefore, inconclusive. An overview of the articles concerning Au-Si eutectic bonding from the last two decades is given below.

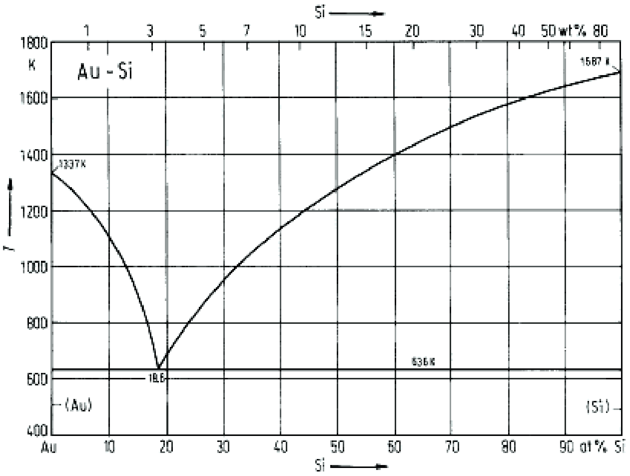

Figure 4.1: Image from Lin et al.: phase diagram of gold and silicon.

4.2.1 Chang et al.

In 1988, Chang, Berman and Shen published an article in which they investigated the gold-silicon interaction under transmission electron microscopy (TEM) [34]. The gold-silicon eutectic is often used to mount a silicon chip to a header. Therefore, the backside of the silicon chip is metalized, which also prevents the silicon from oxidizing what would impair the adhesion between chip and header. After the gold is deposited, before attaching to the header, the gold on the backside is 'alloyed' by heating to above the eutectic temperature. The alloying treatment not only improves the adhesion between the gold and the silicon but also eases the eutectic formation in subsequent bonding to the header. In the article, Chang et al. investigated the structures of Au-Si interactions on the backside of the silicon wafer after the alloying treatment.

A 150 nm gold film is sputtered on a <111> silicon wafer. The wafer is then subjected to heat treatment for 10 minutes at temperatures of 275, 300, 350 and 400 °C in a nitrogen atmosphere furnace. Samples are cut from the wafer for examination with scanning electron microscopy (SEM) and TEM. The deposited gold shows a polycrystalline structure, both as-deposited and after heat treatment below the eutectic temperature. At the interface between the gold and the silicon a silicide (Au_3Si) of several nanometers is formed. The average grains size are 45 nm for Au and 200 nm for Au_3Si. The Au_3Si forms at the silicon side under the original Au-Si interface suggesting that the silicide formation is due to the migration of Au into Si. Many voids are observed in the Au film, which may be the result of the out-flow of Au atoms into Si

Treated above the eutectic temperature, the samples show a very different structure. A 10 min. temperature treatment at 400 °C resulted in the formation of many dark spots of silicon crystals throughout the entire gold film. Most silicon islands are found to protrude through the gold film and have the same orientation as the substrate silicon, which suggests they are grown epitaxially from the substrate. Average grain sizes are in the order of microns, which is much bigger than the fine grains found on the samples below the eutectic temperature. The Au_3Si silicide is not observed in the sample annealed at 400 °C. While the Au film still has a polycrystalline structure, many grains show to follow the orientation of the silicon substrate below.

From these findings, the authors suggest that at 400 °C, a eutectic phase liquid will exist next to two solid phase states, so that the Au film will be partially melted. The melting will probably start at the Au-Si interface and the grain boundaries. The eutectic reaction would therefore result in numerous solid gold grains suspended in a Au-Si liquid solutions, or liquid Au-Si solution trapped in solid gold grains, depending on the amount of silicon dissolved in the gold. When cooled, gold will crystallize first, by the growth of existing gold grains or the creation of new gold grains. The silicon will crystallize epitaxially on the substrate.

4.2.2 Tiensuu et al.

Tiensuu, Bexell, Schweitz, Smith and Johansson presented a method to assemble microstructures with eutectic bonding using a micromanipulator in 1994 [35]. The authors identify a growing need for a general assembly method for all types of microcomponents into larger systems. The bonding should have the ability of joining different materials with various surface conditions. Furthermore, if the different components in the microsystem should be able to communicate, an electrically conductive bond is advantageous. Eutectic Au-Si bonding provides in these desires and has a potential for three-dimensional assembly, low processing temperature and liquid phase bonding. One problem encountered in Au-Si bonding is the presence and formation of surface oxides inhibiting the bonding. Therefore, the experiments are performed in vacuum.

Preliminary experiments are conducted to investigate the bonding process. The bonding tests are carried out at temperatures of 375, 455 and 520 °C in a top-and-bottom heated vacuum furnace at a pressure of $4 - 5\ \mu$Torr. Polished <111> silicon wafers are used and cut in to samples of 5 x 10 mm and 10 x 10 mm. The samples are then cleaned and sputtered with 150 nm Au with part of the samples having a 5-10 nm Cr adhesive layer. A big and small sample are put together, placed in the vacuum furnace and annealed while clamped by a small spring force. The samples are subjected to simple mechanical testing to see if large non-bonded areas exist. The internal structure of the bond is then examined using SEM and TEM.

The authors divide the results into three categories. If the samples can be separated and show signs of bonding at some points, it is considered locally bonded. If the samples cannot be separated it is considered completely bonded, whereas if pieces of the sample broke off along the edge it is considered partially bonded. Samples with only the Au film on the Si substrate showed partial bonding at all three temperatures, while samples with the Cr adhesive layer are locally bonded at 375 °C and completely bonded at temperatures of 455 and 520 °C. When examined with SEM and TEM, the gold layer shows several dark spots, approximately 1 μm in diameter, of which most are voids and some identified as $CrSi_2$ silicide grains. Both the gold and the silicide grains have grown more or less aligned to the silicon matrix.

The experiment shows the best result for the samples with the Cr adhesive layer annealed at 520 °C, which is then used for the microstructure experiment. The microsized elements used in the assembly experiments are made from double polished <110> silicon wafers. First, 0.9 mm wide beams are made by etching rectangular grooves through the wafer with 29% KOH at 80 °C. Parallel <111> planes, perpendicular to the original polished <110> plane, constitute two sides of the beam. The beam is then cleaned and layers of $5 - 10$ nm Cr and 200 nm Au are deposited on four sides of the beam. The beam is cut into microblocks of approximately 860 x 200 x 350 μm. The eutectic bonding of microsized elements is performed in-situ in a SEM, on heated <111> silicon substrates with 100 and 240 nm Au layers. The microblocks are handled using motorized tweezers.

A single microblock is attached to the substrate to examine fracture strengths. To create a microsized assembly, two microblocks are positioned upright on the substrate and are then annealed at 420 °C for a few minutes. The structure is cooled down to below 200 °C, after which the third microblock is placed laying on top of the two standing blocks (Figure 4.2a). The entire structure is clamped and heated to 520 °C for 10 min.

During annealing, the authors observed that the metal film disappeared from a wide, typically 50 μm, region on the substrate around the microblock. Observed during cooling, is the change of position of the microblock when the temperature passed 480-490 °C, even when the structure is mechanically clamped. One sample is seen to tilt sideways as one bottom edge of the microblock is raised about 5 μm relative from the substrate surface. The final micro-bond thickness is very high, typically ranging from 3 to 5 μm.

The single microblocks show little or no bonding to the substrate with 100 nm Au and fairly strong bonds on 240 nm Au. The bonds are not solid but contain numerous voids of varying shapes and sizes. The microblocks have patches of gold matching the shape of the voids in the bond, where the patches do not fill the voids but rather close the lid on top of them. Etching of the fractured surface removed the gold from the bond and revealed the silicon microstructure.

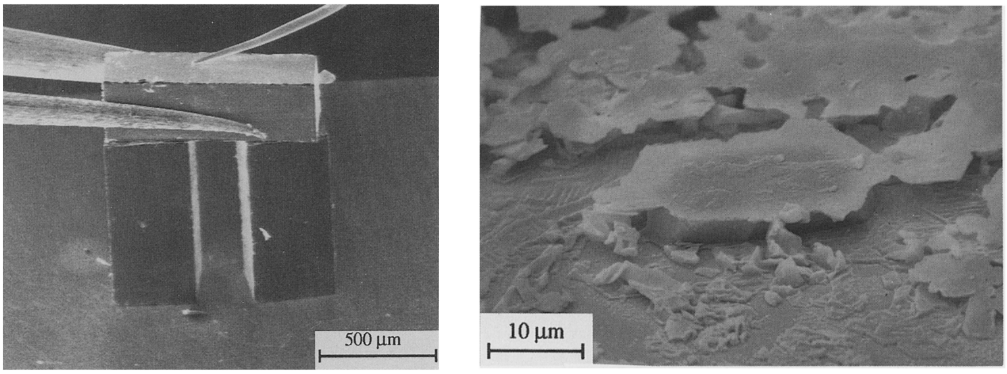

(a) (b)

Figure 4.2: Images from Tiensuu et al. (a) Bonding of the third microblock of the microassembly; (b) The remaining silicon structure of the bond after the gold is etched.

Observed are large faceted structures of $25 - 50$ μm in size, extending from the substrate surface up to the microblock, which are probably epitaxially grown from the substrate (Figure 4.2b).

Void formation is usually ascribed to poor wetting of the eutectic melt due to surface oxides or surface contaminants, but a closer inspection of the voids in the fractured bonds shows a contact angle between the solidified gold and the substrate that indicate good wetting. Together with the oriented growth of the gold grains relative to the silicon substrate, this leads the authors to suggest some other mechanism is involved.

4.2.3 Wolffenbuttel et al.

In that same year, Wolffenbuttel and Wise published their findings on eutectic bonding [36]. Standard 4 inch p-type <100> Si wafers are thermally oxidized after which 30 nm Ti and 120 nm Au are E-beam evaporated. The Ti is deposited to avoid a poor adhesion due to the low surface energy of the SiO_2 layer. The wafers are brought into contact and placed on a hot plate with 100 gr distributed weight for between 5 and 4000 min at temperatures between 350 °C and 400 °C. Heating of the wafer beyond the eutectic temperature results in a change in surface texture due to the formation of fine silicon microstructures on top of the gold surface, which indicates that a 100% bonded area cannot be achieved (Figure 4.3a). The formation of the microstructures seems to occur quicker at higher temperatures, from 10 min at 365 °C to 60 s at 400 °C. Bonded area decreases for higher temperatures, with more than 90% bonded area at 365 °C for 10 min to less than 50% bonded area at 400 °C almost independent of bonding time (Figure 4.3b). As bonding time and temperature are very critical, the authors suggest a additional monitor wafer during processing.

In 1997, Wolffenbuttel published a second paper about eutectic bonding in which he proposes another mechanism plays a role in the formation of the intermediate bonding layer [37]. The poor wettability of gold on an oxide surface results in a poor adhesion. To circumvent this, often an extra layer is used such as Ti or Cr, that adheres well to the oxide layer and subsequently to the deposited Au layer on top. Mating and exposure to a temperature above the eutectic temperature of such wafers have been reported to result in a bond. The general conclusion that this bond is solely based on a eutectic alloying at the interface of the Au-Si system should however be reconsidered, as the observations are not in agreement with those from direct Au-Si interface bonding.

First, the temperature required for a reliable and uniform bond is around 520 °C, which is higher than the Au-Si eutectic temperature (363 °C). Second, unlike the case of a direct Au-Si interface, where Au and Si are epitaxially grown after solidification, the Au-Ti-Si (Au-Cr-Si) system results in silicide grains in a gold layer. It seems the $TiSi_2$ ($CrSi_2$) silicide has replaced the

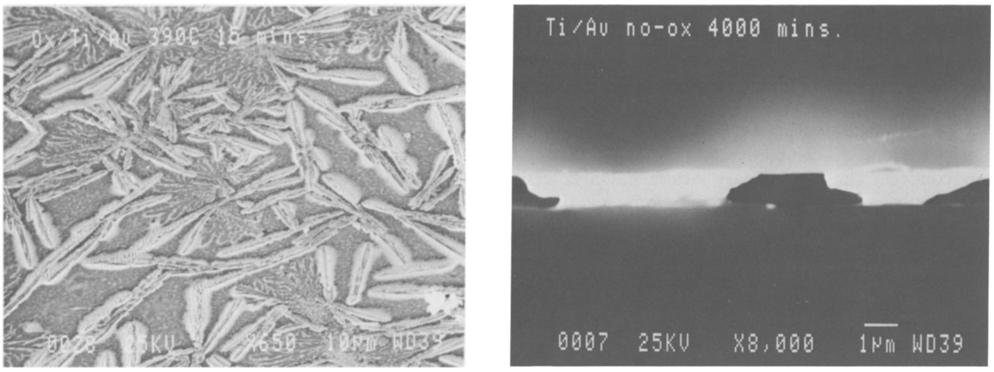

(a) (b)

Figure 4.3: Images from Wolffenbuttel et al. (a) Structure of the Au-Si eutectic material after heating up to 390 °C; (b) Detailed view of the eutectic bond after bonding at 400 °C for 4000 min.

silicon in the eutectic reaction with Au. Ti and Cr are reported to be diffusion barriers and up to some extent that is the reason for their use. However, the very limited solubility of Si in Ti and Cr would prevent the Au-Si eutectic composition from being reached by diffusion of Si through the Ti or Cr into the Au. While the Au-Si eutectic phase plays a dominant role in the bonding of Si-SiO$_2$-Ti(Cr)-Au wafers, the observations suggest that at elevated temperatures silicidation of the Ti(Cr) layer takes place before reaching the eutectic phase.

The author repeated bonding experiments with Si-SiO$_2$-Ti-Au wafers. Standard 4 inch p-type <100> wafers are front-side coated with 20 nm Ti and 100 nm Au using E-beam evaporation. Two wafers were brought in contact in air at room temperature and annealed for 20 or 60 min at 400, 500, 600 and 800 °C in oxygen or nitrogen flow. With a 20 min. anneal only a reliable bond is reported at 800 °C in nitrogen ambient, whereas after 60 min reliable bonds are found at 600 °C and partial bonds at 500 °C. The experiment fails to reproduce the bonding at 500 and 600 °C after 20 min., which lead the author to suggests that cracks in the oxide may have enabled direct Au-Si contact in the earlier experiments.

4.2.4 Bokhonov et al.

Bokhonov and Korchagin published their extensive research in 2000 [38]. The authors acknowledged there are some theories emerging about the crystal structure of the eutectic alloy, while the mechanism of liquid eutectic formation is still open for discussion. Two basic mechanisms of eutectic alloy formation are present. According to the first one, the formation of the eutectic alloy is preceded by the formation of an intermediate layer of a supersaturated solid solution, accompanied by an increase in the concentration of defects in these layers and an increase of the free energy of the system, which would explain why eutectic systems are easily melting. The second mechanism states that the interaction of surface atoms occurs in microregions of physical contact between the conjugated crystal phases and a transitional epitaxial zone is formed. The formation of these zones should lead to a decrease in misalignment and stress on the interface and to an increase of the elastic energy of the interface. The formation of epitaxial zones leads to a weakening of the bond in the surface layers of contacting crystals, which provides the decrease of temperature at which the system passes into the liquid phase.

Below the eutectic temperature, deposited Au films on Si substrates lead to a formation of a diffusion interface between the two layers. Silicon oxides has been observed forming on top of the Au film, which leads to believe that the Si predominantly diffuses through the Au layer. Also, it is demonstrated that the growth rate of the silicon oxide on the Au layer deposited on a <110> Si surface is five times higher than on a Au layer deposited on a <111> Si substrate.

The structure of the liquid alloy is not well know, with sources claiming to have observed

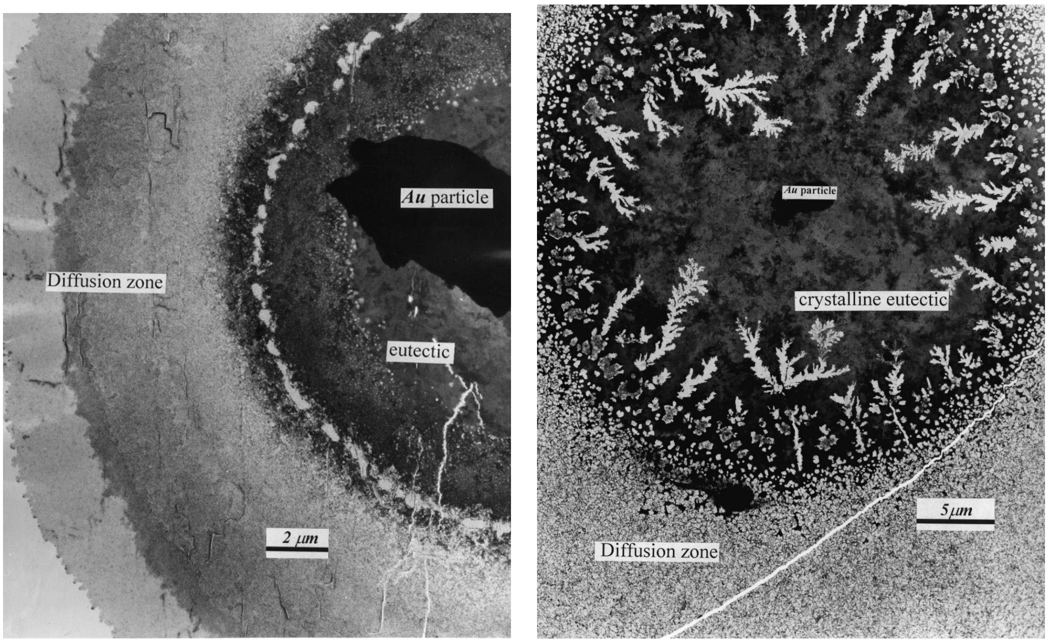

(a) (b)

Figure 4.4: Images from Bokhonov et al. (a) SEM image of the diffusion and eutectic zones formed during heating with a high intensity electron beam; (b) Dendrite crystallization of the solid eutectic Au-Si alloy obtained during isothermal heating above the eutectic temperature.

(metastable) compounds in quenched eutectic alloys, while others could not reproduce these results and found only separate states of Au and Si. The authors therefore conducted a series of in-situ SEM and TEM experiments on the forming of the eutectic alloy from Au particles placed on <100> and amorphous Si films and from Si particles deposited on a single-crystal Au film. The samples are then heated, either with the electron beam of the microscope or with a sample heating plate.

When the gold particle deposited on the amorphous silicon was heated with a low intensity (10^{-2} A/cm^2) beam, a rapid propagation of the interface from the particle into the Si film is observed. The morphological characteristic of this product layer is the formation of periodic concentric layers of different intensity. The reaction occurs below the gold melting point, since no changers are observed in the Au particle, which remained solid. If the Au particle is heated with a higher intensity (10^{-1} A/cm^2) beam, besides the propagation of the reaction front and the formation of concentric product layers, a formation of the eutectic Au-Si is observed in the vicinity of the Au particle (Figure 4.4a). In both cases, the concentric product layers are mixtures of polycrystalline silicon and an amorphous substance. After cooling, the eutectic phase reveals the presence of branched, dendrite silicon crystals distributed in polycrystalline gold. Occasionally, also a metastable compound of silicon and gold is found in the eutectic region.

When the amorphous silicon with the gold particle are heated with the sample heater, below the eutectic temperature, no concentric rings of different intensity are observed, and a uniform product layer is formed. The diffraction pattern of the layer shows again a mixture of polycrystalline Si and an amorphous material. When the temperature is increased to above the eutectic temperature, a eutectic alloy is formed around the particle, where an increase of the eutectic zone is accompanied by a substantial decrease of the Au particle. Cooling of the eutectic alloy leads to dendrite crystallization of the Si in a polycrystalline Au matrix (Figure 4.4b). In this case, no metastable compound are found.

During the investigation of the gold particle on <100> crystalline silicon, Bokhonov and Korchagin discovered a substantially different characteristic of the formation of the eutectic alloy.

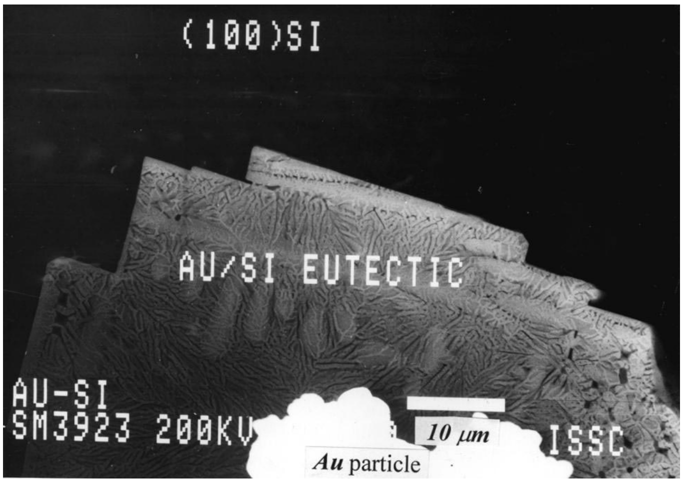

Figure 4.5: Image from Bokhonov et al.: the formation of dendrite silicon crystals and crystalline gold on the <100> silicon surface.

When heated with a high intensity beam, the Au-Si eutectic showed a flat reaction front, which strictly followed the crystal orientations of the <100> silicon (Figure 4.5). Along with this, in regions of the crystalline silicon farther away from the reaction front, the authors observed the deposition of square-shaped crystals and fine gold particles. The crystals turned out to be gold silicides. Cooling of the eutectic melt leads to dendrite Si crystals and Au crystals in the crystal Si matrix. The crystallization and decomposition of the eutectic alloy was accompanied by a crystal phase volume decrease when compared to the liquid phase. After cooling, a transition zone between the crystal eutectic region and initial Si matrix is observed, which is composed of gold silicide particles with sizes in the order of several nm.

When a silicon particle was placed on a <100> gold film at a temperature below the eutectic temperature, no structural and morphological changes are observed. Increasing the temperature to above the eutectic temperature causes the creation of pores in the region of the gold adjacent to the Si particle. The pores show rectangle shapes, oriented along the <100> and <010> direction of the Au crystal. The pore size increases with increasing annealing time and the formation of tentacles between the Si particle and Au film is observed.

The authors suggest that the crystallization of amorphous silicon during annealing with the gold particle is directly connected with the formation of amorphous metal silicides. Supersaturation of the amorphous Si during the diffusion of Au leads to decomposition together with the evolution of crystalline Si and amorphous silicides. Under electron beam heating, concentric layers are observed which differ in the concentration of amorphous Au silicide. The electron beam heats the sample only locally which can give rise to large temperature gradients in the substrate. Diffusion and also supersaturation are dependent on temperature and the temperature gradient could explain the periodic changes in supersaturation. Isothermal heating will not create different supersaturation values and no differences in intensity are observed. The saturation of the silicon, together with the voids that are observed in the gold film with the Si particle, leads the authors to suggest that the diffusion between Au and Si is dominated by the transfer of Au atoms into the Si.

Another unusual fact discovered, the oriented growth of the liquid eutectic phase in the <100> Si substrate is compared to the dissolution of etch pits. As the etching characteristics depend, among others, on the nature, crystallographic orientation and present defects of the crystal, nature and composition of the etchant, the authors suggest similar factors might also determine the shape of the melt on the surface during formation of the liquid eutectic.

The metastable compounds found after cooling when heated with the electron beam could also be explained by the temperature gradient, which would lead to the quenching of the eutectic melt. This would prove that a metastable chemical compound is formed in the liquid eutectic phase.

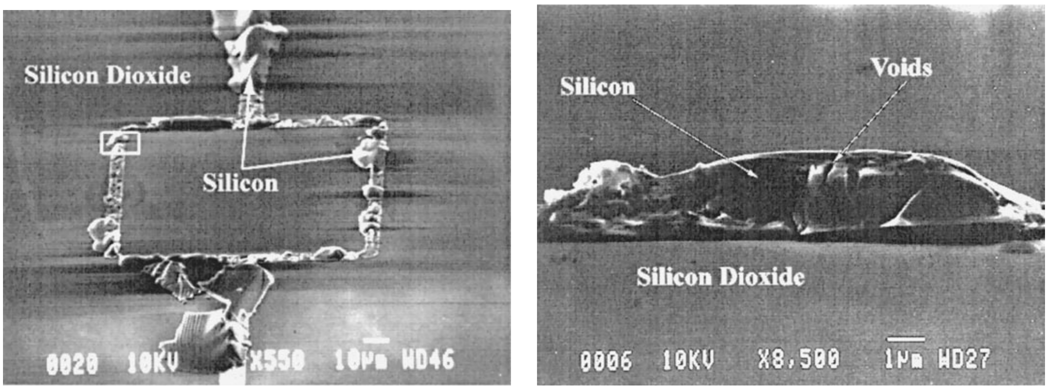

(a) (b)

Figure 4.6: Images from Cheng et al. (a) SEM image showing localized eutectic bonding where silicon transferred to the substrate; (b) Close view SEM image showing the voids in the silicon debris after gold etching.

The crystallization of gold silicide in region further away from the eutectic zone has the same cause, as the beam might lead to overheating and evaporation of the sample. The evaporating melt deposits on cooler parts of the substrate, which causes the stabilization and quenching of metastable Au silicide.

4.2.5 Cheng et al.

While eutectic bonding may in general provide in a relatively low thermal budget, lower processing temperatures may be desirable. Cheng, Lin and Najafi presented their method of localized bonding in 2000, in which the substrate temperature remains low [39]. The localized heating is provided by using microheaters instead of global heating furnaces. The microheaters are constructed so that heating is restricted to a small region, which is surrounded by insulation material. A silicon dioxide layer with thickness 1 μm is grown on the device substrate for electrical and thermal insulation. Patterned 500 nm gold lines with widths of 5 and 7 μm are sputtered on top and used as the heating and bonding material. When an electrical current is applied, the temperature of the microheater rises to activate the bonding process.

A silicon cap is placed on top of the substrate with the microheaters and a contact pressure of 1 MPa is applied. A 270 mA electrical current is applied to the gold lines for 5 min. The bonding temperature is estimated to be 800 °C according to both an electrothermal model and experimental measurements of resistivity changes. Inspection after the bond is forcefully broken reveals the fracture occurs in the silicon cap, with parts of it transferred to the substrate (Figure 4.6a). The substrate is then dipped into gold etchant for 30 min, after which voids appear in the surface of the silicon debris (Figure 4.6b). The authors propose these voids are from a Au-Si composite, as the etchant does not attack silicon. It is suggested that the gold atoms have diffused into the substrate during the bonding. With an average diffusion length of 11 μm the authors calculate a bonding temperature of 750 °C, close to their earlier estimate.

A conventional eutectic bonding process is conducted in an oven for the purpose of comparison. The processing temperature is first ramped to 410 °C in 10 min and kept there for 10 min before being cooled down in 40 min. When the eutectic bond is forcefully broken, nonuniform bonding is observed. The authors suggest that this is due to the lower bonding temperature as compared to the localized bonding. The diffusivity and solubility of gold into silicon increases with temperature, so higher processing temperature is preferred for eutectic bonding. Localized bonding can provide a method to achieve higher bonding temperatures while keeping the substrate at a relatively low temperature.

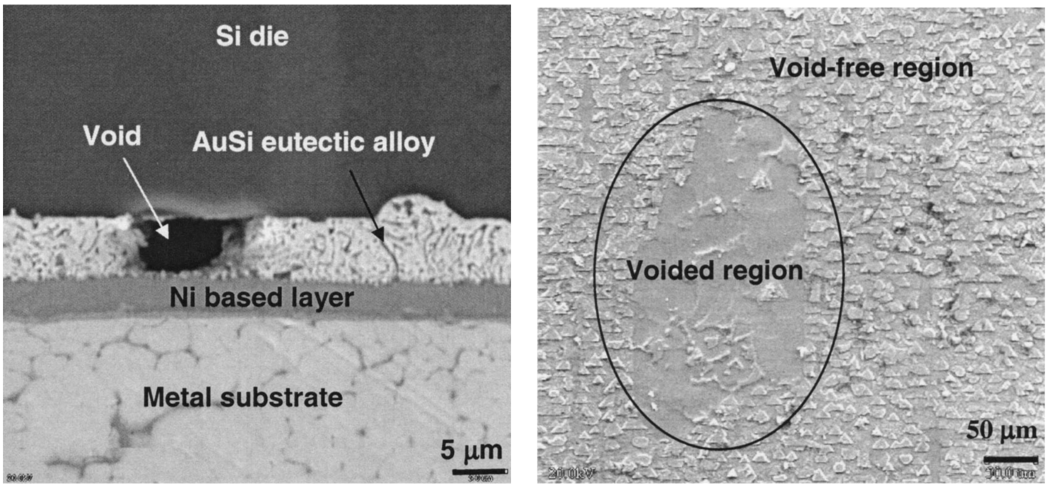

(a) (b)

Figure 4.7: Images from Jang et al. (a) Typical cross-sectional SEM image of the Au-Si eutectic showing a void; (b) Exposed backside of the <111> silicon die. The non-voided region has numerous triangle etch pits whereas the voided region shows a smoother morphology.

4.2.6 Jang et al.

The dissolution behaviour of different crystalline orientations of silicon were further investigated by Jang, Hayes, Lin and Frear and presented in 2004 [40]. In the semiconductor industry eutectic bonding is used for a variety of applications such as silicon die bonding on metal or metalized ceramic substrates. For Au-Si die bonding, Si is provided from the Si die. Therefore, the interfacial reaction between the substrate and the eutectic phase is a key factor for the control of the die bonding process. In the study, the focus lays on the morphology between the Si die and the Au-Si eutectic alloy and differences between <100> and <111> crystalline wafers. Rectangular samples are diced from both types of wafers. The back side of the sample is sputtered with 1.2 μm Au. The sample is placed on a metal substrate with a 3 μm Au layer and heated to 420 °C for 1, 2 and 3 min.

Cross-sectional inspection of the bond revealed a clear layer of Au-Si eutectic alloy, in which voids are regularly found, with sizes ranging from 5 to 100 μm (Figure 4.7a). There is no difference found in external shape of the void between <100> and <111> silicon. However, a different metallurgical morphology is observed. The Au-Si alloy is etched away to inspect the die interface. It is observed that the etched morphology of the Si where there was a void differs from the Si region that had contact to the eutectic phase. The voided region tends to be smoother than the void-free region which is characterized by numerous craters. The craters take the form of inverted pyramids in the <100> substrate and of flat triangles in the <111> substrate (Figure 4.7b). The pyramids are usually much deeper than the triangles, suggesting that the eutectic reaction is faster at the <100> substrate.

The authors found that even in the voids, a thin layer of Au-Si eutectic alloy is present on the <100> substrate, whereas the <111> substrate is still coated with a thin Au layer in the voided regions. They propose that the eutectic reaction at the <100> substrate initiates everywhere but the quickly formed inverted pyramid craters act as a sink and pull away the Au-Si alloy from the bonding layer (Figure 4.8a). The thin Au film on the <111> substrate shows that the Au did not react with the Si. This suggests the present of an inert layer between the Si and Au that prevents the reaction, such as oxide (Figure 4.8b). The initial oxidation of <111> silicon is much greater than that of <100> silicon, what would explain why no oxide is found on the <100> substrate under the same processing conditions.

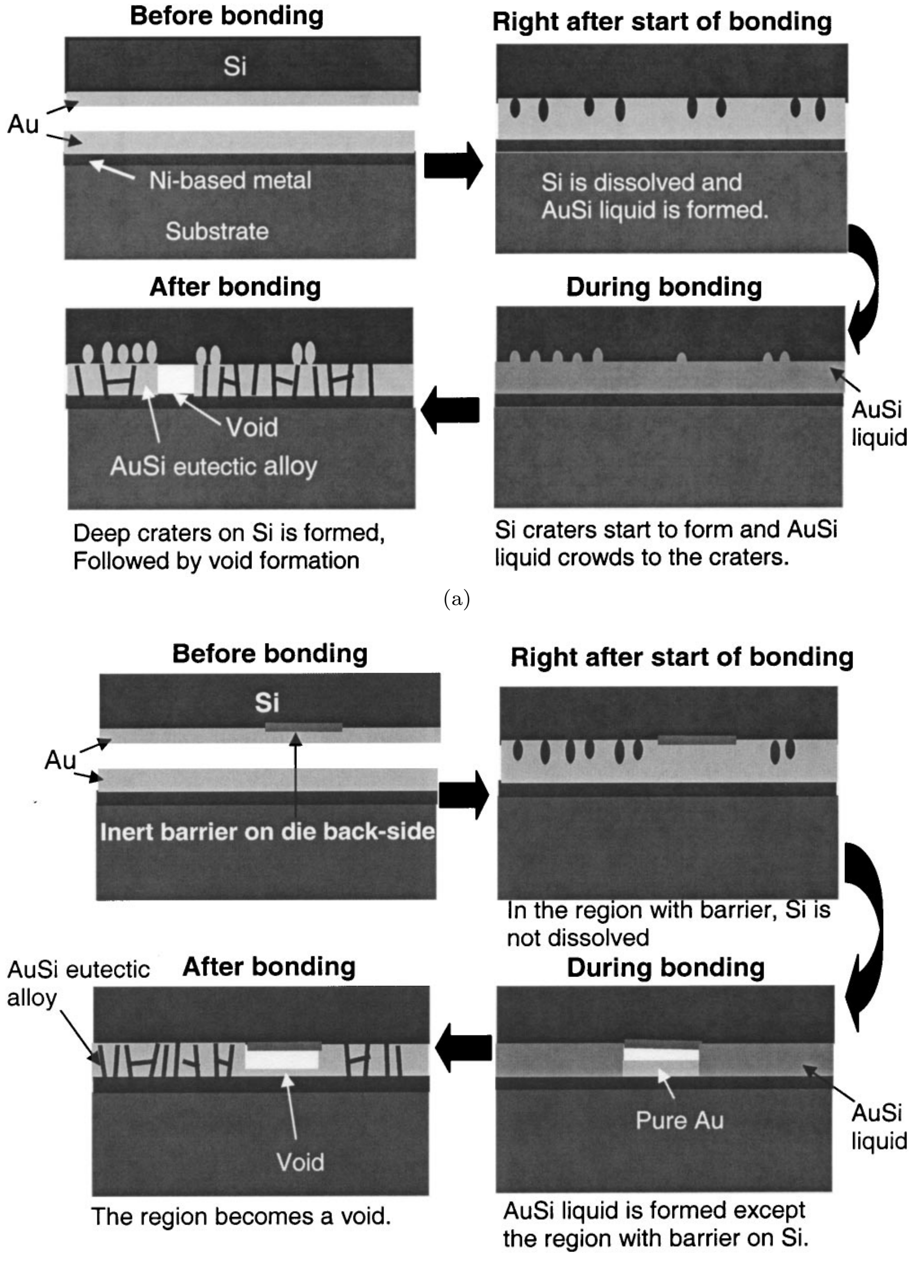

(a)

(b)

Figure 4.8: Proposed void formation from Jang et al. (a) Void formation on <100> silicon; (b) Void formation on <111> silicon.

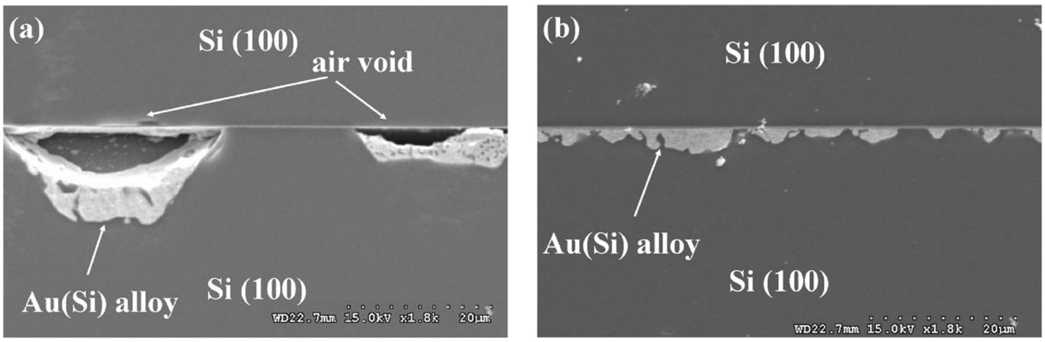

(a) (b)

Figure 4.9: Images from Chen et al. (a) Cross-sectional SEM image of the eutectic bond on crystalline silicon; (b) Image of the eutectic bond on amorphous silicon.

4.2.7 Chen et al.

Chen, Lin and Liu presented their work on amorphous Si/Au wafer bonding in 2007 [41]. They state that, as the requirements for wafer bonding are much stricter than those for conventional die attachment and sealing applications, a uniform and void-free bonding interface is required for applicable wafer bonding. However, voids and craters are often formed at the Au-Si bonding interface and have a serious effect on the reliability of the bonding layer. The authors compared the bonding on amorphous silicon with that of bonding on crystalline silicon. They prepared a <100> silicon wafer with 50 nm Cr, 100 nm Pt and 10 μm Au, which was subsequently bonded with either a <100> silicon wafer or with a wafer on which a layer of 1 μm amorphous silicon was deposited. The wafers are then bonded for 10 min at 400 °C and a pressure of 200 N/cm^2. After bonding the samples are forcefully broken and the bond interfaces are examined with scanning electron microscopy (SEM).

SEM images of the crystalline silicon revealed relatively big craters (Figure 4.9a). Owing to the anisotropy nature of crystalline Si the crystalline Si/Au reaction rate is highly dependent on the crystallography of the Si wafer. Si dissolution into the Au proceeds preferentially along particular planes, usually the planes with highest surface energy. In silicon, the <111> plane has the lowest surface energy, which is thus the most resistant to dissolving in Au. This means that as Si reacts with Au, facet craters or inverted pyramids form on the surface. In addition, it is observed that big air voids are formed inside the craters, which is suspected due to the difference in density between Si and the liquid Au-Si alloy, being 2.33 and 18.64 g/cm^3. The air voids result in a weak bonding interface and poor thermal and electrical conductivity across the bonding interface.

On the bond interface of the amorphous silicon, much smaller craters are observed. Also, no air voids are found (Figure 4.9b). Suggested is that because the dissolution of amorphous Si into Au has no preferential orientation, a uniform layer of Au-Si eutectic alloy if quickly formed at the interface. When the thin layer of amorphous silicon is consumed by the reaction, the eutectic reaches the crystalline Si. However, since the eutectic alloy already contains portions of Si, the reaction with the underlying Si is much smaller which prevents the formation of big craters. Therefore, an amorphous Si coating layer on a otherwise crystalline wafer will result in stronger and uniformer bond as the rapid reaction of the Au with the amorphous Si gives a uniform bonding layer and subsequently slows the reaction with the underlying crystalline substrate.

4.2.8 Lin et al.

In 2009, Lin, Baum, Haubold, Frömel, Wiemer, Gessner and Esashi presented a conference paper in which several process parameters are examined [42]. To see if the concentration ratio has an effect on the bond strength, samples are prepared in which the amount of Si and Au is clearly defined. Therefore, the wafers are first coated with a 100 nm thick oxide layer, on which 600 nm

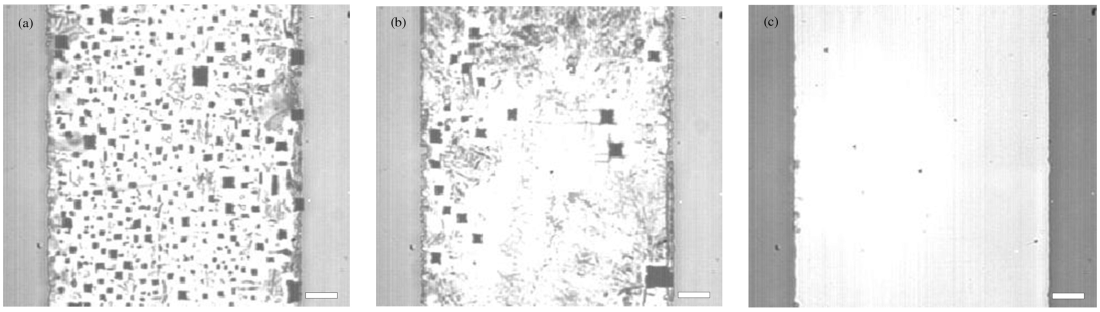

(a) (b) (c)

Figure 4.10: IR images of the Au-Si bonding interface from Jing et al. (a) High density of dark spots; (b) Low density of dark spots; (c) Nearly no dark spots.

of amorphous Si is deposited. On one wafer of each bonding pair, 30 nm Cr is deposited as an adhesive layer after which a Au layer with thicknesses of 750, 500 or 250 nm is deposited, which leads to a Si at.% of 57.5, 67.0 and 80.3 in the bonding layer stack. It is observed that the bond strength is inversely proportional to the amount of Si, as the yield decreased from 100% to 96% and 40% for increasing Si at.%. Bonding experiments performed without the Cr adhesive layer result in insufficient bonding, as the samples can be easily separated. Because SiO_2 was used to clearly define the amount of Si and prevent the eutectic to reach the bulk, the bond strength is shown to be compromised, as the fractures occur mostly on the oxide interface.

Next, the authors investigated the influence of the process temperature and pressure. Patterned, 350 or 500 nm thick Au layers are deposited on a SiO_2 wafer and then bonded with a single crystalline Si wafer. The temperate ranged from 390 to 400 °C and the pressure varied from 100 to 500 kPa, for a period of a few minutes up to 15 min. The authors found that high temperature of pressure leads to an uncontrollable overflow of the eutectic liquid, while a decrease in temperature, pressure or both prevented the overflow from occurring. Controlling the flow of the eutectic liquid is important, as it may lead to short circuits in devices with electrical connects and poor bonding.

4.2.9 Jing et al.

Jin, Xiong and Wang presented a method to qualitatively evaluate the Au-Si eutectic bond strength using infrared microscopy in 2010 [43, 44]. A 2 μm thick silicon oxide is grown on double polished n-type <100> silicon wafers. Then, 50 nm titanium and 400 nm gold is deposited using sputtering equipment. The titanium layer is used as an adhesive layer to ensure bonding to the oxide layer. The wafer is bonded to a bare silicon wafer in a vacuum bonder, for 30 min at 400 °C, with an applied pressure of 0.8 MPa. When studied with infrared microscopy, the authors found that there is a spread of darker spots over the samples on the wafer (Figure 4.10). When the samples are diced, some samples separated from the stress originating from the dicing and it is found these samples also had very few dark spots. The samples are then subjected to bond strength testing and again it is found that there is a correlation between the number of dark spots on the bonding interface and the bond strength. When the bonding interfaces are etched with Au etchant, the dark spots turn out to be craters in the form of inverted pyramids (Figure 4.11a). When a <111> silicon wafer is used, the spots take the form of triangles (Figure 4.11b). It is therefore proposed the voids that are found after etching are spots in which the eutectic phase is formed. More dark spots means that the eutectic reaction occurs at more places and subsequently the bond strength is increased.

Apart from the anisotropy of the eutectic reaction, the formation of the alloy also seems to be nonuniform, as craters are found at some placed but absent at others. The authors suspect this is because of the formation of a native oxide on the silicon substrate [45, 46]. Even a thin oxide layer would work a diffusion blocker, preventing the Si and Au to transfer. Therefore, 50 nm Ti and

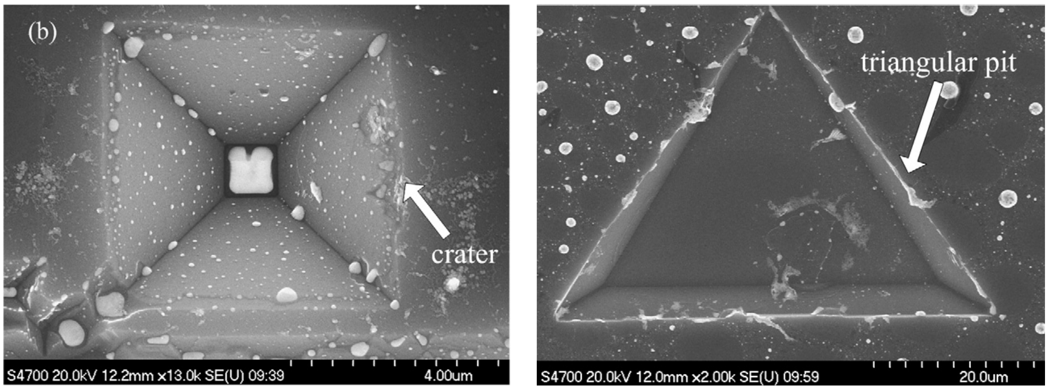

(a) (b)

Figure 4.11: Images from Jing et al. (a) SEM image of the bare <100> silicon surface after bonding; (b) SEM image of the bare <111> silicon surface after bonding.

200 nm Au are also sputtered to the previously bare silicon wafer, because the Ti decomposes the native oxide on the silicon surface. This time, a uniform reaction is observed, without big craters but with a uniform eutectic layer forming at the interface. In 2011, an experiment was presented in which a layer of amorphous silicon is deposited as well as the Ti and Au metal layers, providing all material needed for the eutectic bond such that the silicon substrate is no longer needed. With this method, other wafer pairs, such as glass, can also be bonded [47].

4.3 Discussion and conclusions

Since the initial scientific papers on eutectic bonding were presented, research has progressed into fundamental understanding as well as applied technological advances. The Au-Si eutectic provides a adequate way of wafer bonding which is compatible with on-chip electrical connects because of its relatively low processing temperature. Because the bond is formed from a liquid phase, surface roughness of the bonded substrate is not of great importance. Other process parameters reveal to be more critical, as the formation of voids in the eutectic layer and the Si to Au ratio of the mixture show to have a strong influence on the bond strength. Many articles show that the dissolution of the silicon substrate by the eutectic melt has an anisotropic nature, as it follows the crystalline orientations of the silicon matrix. The dissolution is said to be preceded by a diffusion mechanism which would provide the the ratio of gold and silicon that enables liquefaction of the mixture. Whether this diffusion is dominated by gold atoms flowing into the silicon, or silicon atoms traveling through the gold matrix is still open for debate as experiments have found clues that lead to either conclusion.

On the composition of the eutectic alloy, experiments point towards the existence of a metastable gold silicide during the liquid phase. When the liquid is quickly cooled or quenched, traces of this compound can be found. However, when the eutectic cools gradually, the compound decomposes into separate crystals of gold and silicon. These crystals are found to growth epitaxially on crystalline substrates, which would result in substantial bonding strength. Results on the volume change of the eutectic alloy compared to the separate gold and silicon phases are contradictory. Tiensuu et al. [35] mention the substantial increase of volume during bonding, while others [40, 41] state a decrease in volume as the density increases. From the perspective of energy conservation it is clearly counterintuitive for the liquefaction of the mixture to be accompanied by a volume increase.

However, the conflicting experimental findings may be unified by considering the liquefaction and subsequent solidification of the eutectic mixture. As the liquid eutectic is adopted to have a higher density than the separate crystals, solidification into segregate gold and silicon crystals would result in an increase in volume. It is mentioned the increase in eutectic volume is preceded by the gold being drawn towards the bonding interface from a wide region. This would result in an increase of eutectic material but as the alloy is still liquid with a higher density, an increase of mass may not immediately become apparent as an increase in volume. As the inflow of gold stalls, the ratio of gold to silicon changes as the substrate provides unlimited silicon. This leads to the solidification of the eutectic melt into separated gold and silicon crystals and the increase of material might first become apparent.

Surface conditions of the substrate are found to have a big effect on the reaction speed and void formation. As even a thin native oxide on the silicon prevents the eutectic reaction from taking place, the initiation of the eutectic melt tends to have a nonuniform behaviour. In amorphous silicon this may not have too big effects, as the eutectic alloy spreads throughout the silicon, in crystalline silicon the eutectic follows the crystal orientation which leads to specifically oriented craters. These craters are suggested to facilitate a pulling in of the eutectic melt which would lead to the formation of voids and subsequently a weaker bond.

To provide in a more uniform eutectic reaction, adhesive metal layers such as titanium or chromium, are use to decompose the surface oxides. While these materials are known to provide a better adhesion of gold to silicon, these intermediate layers would also have an effect on the diffusion and initiation of the eutectic reaction as they would prevent the gold to come into contact with the silicon. Wolffenbuttel [37] suggests the titanium and chromium take place in the eutectic formation by forming silicides which take the place of the silicon crystal in the eutectic melt. However, subsequent experiments show no findings towards this theory and the exact influence of the adhesive metal layers on the eutectic bonding process remains the subject of further scientific investigation.

Chapter 5

Experiments

This chapter presents the experiments conducted to determine the eutectic bond strength and the influence of intermediate metal adhesive layers. As the bonding is used to attach structures of the sensor used to transmit and withstand the mechanical load, knowing the value of the bond strength is crucial in designing and dimensioning the force sensor. The first experiment is conducted to find the optimal processing time and to see if there is any influence by the use of an adhesive metal layer. After this, the bond is quantitatively investigated in an attempt to find the bond fracture strength. To examine the influence of the intermediate adhesive layers, a third experiment is conducted in which layer stacks with different thicknesses of Ti and Cr are annealed at high temperatures. After this, bond strength experiments are conducted for each layer configuration.

5.1 Initial bonding experiment

An initial investigation into eutectic bonding is performed as part of another device development, by K. Ma. The experiment is conducted to find the optimal processing time and see if the use of an adhesive metal layer has any influence on the bond.

5.1.1 Experiment

Standard <100> Si wafers are used, on which a 500 nm layer of SiRN is deposited. On this, a 10 nm Cr adhesive layer and 100 nm Au are deposited. The wafers are bonded with bulk <100> Si wafers without metalization. The two wafers are aligned and placed in a EVG-501 vacuum wafer bonding system, where they are heated to 375 °C and bonded for 5, 30, and then, 15 min. To see how the bonding performs using patterned structures, bottom wafers are created with 500 nm thick poly-Si pillars, of 45 μm radius, on top of the 500 nm SiRN layer. The top wafer is also coated with 500 nm SiRN and 500 nm poly-Si. Then, a 100 nm Au layer is deposited upon both the bottom as well as the top wafer. The samples are placed in the vacuum bonder and bonded for 15 min. at 375 °C. The wafers are then diced and the bond is forcefully broken to inspect the bond interface using scanning electron microscopy (SEM).

5.1.2 Results

The results of the experiment are given in Table 5.1, as well as the configurations of the wafers. Processing for 5 min. provides no bonding, as the wafers show to be loose upon unloading. Furthermore, optical inspection shows no Au is transfered to the top wafer. This shows that a bonding time of 5 min. is too short. When the bonding time is increased to 30 min., a weak wafer scale bonding is achieved. However, all Au is transfered into the top wafer suggesting the bonding time might be too long. The wafers are then bonded for 15 min. First results show that the bonding is achieved at wafer-scale. The wafer is then sawed and diced into pieces of 5 x 5 mm. All samples remain bonded, showing that chip-scale bonding can be accomplished within 15 min.

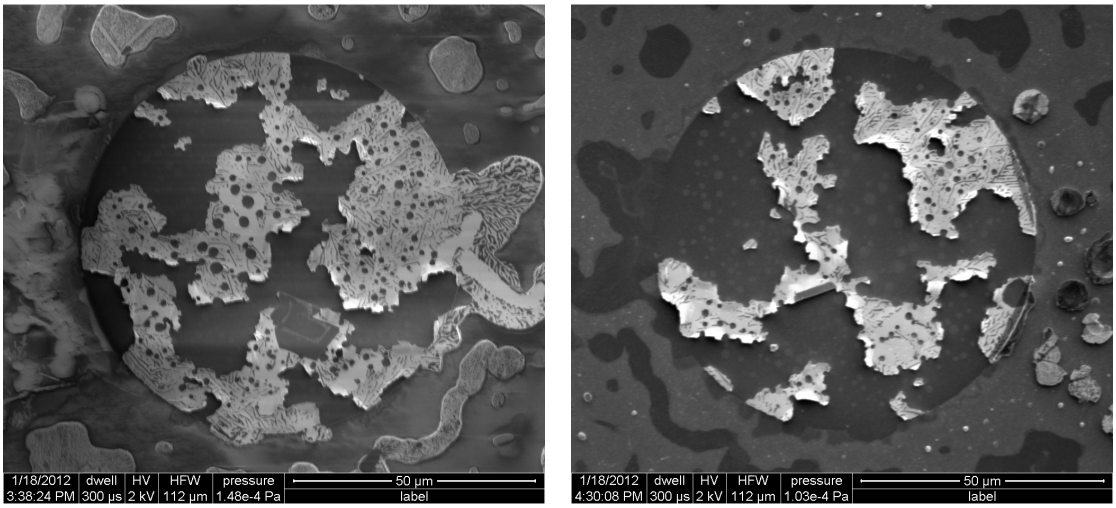

(a) (b)

Figure 5.1: SEM images of the bond interface after bonding for 15 min. (a) The 500 nm poly-Si pattern with parts of the deposited Au; (b) The mirrored imprint on the Si top wafer.

Figure 5.1a shows a SEM image of the poly-Si structure after the bond is broken. Figure 5.1b shows the corresponding section on the top wafer. In both images, portions of the eutectic melt are clearly visible next to the pillar, appearing to have flown around the pattern. On top of the patterned poly-Si, portions of the Au film are found. The film seems to stick to the poly-Si only loosely, as flakes of the Au are clearly curling up. The fracture of the bond is only visible in the Au film, and no clear fractures are observed in the poly-Si.

The bad adhesion of the Au on the poly-Si might be improved using an adhesion layer. Therefore the experiment is repeated with 10 nm Ti underneath the Au layer on both the bottom and top wafer. Figure 5.2 shows the SEM images after the bond is broken. It seems the eutectic reaction on the poly-Si next to the pillars is prohibited by the Ti layer, as it shows a clear uniform surface with no portions of eutectic melt. However, bonding is achieved with the poly-Si structures as breaking of the bond results in fractured pillars. Most of the bond fracture however, runs over a clear flat surface. Closer inspection shows that this is the poly-Si/SiRN interface, which shows the eutectic bond strength is higher than the bond strength of poly-Si on SiRN. Figure 5.3a shows the fractured bond in which a portion of the poly-Si is pulled from the top wafer, Figure 5.3b shows the subsequent crater. Also visible are peaks that appear to have grown from the patterned area.

5.1.3 Discussion

The initial bonding experiments provide information on the bonding time and the influence of the intermediate adhesion layer, both in concordance with earlier findings in literature. The experiment with the Ti layer also shows the retreat of the metal layer around the areas of bonding. However, the eutectic reaction seems not confined to the patterned area, as crystal peaks are visible that seem to have grown from the poly-Si pattern. Clearly, this is something that has to be controlled if eutectic bonding is used to bond MEMS devices, as it would have detrimental effects on adjacent structures or electrical connects. Fractures on the interface of broken bonds show the bonding strength achieved is higher than the bond of the poly-Si layer on the SiRN. The exact value of the bond strength however, cannot be determined as the bonded area is not clearly defined.

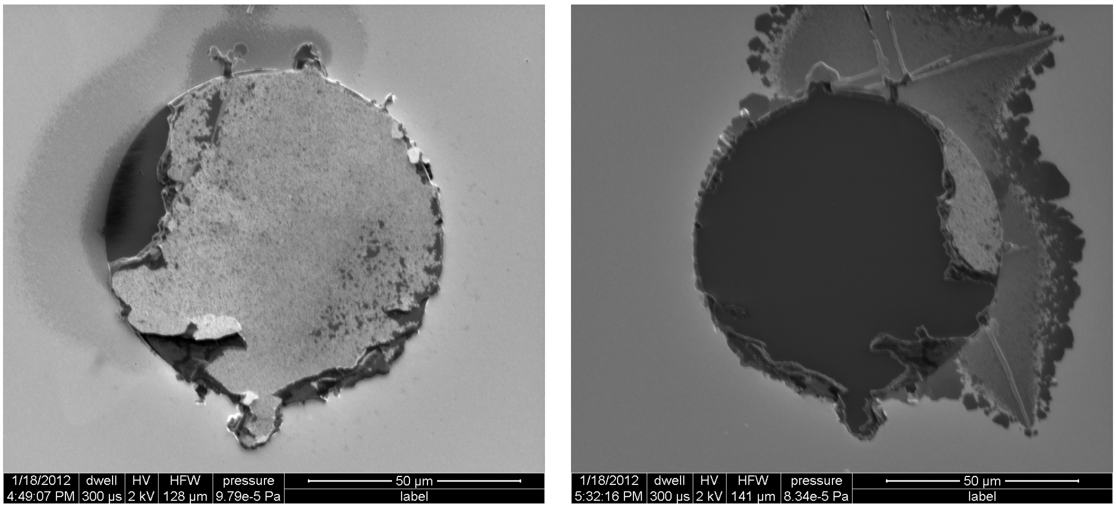

(a) (b)

Figure 5.2: SEM images of the bonding using a Ti adhesion layer. (a) Upon breaking the bond, the poly-Si layer is pulled from the top wafer and is shown here on the poly-Si pattern from the bottom wafer; (b) The remaining crater in the top wafer.

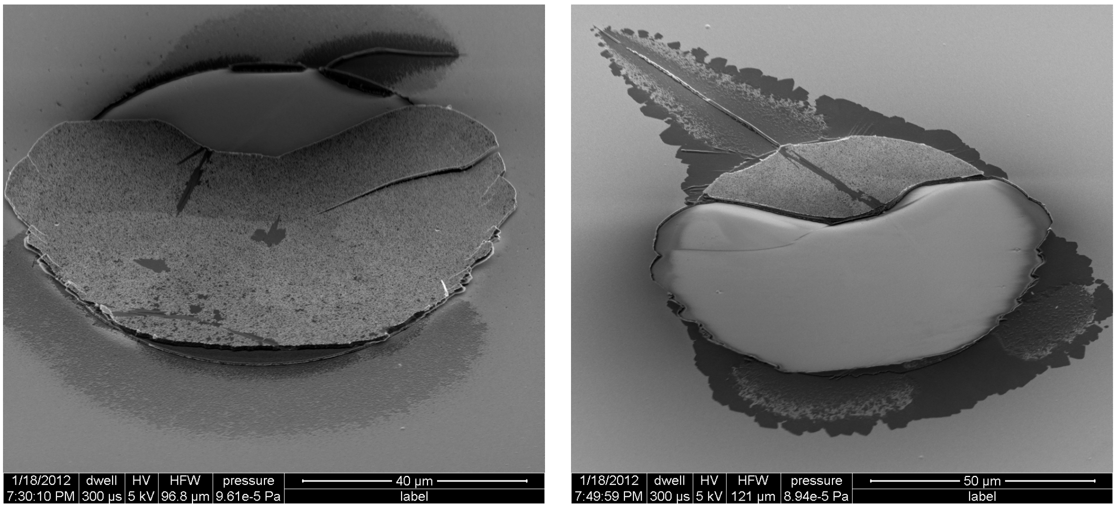

(a) (b)

Figure 5.3: SEM images of the bonding with the Ti adhesion layer. (a) The poly-Si layer is bonded to the poly-Si pattern and released from the top wafer; (b) A crystal tentacle is grown from the pattern.

	Bottom wafer	Top wafer	Bond time	Result	Conclusion
1	Bulk Si 500 nm SiRN 10 nm Cr 100 nm Au	Bulk Si	5 min.	No Au transfer to top.	Bonding time too short.
2	Bulk Si 500 nm SiRN 10 nm Cr 100 nm Au	Bulk Si	30 min.	Wafer-scale bonding. All Au transfered to top	Bonding time might be too long.
3	Bulk Si 500 nm SiRN 10 nm Cr 100 nm Au	Bulk Si	15 min.	Sawed and diced. Chip-scale bonding.	Works for full-area bonding.
4	Bulk Si 500 nm SiRN 500 nm poly-Si 100 nm Au	Bulk Si 500 nm SiRN 500 nm poly-Si 100 nm Au	15 min.	Sawed and diced. Chip-scale bonding.	Actual bond strength unknown.
5	Bulk Si 500 nm SiRN 500 nm poly-Si 10 nm Ti 100 nm Au	Bulk Si 500 nm SiRN 500 nm poly-Si 10 nm Ti 100 nm Au	15 min.	Adhesion improved.	Actual bond strength unknown.

Table 5.1: Overview of the configurations and results of the initial bonding experiments.

5.2 Bond strength experiment

The next set of experiments is conducted to find the eutectic bond strength. This time, chromium is used as an adhesive layer. The top wafers are patterned with pillars to create a defined bonding area. Several samples with pillars of different diameters are bonded. The samples are pulled from the bottom wafer and the required force to release a sample is measured. As the number and area of the pillars is known, the fracture strength of the bond can be determined via $\sigma = F/A$.

5.2.1 Experiment

The bottom and top wafers are standard <100> Si wafers, on which 10 nm Cr and 100 nm Au is deposited. On the top wafer, pillars are patterned using DRIE etching. Via this pattern, the bond only occurs on the defined area of the pillars. Apart from the pillars, the gap between the top and bottom wafer is 800 nm. A schematic cross-section of the top and bottom wafer is given in Figure 5.4. The wafers are bonded in vacuum bonder, at 375 °C for 15 min. After bonding, pull tests are performed on each sample to find the force needed to break the bond.

5.2.2 Measurement setup

To measure the force needed to break the bonds of a sample, the bottom wafer is glued on an aluminum fixture, which is mounted to a load-cell (Vishay Tedea-Huntleigh 1022). A metal bar is glued on each sample on the top wafer, to which a load can be attached via a spring (Figure 5.5). While the load-cell continuously measures the force, the load is increased until the sample breaks. Pull tests are performed on samples with pillars of different diameter. Results of the pull testing are shown in Figure 5.6. The expected bond strength is indicated by the red line.

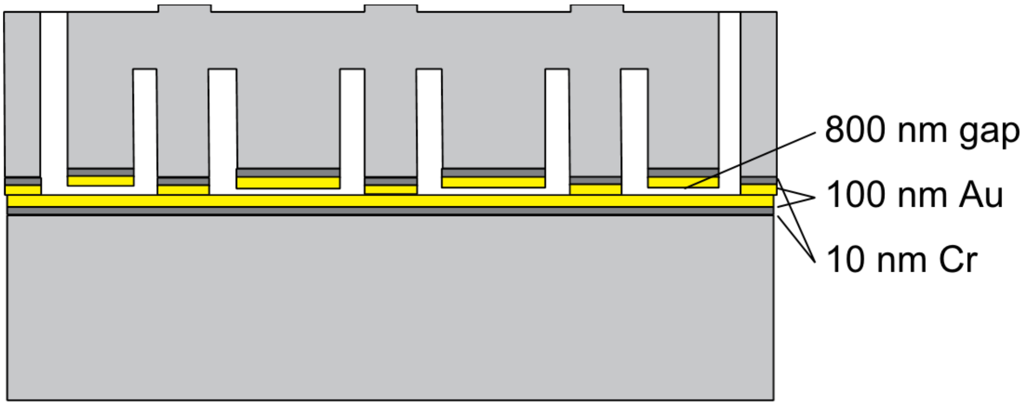

Figure 5.4: Cross-section of the wafers bonded in the bond strength experiments.

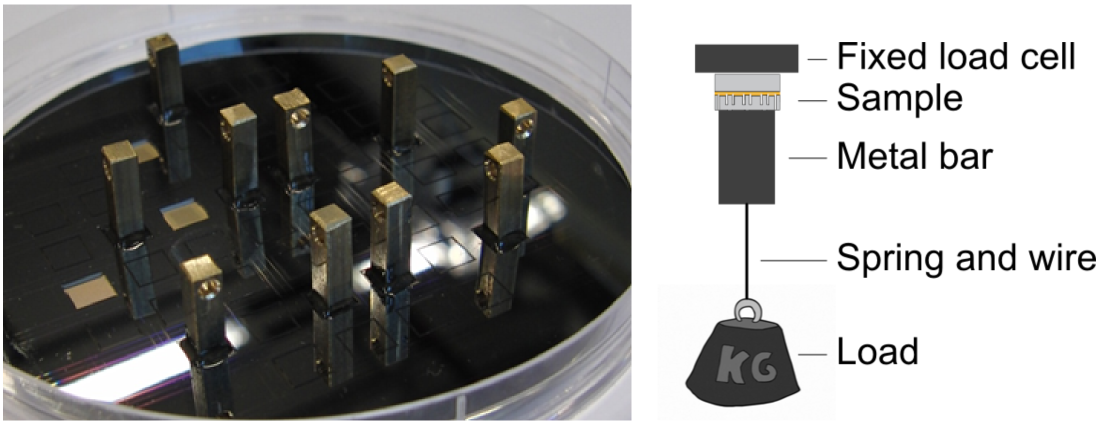

(a)

(b)

Figure 5.5: Measurement setup to find the bond strength: (a) Metal bars are glued to the top wafer of the samples; (b) The bottom wafer is fixed to a load cell, after which a load is attached to the metal bars.

5.2.3 Results

The measurements show a great variation in the bond strength. Also, most of the measured bond strengths are significantly higher than the expected strength of 25 MPa [35]. SEM images of the bond interface of the bottom and top wafer of a sample are given in Figure 5.7. Typically, the fracture occurs in the pillars, just above the bonding interface, as is shown in Figure 5.8. However, some samples reveal another, unexpected, characteristic. As shown in Figure 5.9, when the bonded pillars are pulled from the bottom wafer, they pull out a portion of the bulk Si, which fractures over the <111> crystal orientation.

5.2.4 Discussion

The results raise some questions. First, why does the fracture occur in the bulk as opposed to in the pillar? It would be expected that, given that the bond strength is at least as high as the Si fracture strength, the maximum stress would occur in the pillar as it is much smaller than the bulk structure. Second, when portions of the bulk are pulled from the bottom wafer, why does the fracture run across the <111> crystal orientation?

An answer to the first question may be given using finite element modeling (FEM). Figure 5.10 shows a model of the pillar being pulled from the bulk. As can be seen, the highest stress concentrations occur in the pillar, just above the bond, which corresponds to the fractures found

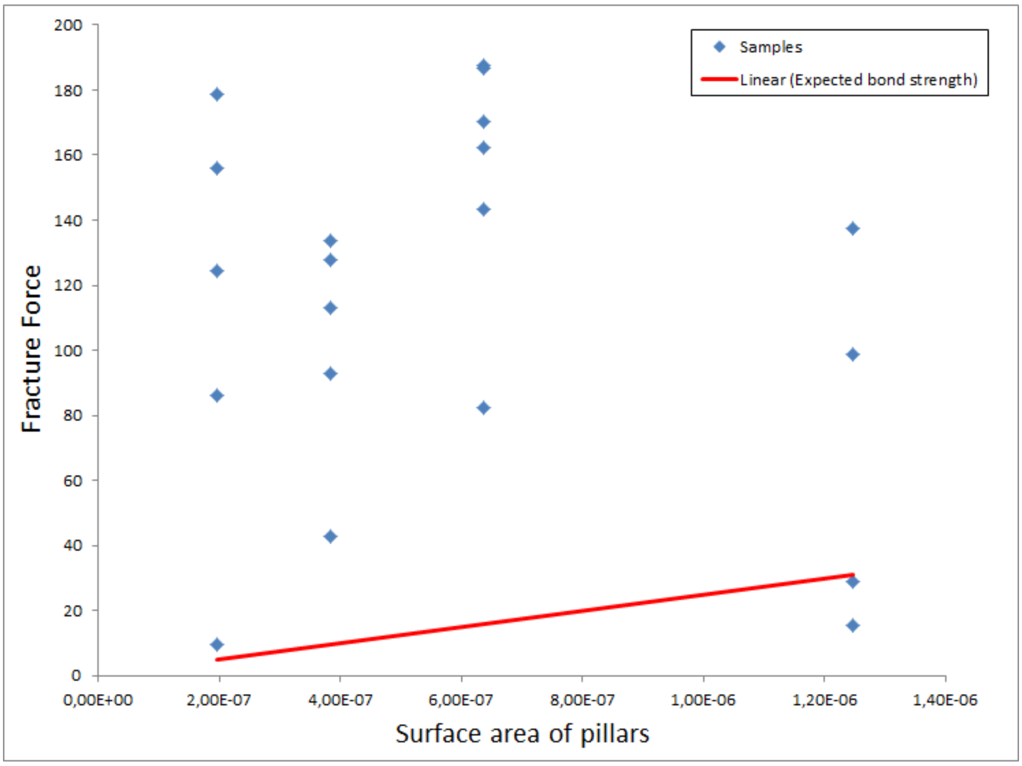

Figure 5.6: Results of the pull tests. Various values for the bond strength are found and however scattered, most values exceed the expected bond strength.

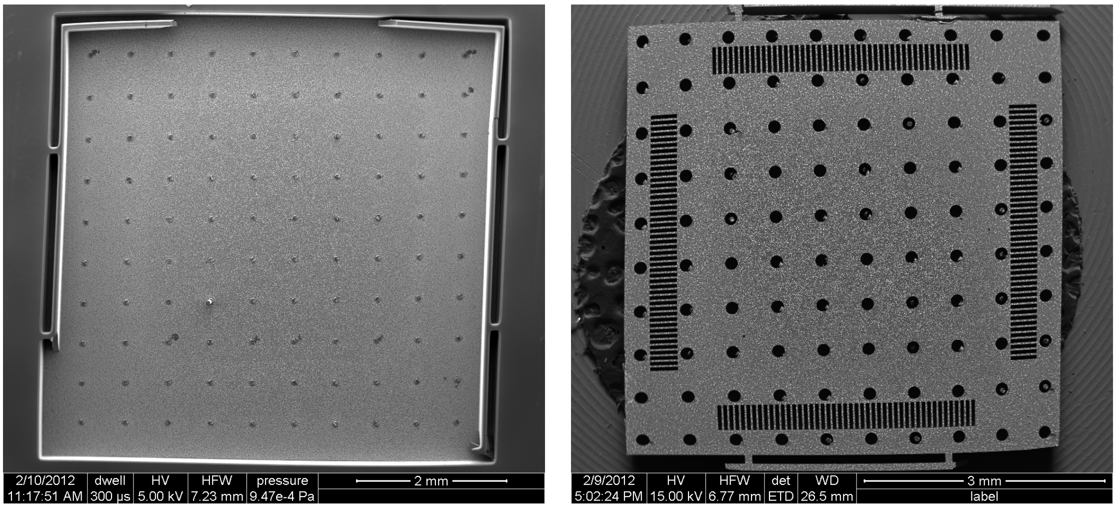

(a) (b)

Figure 5.7: SEM image after the bond has been broken: (a) Bottom wafer; (b) Top wafer.

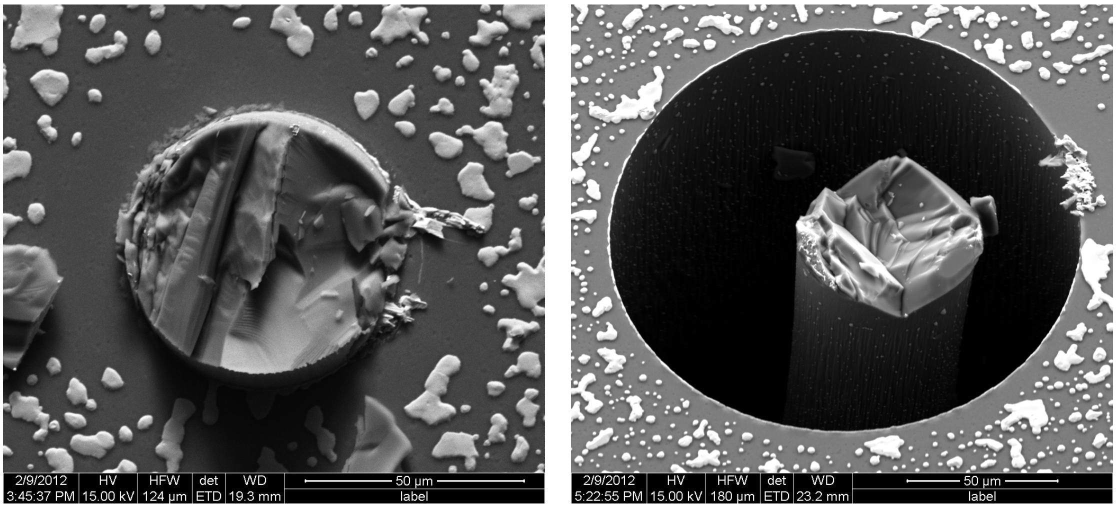

(a) (b)

Figure 5.8: Close up of the broken pillars on the (a) bottom wafer and (b) top wafer. Most fractures appeared in the pillar just above the bonding interface. Note also the various droplets of the eutectic alloy.

in Figure 5.8. But from Figure 5.10b it also becomes clear that a stress concentrations build up in the bulk, just below the bottom corners of the pillars. The stress in these concentrations however, is lower than in the pillar, suggesting that a fracture would only run through the bulk if the fracture strength of the bulk is somehow compromised in comparison with the pillar.

To answer the second question, why the fracture follows the crystal orientation, several options are formulated. It might be due to the difference in energy for the various planes of the crystal orientation. As different planes have different packing densities, the energy needed to release an atom from the various planes differs. The fracture may follow the <111> plane simply because this requires the least energy. Another option is that the portion of the bulk that is released from the bottom wafer, is in fact not bulk Si but the eutectic alloy. Formation of the eutectic melt is known to follow the crystal orientation [38]. If enough eutectic alloy is created to fill the entire volume of the inverted pyramid under the pillar, it is not bulk Si that is fractured, but the fracture runs along the bulk Si/eutectic alloy interface.

To see if the inverted pyramid would constitute normal breaking behaviour for the Si bulk, the bond strength experiment is repeated with wafers that are fusion bonded. SEM images are taken after the bond is forcefully broken (Figure 5.11). As can be seen from Figure 5.11a, portions are pulled from the bottom wafer on various places, however, Figure 5.11b shows the fracture does not run along the Si crystal orientation. This indicates that, since bulk Si is not inclined to fracture along the crystal orientation, the properties of bulk material of the bottom wafer in eutectic bonding are altered.

The aforementioned experiments are conducted to find the eutectic bond strength. The pull testing gives no clear answer, as the measurement provides very scattered results. Eutectic bonding however, does enable very strong bonds, as almost all samples show bond strengths above the expected value. SEM images show particular characteristics of the bond fracture, as it runs along the crystal <111> plane. Comparison with another bonding technique show that this is not to be considered normal bulk Si fracture behaviour. Therefore, this shows that the Si bulk is altered during eutectic bonding.

A possibility as to how the bulk may have been altered is the diffusion of Au atoms into the Si matrix. As the eutectic reaction is preceded by a diffusion, the doping of the bulk with Au could lead to the formation of residual stress after bonding. This would impair the fracture strength of the Si bulk and explain why the fracture runs through the bulk instead of the pillar, but not

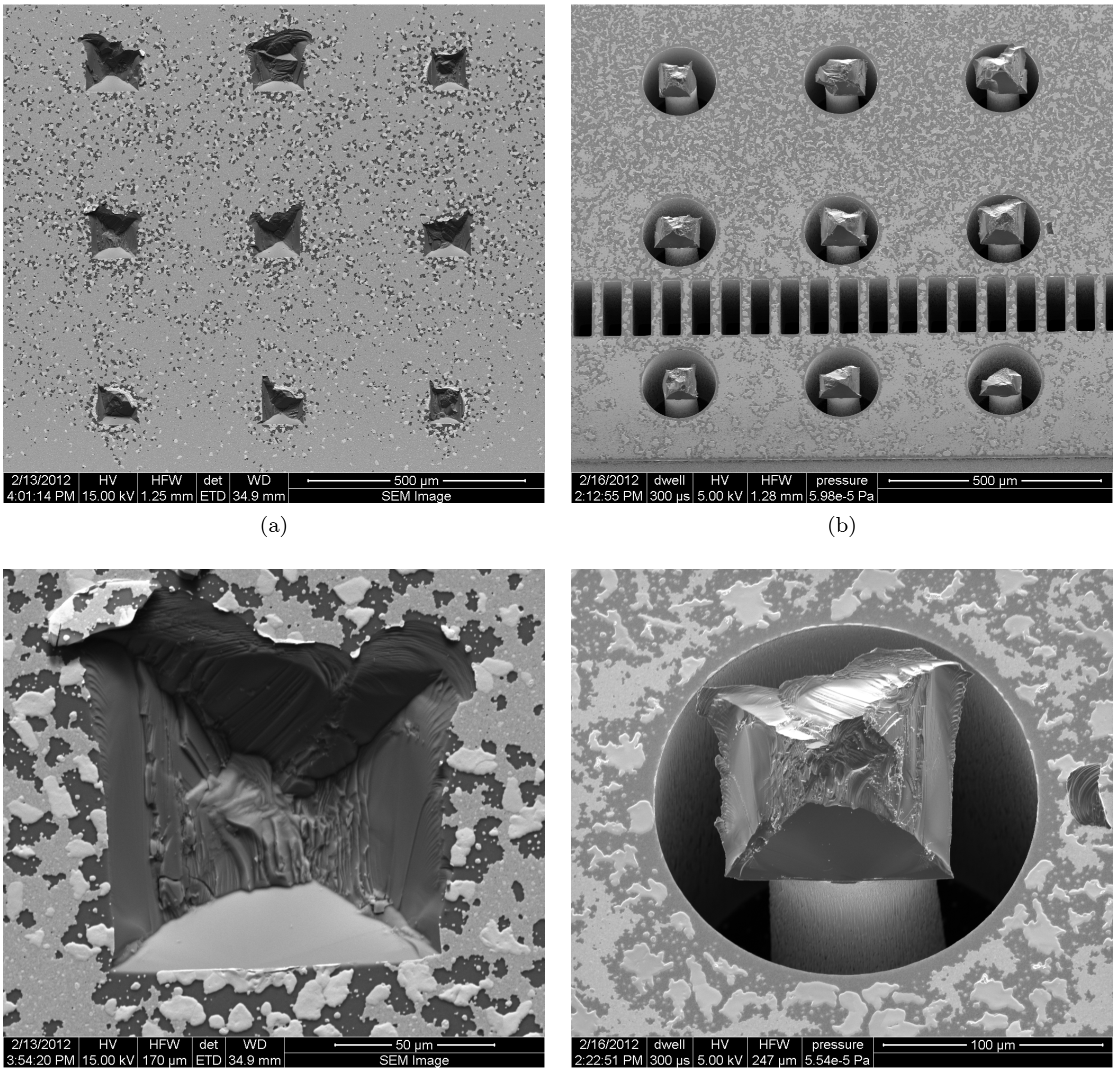

(a) (b)

(c) (d)

Figure 5.9: Portions of the bulk are pulled from the bottom wafer. The fracture runs along the crystal orientation, and the craters take the form of inverted pyramids. (a) Overview of the inverted pyramids in the bottom wafer; (b) Portions of the bulk attached to the pillars on the top wafer; (c) Close-up of an inverted pyramid; (d) Close-up of the pyramid attached to the pillar.

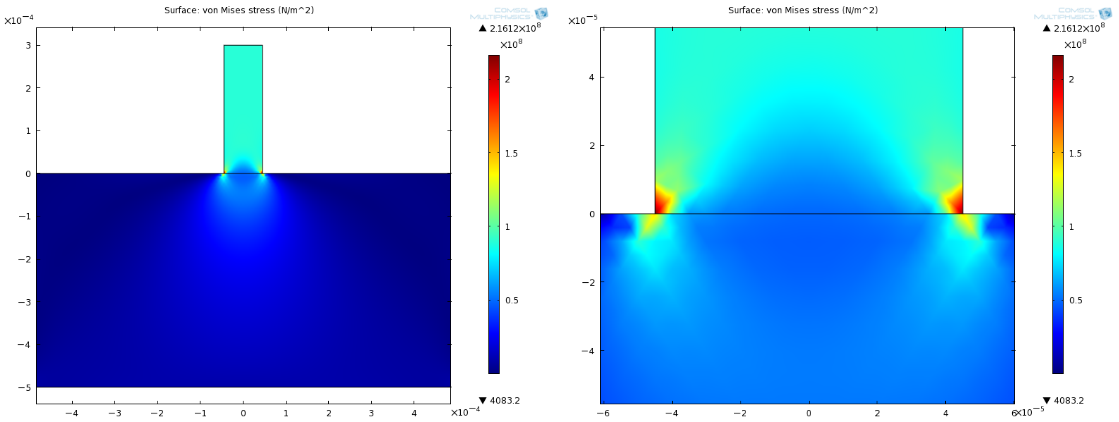

(a) (b)

Figure 5.10: Finite element model of the stress in the pillar and bottom wafer when the pillar is pulled: (a) Overview of the pillar on the wafer; (b) Close-up of the stress concentrations in the pillar and the Si bulk.

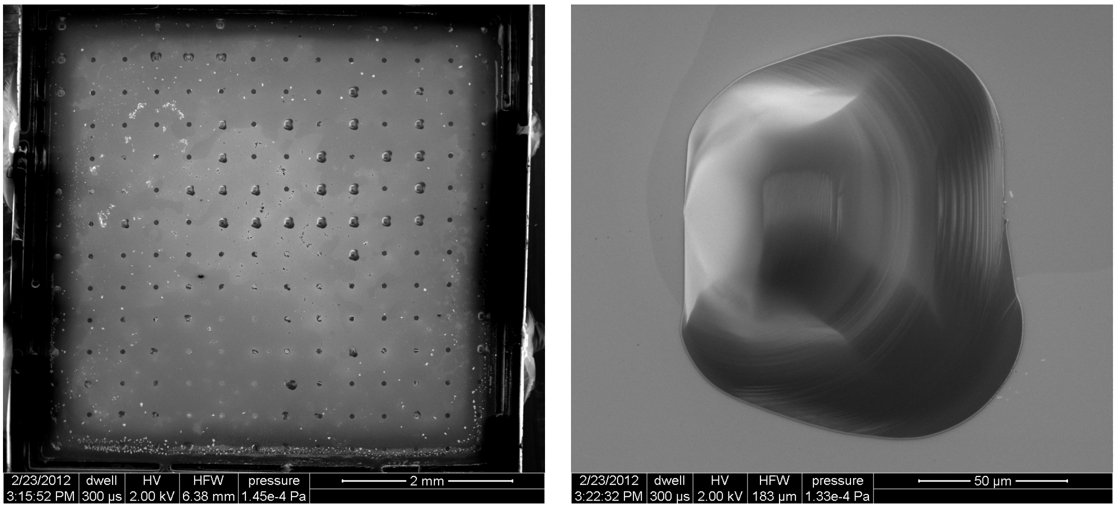

(a) (b)

Figure 5.11: SEM image of a broken sample after it is bonded using fusion bonding. (a) Overview of the sample, showing that portions of the bulk have been pulled out on various places; (b) Close-up of a crater in the bottom wafer, showing no preference for any crystal orientation.

necessarily why the fracture follows the crystal planes. The formation of the eutectic alloy is known to follow the crystal orientations of the Si, but the size of the inverted pyramid is much larger than the volume that can be formed by the eutectic alloy. Therefore, at this moment no clear explanation can be given for the inverted pyramids found on the fracture interface.

5.3 Surface reaction experiment

To get a better understanding of the reactions occurring on the Au-Si interface and the influence of the intermediate Cr or Ti layer, an experiment is conducted in which the thickness of the adhesion layer is varied. The wafers are then broken into quarters and subjected to high temperature annealing for increasing time periods. After the surface has reacted, the deposited layers are etched from the wafers to enable close inspection of the reaction surface on the Si.

5.3.1 Experiment

Six one side polished <100> Si wafers are deposited with adhesive layers of Ti or Cr, in thicknesses of 10, 10 or 100 nm. On top of the adhesive layer, a 100 nm thick Au layer is deposited. One wafer is deposited with just the 100 nm Au as a reference. The wafers are then broken in quarters. The quarters are annealed in a furnace oven at 400 °C under nitrogen ambient. The first quarter is annealed for 15 min. The second quarter is annealed for 30 min. The third quarter is annealed for 170 min. The fourth quarter is not annealed in the oven, indicated as 0 min., to function as a reference. Each quarter is then again broken, in two parts. One part of each quarter of each wafer is then wet etched in Aqua Regia to remove all the deposited metal layers. Table 5.2 shows the wafer configuration and processing conditions. The process flow for this experiment is given in Appendix C.1.

5.3.2 Results

After the wafers are annealed for the various time periods, the surfaces of the quarters are visually compared. Parts from each quarter are then etched and the Si surface is investigated under an optical microscope. Results from both inspections are discussed.

Observations after annealing

Photographic images of the four quarters of the various wafers after annealing are given in Appendix D.1. Several notable characteristics are found. Figure D.1 shows the first wafer, with 100 nm Au. On all annealed quarters, a pattern is formed in the shape of numerous darker crosses on a lighter surface. The lighter parts of the pattern are still darker than the as-deposited Au layer on the fourth quarter. The crosses seem to be oriented crystallographic and appear directed in the <110> direction. All three annealed parts exhibit the crossed pattern and no notable difference is observed between the first quarter annealed for 15 min. and the second quarter that has been in the oven for 30 min. The third quarter that is annealed for 170 min. differs slightly, as the pattern seems a little faded. The difference between the lighter and darker parts of the pattern is less distinct and the edges of the pattern seem more ragged. Also, the third quarter shows areas around the corners where the surface appears more mat and gray.

The second wafer, with a 10 nm Ti adhesive layer, is shown in Figure D.2. Remarkably, there seems to be no significant difference between all four quarters. The quarters annealed for several periods at high temperature all have metal surfaces that appear as-deposited. Wafer three, with 50 nm Ti deposited, is shown in Figure D.3. The annealed quarters present a mat surface, with a color comparable to the deposited Au layer. On quarter one, the mat surface appears uniform, with an occasional darker spot. On quarters two and three, several darker strikes are observed. However, the surfaces on all three quarters are comparable. Figure D.4 shows the fourth wafer, with a 100 nm Ti intermediate layer. Again, quarters two and three exhibit a mat surface, but this time a distinct change of color is observed. The annealed quarters all present a orange color,

	Layer stack	Processing temperature	Processing time
1	Bulk Si 100 nm Au	400 °C	0, 15, 30, 170 min.
2	Bulk Si 10 nm Ti 100 nm Au	400 °C	0, 15, 30, 170 min.
3	Bulk Si 50 nm Ti 100 nm Au	400 °C	0, 15, 30, 170 min.
4	Bulk Si 100 nm Ti 100 nm Au	400 °C	0, 15, 30, 170 min.
5	Bulk Si 10 nm Cr 100 nm Au	400 °C	0, 15, 30, 170 min.
6	Bulk Si 50 nm Cr 100 nm Au	400 °C	0, 15, 30, 170 min.
7	Bulk Si 100 nm Cr 100 nm Au	400 °C	0, 15, 30, 170 min.

Table 5.2: Overview of the different layers deposited on the seven wafers. Each wafer is subsequently broken in quarters which are annealed at high temperature for various time periods.

darker than the color of the deposited Au layer. The first quarter shows the same dark orange as quarters two and three, but its surface is not as mat. Several small spots are found on the first quarter, where the surface has become mat, as well as the areas around the corners, where the onset of the mat surface is found.

The fifth wafer is shown in Figure D.5, with 10 nm Cr under the 100 nm Au layer. This wafer also shows a pattern of light and darker crosses, which resembles wafer 1, with only 100 nm Au. But now it seems, lighter crosses are found on a darker surface. However, the sizes of the colored fields show greater dispersion and the orientation of the coloration appears more random. The first and second quarter show no significant difference, but the third quarter does differ, as it shows more dark areas with only a few small lighter crosses. Figure D.6 shows the sixth wafer, with 50 nm deposited Cr. The temperature annealing here created a mat surface, composed of numerous circular spots. The first quarters shows the initiation of the mat spots on the surface, starting from the corner and not yet filling the entire surface. On the second quarter, the surface is completely mat, although the numerous spots can still be observed. Quarter three shows a more uniform surface, where all the spots have created an even mat surface. The mat surface shows no distinct change of color. The seventh wafer, with 100 nm Cr deposited, is shown in Figure D.7. Again, circular mat spots are observed on the surface, that increase in density with increasing annealing time. However, the size of the spots is smaller and the density of spots is less compared to wafer six, as most of the surface of the first quarter is unaffected and parts of surface of the second quarter still show the shiny as-deposited Au layer. On the third quarter, the whole surface has reacted. However, the surface is not uniform and the circular spots are clearly visible.

Observations after etching

Microscopic images of the wafer parts after etching with Aqua Regia are given in D.2. The images show the various ways in which reactions have taken place between the Si substrate and the deposited metal layers. During deposition of the metal layers, no surface reaction takes place. Therefore, no images are given for the parts that are not annealed at high temperature. For each sample, three images are given with different magnifications. For each figure, image (a) shows a magnification of 10.000 times, (b) has a magnification of 50.000 times and (c) is magnified 100.000 times.

Figure D.8 shows the Si surface of wafer one that is annealed for 15 min. Figure D.9 shows the etched surface after 30 min. of annealing, while Figure D.10 shows the Si on which the 100 nm Au is annealed for 170 min. From the images at a magnification of 10.000, it becomes clear that a non-uniform surface is created during the annealing. Several darker areas can be observed over the sample, with some spots showing multiple coloration. The areas have sizes up to several tens of μm. However, the surface between the areas shows many dark spots, with sizes of several μm. These small spots show to be voids in the silicon substrate, while the bigger areas seem to be of different material than the Si and exhibit striped patterns. Several bigger voids show a form of crystalline orientation along some of the edges, although not all and most of the spots seem to have not distinct orientation. No clear difference is observed between the samples annealed for different time periods.

The samples of wafer two are shown next, with Figure D.11 the part that is annealed for 15 min., Figure D.12 the part that is annealed for 30 min. and Figure D.13 the part that is annealed 170 min. Several voids are found on the Si surface, with sizes ranging from one to ten μm. The voids are uniformly distributed. No crystalline preference is observed, as all spots show rounded edges and random shapes. There seems to be no significant difference between the samples annealed for various times, either in density, size or distribution of the voids.

The Si surfaces of wafer three are given in Figure D.14, which shows the surface after 15 min. annealing, Figure D.15, which shows the surfaces that are annealed for 30 min. and Figure D.16, in which the samples are annealed for 170 min. The surfaces show great irregularities, with areas that show crystal-like growth in size of several hundreds of μm. Closer inspection shows the surface is severely affected by the temperature annealing. Many voids with sizes in the order of μm have created numerous valleys and craters. The surfaces annealed for 15 and 30 min. show similar images, with the exception that on the latter the voids appear to have a somewhat crystalline orientation. The surface annealed for 170 min. shows a distinctive increase in the large crystal-like patterns. They seem to be of a different material, grown on the surface and appear to be much less affected by the etching with Aqua Regia.

Figure D.17 shows the surface of wafer four, annealed for 15 min. Figure D.18 shows the surface after 30 min. and Figure D.19 shows the etched surface after 170 min. annealing. The surfaces show the creation of circular structures in the Si, that increase in size with increasing annealing time. The circular structures consist of many voids and valleys in the affected Si surface, with sizes in the order of several μm. The density of the voids within the circular region does not seem to change with increasing time, rather the area of the region expands, eventually covering the whole surface. Concentric rings are observed in the circular regions of voids.

The pattern that in found on top of the metal layers of wafer five, is also observed on the Si substrate. Figure D.20 shows the sample that is annealed for 15 min., Figure D.21 shows the sample that is annealed for 30 min. and Figure D.22 shows the sample that is annealed for 170 min. The surfaces show a uniform distribution of voids with sizes of several μm. The aforementioned pattern is not caused by the voids. It seems the substrate itself exhibits coloration. The voids appear to have some crystalline orientation preference, comparable to that of wafer one. Between the sample annealed for different time periods, no clear distinction is observed.

Figure D.23 shows the surface of wafer six, that is annealed for 15 min. Figure D.24 shows the surface that is annealed for 30 min. and Figure D.25 shows the surface of the sample that is annealed for 170 min. On the surface annealed for 15 min., circular areas are observed, that consist of voids in the Si substrate, with size ranging from 1 to 10 μm. The voids show rounded corners and no clear crystalline orientation. On the samples that are annealed for 30 and 170 min., the voids fill the surface of the wafer. The density of the voids however, remains the same. The voids now clearly show crystalline orientation, as they have rectangular shapes. In the voids, material other than Si is found, that seems to be unaffected by the wet etching. On the sample that is annealed for 170 min., another pattern emerges. Besides the distinct voids, other areas are found that show a darker color compared to the substrate. The darker areas do not appear to have a different height than the substrate.

Lastly, the surfaces of wafer seven are given. Figure D.26 shows the etched Si surface after annealing for 15 min., Figure D.27 shows the etched surface after annealing for 30 min. and Figure D.28 shows the etched surface after the sample is annealed for 170 min. All surfaces show non-uniform patterns. The patterns consist of round regions where the substrate is affected and voids are found. On the sample that is annealed for 15 min., the edges of the regions consist of rounded voids in the Si. Within the region, other structures are found, with multiple connecting valleys. In the valleys, material is found other than the Si. When the sample is annealed for 30 min., several smaller spots are found between the bigger regions. These spots consist of voids filled with the unknown material. The void exhibit a clear crystalline orientation. The surface of the sample annealed for 170 min. also shows the smaller spots between bigger regions. The voids still seem to be filled with another material but they show not clear crystalline preference.

5.3.3 Discussion

The results show that on all wafers, surface reaction have taken place during the high temperature annealing. On the Si surface of all wafers voids are found, indicating a reaction has occurred between the Si and a metal. Not all surfaces look the same and surface reactions have even taken place with an intermediate layer of 100 nm, which suggests that the Au is not the only metal that reacts with the Si and forms the voids. Ti and Cr are known to react with Si to form compound silicides. This would also give an explanation to the unknown material found in some of the voids, as the compound would not be affected by metal etchant. The fact that the Ti and Cr also react with the Si makes it hard to distinguish whether the Si has also reacted with the Au. As the intermediate layer becomes thicker, it seems more unlikely that the Si and Au have come in contact, but the results presented here cannot prove nor deny this has happened. Therefore, from these images it does not become clear which configuration provides the strongest bond. All samples show reaction occurred with the Si substrate, but if this reaction is not providing in the Au-Si eutectic alloy, a strong bond may not be achieved.

Images also show that the metals itself react under high temperature annealing, as the metal surfaces change significantly. Only the metal surface of wafer two, with 10 nm Ti, shows no change from annealing. The results may be explained by a reaction between the Ti or Cr and the Au. Proposed is that the 10 nm Ti reacts with only a little portion of the 100 nm Au. The reaction product creates a diffusion barrier, effectively blocking the rest of the Au to react or diffuse into the Si. When a thicker layer of Ti is deposited, more Au is needed in the reaction. So much so, that the reaction becomes visible on top of the metal surface. Even more Ti results in even more of the reaction showing, hence the increasingly darker color found between wafer three and four. A reaction between the Au and Cr would also explain the results found for wafers five, six and seven. A thin layer of Cr exhibits a somewhat porous characteristic, unlike Ti. Therefore, 10 nm Cr would not provide a effective layer between the Si and Au and this would explain why wafer five shows a pattern very much like wafer one. A thicker layer of Cr would seal of the Si, hence the results are explained by a reaction between the two deposited metals. The difference between the last two wafers is then due to the different ratios of the Cr and Au.

This shows that while Ti and Cr are usually used as an adhesive layer between the Si and Au, they also contribute themselves to several reactions, with both the Si and the Au. Their influence should therefore not be neglected when designing a device, setting up a fabrication method or wanting to explain the mechanics of eutectic bonding. From the results of experiment 3, no clear candidate is found for the strongest bond, as multiple reactions can be the cause of the voids found on the Si substrate.

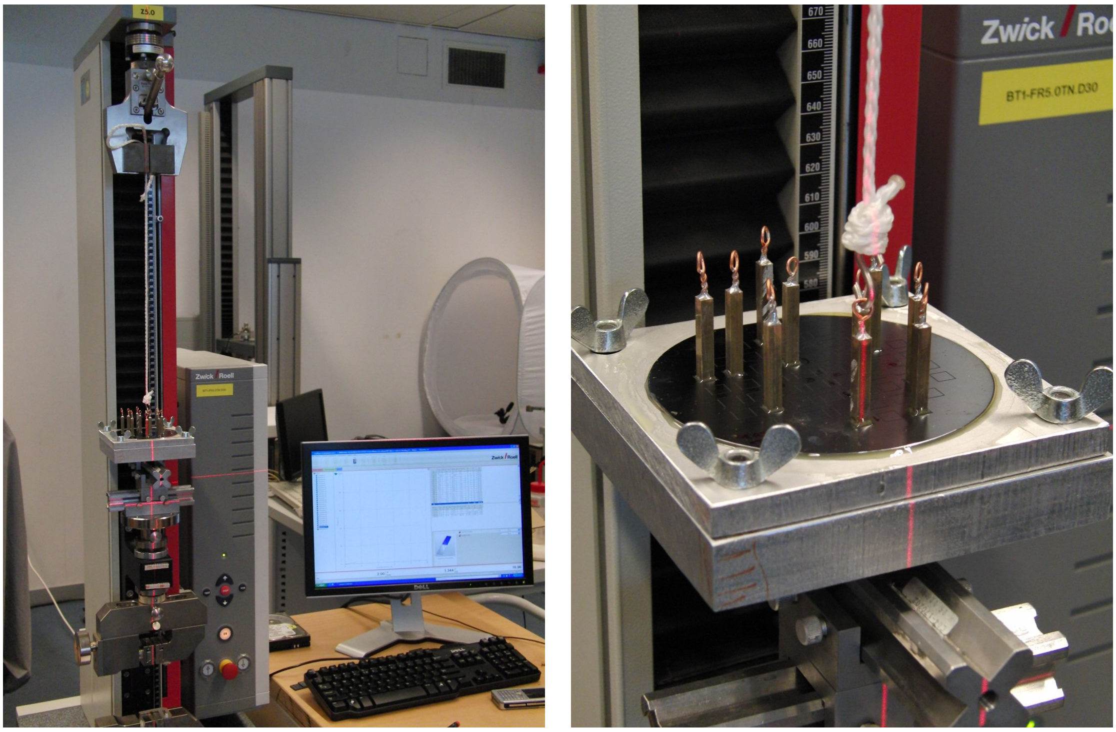

(a) (b)

Figure 5.12: Pull bench measurment setup. (a) A string is attached to the samples to pull them from the bottom wafer; (b) The bottom wafer is glued on a aluminum block which is fixed to the moving arm.

5.4 Advanced bond strength experiment

For each of the seven wafer configurations created in experiment 3, the bond strength is investigated using pull-testing. This time, an automated pull-bench is used, to measure the force needed to release a sample from the bond and make sure the process conditions and direction of the force are the same for each sample.

5.4.1 Experiment

Standard Si <100> wafers are deposited with the different layer stacks as described in experiment 3. The metal layers are deposited on both the bottom and the top wafer of each bonding pair. The top wafer is patterned using DRIE etching to create several square samples with the pillars that will be bonded. Several different samples are created, with a different number and radius of the pillars. The two wafers are bonded together in a vacuum bonder at a temperature of 375 °C for a time period of 15 min. After annealing, the bonded wafer are examined in the pull-bench, where individual samples are forcefully releases from the bond. The process flow for this experiment is given in Appendix C.2.

5.4.2 Measurement setup

The bonding strength is measured using an automated pull-bench (Zwick, Model Z1.0/THIS). With this setup, the wafers are attached to a moving arm. A fixed load-cell is attached to the samples. The arm with the wafers then gradually moves away from the load-cell, increasing the force on the bond that is continuously measured. Metal bars are glued on the samples of the top wafer and attached to the load-cell via a string. The bottom wafer is glued to an aluminum block which is used to fixate the sample in the pull-bench. Figure 5.12 shows the measurement setup.

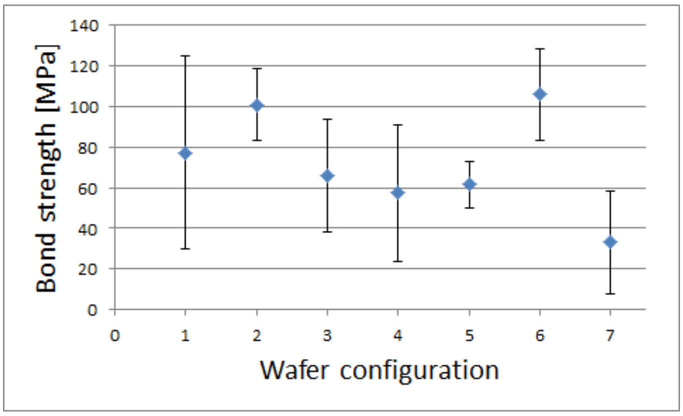

Figure 5.13: Mean bond strength values for each wafer configuration. Also given are the standard deviations from the mean value.

Wafer	Mean fracture strength [MPa]	Standard deviation	Fractured
1. 100 nm Au	77,4	47,3	Si bulk
2. 10 nm Ti, 100 nm Au	101	17,8	Si bulk
3. 50 nm Ti, 100 nm Au	65,9	27,6	Si bulk
4. 100 nm Ti, 100 nm Au	57,4	33,7	Bond interface
5. 10 nm Cr, 100 nm Au	61,5	11,2	Si bulk
6. 50 nm Cr, 100 nm Au	106	22,5	Si bulk
7. 100 nm Cr, 100 nm Au	33,1	25,1	Bond interface

Table 5.3: Mean bond strength and standard deviation of samples pulled from each wafer configuration.

5.4.3 Results

The obtained data from the pull-bench testing is given in Appendix E. The mean fracture strength for each wafer is shown in Figure 5.13 and given in table 5.3 with also the standard deviation from the mean value. It becomes clear that the acquired bond strength shows great variation for the different wafer configurations. Also between samples on the same wafer, variation in bond strength is quite large, as given by the standard deviation. The strongest bonds are found on wafer two and six, which are the wafers with 10 nm Ti and 50 nm Cr. Wafer seven, with 100 nm Cr, shows the weakest bonds. While the mean bond strength for wafer one with only 100 nm Au is quite strong, the spreading in the measured values is remarkably large. Images of the fractured bond interface are given for several samples in Appendix F.

5.4.4 Discussion

The pull-bench measurements provided widespread values for the bond strength, remarkably also for the various samples on each wafer. The images of the fractured bond interface show a gradient in the fracture pattern. A misalignment of the mounts used to pull the samples might be a cause of this, but it also suggests that the reactions forming the bond do not occur uniformly. The spread in values is the biggest for wafer one, on which a sole layer of 100 nm Au is deposited. This suggests that the bonding between Au and bare Si is most prone to factors influencing the bond. In the literature presented in chapter 4, similar findings are described, in which the Si surface is easily compromised by the forming of a native oxide. Therefore, a thin adhesive layer of Ti or Cr is used to break the oxide [37]. The results for wafer two and five, with 10 nm Ti and Cr, acknowledge this theory, as the standard deviation is the smallest for these wafers, showing the bonding has occurred more uniform. Images from experiment 3 also show a uniform distribution of the voids in the Si surface for wafers two and five.

Wafer three and four show a decline in bond strength as the thickness of the intermediate Ti layer increases. Qualitatively, this would be expected, as a thicker Ti layer would prevent the Au from coming into contact with the Si and forming the eutectic bond. However, a sufficiently thick layer would seal of the Si substrate, preventing any eutectic reaction from taking place and result in a very uniform, weak, bond. The fact that the spreading in the bond strength increases from wafer three to four and that the mean bond strength is still close to the bond strength found on wafers one and five, suggests bonding reactions do occur, even for thick layers of Ti. Results from experiment 3 also confirm this, as the Si surface of wafers three and four, while non-uniform, is severely affected. The Ti seems not to shield the Si from reacting but actively contributes to a reaction.

The same may not necessarily be true for wafers six and seven, with 50 and 100 nm Cr. Wafer seven overall shows a weak bond and there is a significant spreading the bond strength values. Wafer six however shows an unexpected high value for the mean bond strength. Images from experiment 3 show that wafers six and seven have great non-uniformity on the also severely affected Si substrate. This would explain the spreading in the measurement results, but not the high mean strength of wafer six. Since the non-uniformity would reduce the overall bonded area, a lower bond strength would be expected. It seems the 50 nm Cr layer actively contributes to a stronger bond. Why this contribution predominantly manifests itself when the Cr has a thickness of 50 nm is a topic for further investigation.

5.5 Conclusions

The experiments presented in this chapter are conducted to find the maximum eutectic bond strength and the process parameters influencing this value. The first experiment shows that a bonding time of 15 min. is sufficient to create a strong bond. Processing for 30 min. can even be considered as too long. It also showed that addition of an intermediate adhesive metal layer improves the bond. The second experiment suggests that the achieved eutectic bond is at least as strong as the bulk strength of the Si, as fractures occurred in the pillars, and sometimes the bulk substrate, but not on the bond interface. The influence of the adhesive metal layers can not be neglected in the complete description of the reactions occurring during bonding, as experiment three shows. While thin layers intermediate layers do increase the uniformity of the surface reactions, their influence is not restricted to the decomposition of the native oxide layer on the Si substrate. The results from experiment three and four show that when the thickness of the adhesive layers is increased, the Ti and Cr actively react themselves with the Si and Au. Unknown material is observed on the wafers which is likely a compound silicide formed between the Ti or Cr and Au. Which reactions occur and what materials are created is subject to further investigation. The bond strength measurements could not provide in a definitive value for each wafer configuration. The spreading between the samples on the same wafer is found to be quite large. Therefore, no clear distinctions can be observed between every wafer configuration. The results do indicate that the addition of a thin intermediate layer improves bonding uniformity, but adding too much Ti or Cr degrades the bond as competing reactions occur.

Chapter 6

Conclusions and recommendations

This chapter presents the conclusions from the development of the force sensor, the investigation into eutectic bonding and the experiments conducted to find optimal processing parameters and wafer configurations.

6.1 Sensor design

A design is presented of a six-component force and moment sensor, capable of measuring up to 50 N of normal force and 10 N of shear force. The design features mechanical load reduction, by using a double-wafer design that is bonded via load-bearing pillars. This effectively translates the applied forces into displacements that can subsequently be measured by the sensing structures in the bottom wafer. Dimensions and geometry of these sensing structures are determined by creating a equivalent spring constant model. With this model the structures are designed to approach the maximum allowable stress to provide the best sensitivity. The proposed strain gauges consist of a deposited Au metal layer. Optimization of the strain gauges dimensions is presented. Analytical analysis shows that the initial resistance of 12 Ω of the strain gauges changes up to 2,4 ‰ (29 mΩ) under maximum load. Options are given for wiring and readout, as the sensors can be used as single cells or can be connected in series to increase the signal that can be measured. Temperature influences can be compensated using Wheatstone configurations, as multiple strain gauges can be used as the different legs of a Wheatstone bridge. A CleWin photo-lithography mask is created for the sensing structures, the strain gauges and the electrical on-chip wiring. The design incorporates wafer-to-wafer bonding, whereby significant forces are exerted on the established bond. The dimensions of the structures in this design are also dependent on the achieved bond strength. If in the future, the bond strength shows to be significantly lower than assumed, the design may need re-dimensioning to provide in larger bond areas. At the moment, no such need exists.

6.2 Eutectic bonding

The experiments performed to establish fabrication process parameters and wafer configuration provided several insights. A processing time of 15 min. is found to be sufficient to create a strong bond in the initial experiment, annealing longer may even degrade the quality of the eutectic bond. A thin adhesive layer of Ti or Cr, deposited between the Si and Au, is found to improve the bond strength. Pull testing of bonded samples shows fractures occurring in the Si, suggesting the achieved bond strength is higher then the fracture strength of the Si bulk. The addition of Ti or Cr is shown to influence the bonding reactions, as experiments show that additional reactions take place on the Si surface and also between the Ti or Cr and Au. Pull testing on samples with varying thicknesses of the intermediate metal layer give no clear indication of an optimum to establish the strongest bond. The significant spreading in the measured bond strength values might indicate that the bonding is not uniform over the wafer, although it could also be caused by a misalignment during the pull-testing.

6.3 Future work

The design of the sensor features Au strain gauges. This limits the options on processing after the deposition of the Au. At this moment, the strain gauges and the Au for the eutectic bonding can be deposited in one processing step. However, if future research shows that Au is not the preferred metal of eutectic bonding is not the preferred method of bonding, the sensing structures of the sensor can be created using poly-Si as a piezoresistive material. This would enable other processing options, such as higher temperature bonding, and might also increase the sensitivity of the sensor.

As the adhesive layers of Ti and Cr are shown to actively take part in the surface reaction and compound materials are found, a better understanding of the reaction between the Ti or Cr with the Si substrate and between the Ti or Cr and the Au is needed. The unknown material found during the experiments could be investigated to find its composition, i.e. by examining with: Transmission Electron Microscopy (TEM), Auger Electron Spectroscopy, Energy Dispersive X-ray spectroscopy (EDX) or X-ray Photo-electron Spectroscopy (XPS).

The processing conditions may also need further investigation, as the experiments showed the bonding does not occur uniformly over the wafer. This variation in achieved bond strength would not be suitable in a fabrication process and the factors causing this non-uniformity should be examined. For the bond strength experiments, the deposited metal layers are not patterned. The bond area is defined by the geometry of the Si pillars. However, to be able to use eutectic bonding in the fabrication of devices, it should be possible to define the area of bonding by defining a pattern in the deposited metal layers. Patterning of the deposited layers on the seven wafer configurations is examined using wet etching. However, this resulted in lift-off of the Au layer, as galvanic corrosion caused severe under-etching of the adhesive metal layers [48]. Therefore, methods should be established to pattern the deposited metal layers without the use of electrochemical wet etching.

Bibliography

[1] P. H. Veltink, H. Kortier, and H. M. Schepers, "Sensing power transfer between the human body and the environment," *IEEE Transactions on Biomedical Engineering*, vol. 56, no. 6, pp. 1711–1718, 2009.

[2] P. H. Veltink, R. J. Wiegerink, and M. Elwenspoek, "Sensing power transfer between the human body and the environment." STW project proposal, 2008.

[3] "Power sensor." website, May 2012. http://uspam.ewi.utwente.nl.

[4] R. A. Brookhuis, T. S. J. Lammerink, R. J. Wiegerink, M. J. De Boer, and M. C. Elwenspoek, "Force sensor for measuring power transfer between the human body and the environment," in *2011 16th International Solid-State Sensors, Actuators and Microsystems Conference, TRANSDUCERS'11*, pp. 2042–2045, 2011.

[5] M. Elwenspoek, G. Krijnen, R. Wiegerink, and T. Lammerink, *Introduction to Mechanics and Transducer Science*. University of Twente, 2009.

[6] A. A. Barlian, W. . Park, J. R. Mallon Jr., A. J. Rastegar, and B. L. Pruitt, "Review: Semiconductor piezoresistance for microsystems," *Proceedings of the IEEE*, vol. 97, no. 3, pp. 513–552, 2009.

[7] B. J. Kane, M. R. Cutkosky, and G. T. A. Kovacs, "Cmos-compatible traction stress sensor for use in high-resolution tactile imaging," *Sensors and Actuators, A: Physical*, vol. 54, no. 1-3, pp. 511–516, 1996.

[8] B. J. Kane, M. R. Cutkosky, and G. T. A. Kovacs, "Traction stress sensor array for use in high-resolution robotic tactile imaging," *Journal of Microelectromechanical Systems*, vol. 9, no. 4, pp. 425–434, 2000.

[9] W. L. Jin and C. D. Mote Jr., "Development and calibration of a sub-millimeter three-component force sensor," *Sensors and Actuators A: Physical*, vol. 65, no. 1, pp. 89–94, 1998.

[10] W. L. Jin and C. D. Mote Jr., "A six-component silicon micro force sensor," *Sensors and Actuators, A: Physical*, vol. 65, no. 2-3, pp. 109–115, 1998.

[11] T. Mei, W. J. Li, Y. Ge, Y. Chen, L. Ni, and M. H. Chan, "Integrated mems three-dimensional tactile sensor with large force range," *Sensors and Actuators, A: Physical*, vol. 80, no. 2, pp. 155–162, 2000.

[12] J. Kim, Y. Park, and D. Kang, *Design and fabrication of a three-component force sensor using micromachining technology*. No. 1685 in VDI Berichte, Deutscher Ingenieur-Verlag, 2002.

[13] K. Kim, K. R. Lee, Y. K. Kim, D. S. Lee, N. K. Cho, W. H. Kim, K. B. Park, H. D. Park, Y. K. Park, J. H. Kim, and J. J. Pak, "3-axes flexible tactile sensor fabricated by si micromachining and packaging technology," in *Proceedings of the IEEE International Conference on Micro Electro Mechanical Systems (MEMS)*, vol. 2006, pp. 678–681, 2006.

[14] L. Wang and D. J. Beebe, “Silicon-based shear force sensor: development and characterization,” *Sensors and Actuators, A: Physical*, vol. 84, no. 1, pp. 33–44, 2000.

[15] L. Wang and D. J. Beebe, “Characterization of a silicon-based shear-force sensor on human subjects,” *IEEE Transactions on Biomedical Engineering*, vol. 49, no. 11, pp. 1340–1347, 2002.

[16] S. Bütefisch, S. Büttgenbach, T. Kleine-Besten, and U. Brand, “Micromechanical three-axial tactile force sensor for micromaterial characterisation,” *Microsystem Technologies*, vol. 7, no. 4, pp. 171–174, 2001.

[17] V. Nesterov and U. Brand, “Modelling and investigation of the silicon twin design 3d micro probe,” *Journal of Micromechanics and Microengineering*, vol. 15, no. 3, pp. 514–520, 2005.

[18] A. Tibrewala, A. Phataralaoha, and S. Büttgenbach, “Simulation, fabrication and characterization of a 3d piezoresistive force sensor,” *Sensors and Actuators, A: Physical*, vol. 147, no. 2, pp. 430–435, 2008.

[19] A. Tibrewala, A. Phataralaoha, and S. Büttgenbach, “Development, fabrication and characterization of a 3d tactile sensor,” *Journal of Micromechanics and Microengineering*, vol. 19, no. 12, 2009.

[20] D. V. Dao, T. Toriyama, J. Wells, and S. Sugiyama, “Six-degree of freedom micro force-moment sensor for application in geophysics,” in *Proceedings of the IEEE Micro Electro Mechanical Systems (MEMS)*, pp. 312–315, 2002.

[21] M. Ádám, E. Vázsonyi, I. Bársony, G. Vésárhelyi, and C. Dücsö, “Three dimensional single crystalline force sensor by porous si micromachining,” in *Proceedings of IEEE Sensors*, vol. 1, pp. 501–504, 2004.

[22] G. Vásárhelyi, M. Ádám, E. Vázsonyi, Z. Vízváry, A. Kis, I. Bársony, and C. Dücsõ, “Characterization of an integrable single-crystalline 3-d tactile sensor,” *IEEE Sensors Journal*, vol. 6, no. 4, pp. 928–934, 2006.

[23] E. Vázsonyi, M. Ádám, C. Dücs, Z. Vízváry, A. L. Tóth, and I. Bársony, “Three-dimensional force sensor by novel alkaline etching technique,” *Sensors and Actuators, A: Physical*, vol. 123-124, pp. 620–626, 2005.

[24] G. Vásárhelyi, M. Ádám, E. Vázsonyi, I. Bársony, and C. Dücso, “Effects of the elastic cover on tactile sensor arrays,” *Sensors and Actuators, A: Physical*, vol. 132, no. 1 SPEC. ISS., pp. 245–251, 2006.

[25] D. Molnár, A. Pongrácz, M. Ádám, Z. Hajnal, V. Timárné, and G. Battistig, “Sensitivity tuning of a 3-axial piezoresistive force sensor,” *Microelectronic Engineering*, 2011. Article in Press.

[26] L. Beccai, S. Roccella, A. Arena, F. Valvo, P. Valdastri, A. Menciassi, M. C. Carrozza, and P. Dario, “Design and fabrication of a hybrid silicon three-axial force sensor for biomechanical applications,” *Sensors and Actuators, A: Physical*, vol. 120, no. 2, pp. 370–382, 2005.

[27] P. Valdastri, S. Roccella, L. Beccai, E. Cattin, A. Menciassi, M. C. Carrozza, and P. Dario, “Characterization of a novel hybrid silicon three-axial force sensor,” *Sensors and Actuators, A: Physical*, vol. 123-124, pp. 249–257, 2005.

[28] A. Sieber, P. Valdastri, K. Houston, A. Menciassi, and P. Dario, “Flip chip microassembly of a silicon triaxial force sensor on flexible substrates,” *Sensors and Actuators, A: Physical*, vol. 142, no. 1, pp. 421–428, 2008.

[29] R. Wiegerink, R. Zwijze, G. Krijnen, T. Lammerink, and M. Elwenspoek, "Quasi-monolithic silicon load cell for loads up to 1000 kg with insensitivity to non-homogeneous load distributions," *Sensors and Actuators, A: Physical*, vol. 80, no. 2, pp. 189–196, 2000.

[30] R. Hibbeler, *Mechanics of Materials.* Pearson Education, 2nd revised ed., 2005.

[31] W. C. Young and R. G. Budynas, *Roark's formulas for Stress and Strain.* McGraw-Hill, 7th revised ed., 2001.

[32] T. Yi, L. Li, and C. J. Kim, "Microscale material testing of single crystalline silicon: Process effects on surface morphology and tensile strength," *Sensors and Actuators, A: Physical*, vol. 83, no. 1, pp. 172–178, 2000.

[33] D. Son, J. . Kim, T. W. Lim, and D. Kwon, "Evaluation of fracture properties of silicon by combining resonance frequency and microtensile methods," *Thin Solid Films*, vol. 468, no. 1-2, pp. 167–173, 2004.

[34] P. . Chang, G. Berman, and C. C. Shen, "Transmission electron microscopy of gold-silicon interactions on the backside of silicon wafers," *Journal of Applied Physics*, vol. 63, no. 5, pp. 1473–1477, 1988.

[35] A. . Tiensuu, M. Bexell, J. . Schweitz, L. Smith, and S. Johnsson, "Assembling three-dimensional microstructures using gold-silicon eutectic bonding," *Sensors and Actuators: A.Physical*, vol. 45, no. 3, pp. 227–236, 1994.

[36] R. F. Wolffenbuttel and K. D. Wise, "Low-temperature silicon wafer-to-wafer bonding using gold at eutectic temperature," *Sensors and Actuators: A.Physical*, vol. 43, no. 1-3, pp. 223–229, 1994.

[37] R. F. Wolffenbuttel, "Low-temperature intermediate au-si wafer bonding; eutectic or silicide bond," *Sensors and Actuators, A: Physical*, vol. 62, no. 1-3, pp. 680–686, 1997.

[38] B. Bokhonov and M. Korchagin, "In situ investigation of stage of the formation of eutectic alloys in si-au and si-al systems," *Journal of Alloys and Compounds*, vol. 312, no. 1-2, pp. 238–250, 2000.

[39] Y. T. Cheng, L. Lin, and K. Najafi, "Localized silicon fusion and eutectic bonding for mems fabrication and packaging," *Journal of Microelectromechanical Systems*, vol. 9, no. 1, pp. 3–8, 2000.

[40] J. . Jang, S. Hayes, J. . Lin, and D. R. Frear, "Interfacial reaction of eutectic ausi solder with si (100) and si (111) surfaces," *Journal of Applied Physics*, vol. 95, no. 11 I, pp. 6077–6081, 2004.

[41] P. H. Chen, C. L. Lin, and C. Y. Liu, "Amorphous si/au wafer bonding," *Applied Physics Letters*, vol. 90, no. 13, 2007.

[42] Y. C. Lin, M. Baum, M. Haubold, J. Frömel, M. Wiemer, T. Gessner, and M. Esashi, "Development and evaluation of au-si eutectic wafer bonding," in *TRANSDUCERS 2009 - 15th International Conference on Solid-State Sensors, Actuators and Microsystems*, pp. 244–247, 2009.

[43] E. Jing, B. Xiong, and Y. Wang, "The bond strength of au/si eutectic bonding studied by ir microscope," *IEEE Transactions on Electronics Packaging Manufacturing*, vol. 33, no. 1, pp. 31–37, 2010.

[44] E. Jing, B. Xiong, and Y. Wang, "The au/si bonding interface studied by infrared microscope," *Materials Letters*, vol. 64, no. 7, pp. 827–829, 2010.

[45] E. Jing, B. Xiong, and Y. Wang, "Low-temperature au/si wafer bonding," *Electronics Letters*, vol. 46, no. 16, pp. 1143–1144, 2010.

[46] E. Jing, B. Xiong, and Y. Wang, "Low-temperature au-si wafer bonding," *Journal of Micromechanics and Microengineering*, vol. 20, no. 9, 2010.

[47] E. Jing, B. Xiong, and Y. Wang, "Low-temperature au/a-si wafer bonding," *Journal of Micromechanics and Microengineering*, vol. 21, no. 1, 2011.

[48] Y. Nemirovsky, I. A. Blech, and J. Yahalom, "Abnormal undercutting in etched cr/au films," *Journal of the Electrochemical Society*, vol. 125, no. 7, pp. 1177–1179, 1978.

Appendix A

Maple model

```
> restart;
# Complete device spring equivalent model
# Constants
# Youngs modulus Silicon
> E := 0.150e12;
> Fx := 10;
> Fz := 50;
# Variables
# Height pillars
> h := 0.300e-3;
# Radius Load bearing pillars
> r[1] := 0.25e-4;
# Number of Load bearing pillars
> n[1] := 100;
# Thickness device layer
> t := 0.25e-4;
# Width cantilever arms
> w := 0.25e-4;
# Length cantilever arms transverse springs
> l[2] := 0.300e-3;
# Number of transverse springs
> n[2] := 60;
# Length cantilever ams cross springs
> l[3] := 0.150e-3;
# Number of crosses
> n[3] := 25;
# Number of arms per side of each cross
> n[c] := 3;
# Radius Cross spring pillars
> r[3] := 0.25e-4;
# Spring constants of seperate parts
# Spring constant Load bearing pillars
> kPx := 3*E*Pi*r[1]^4*n[1]/h^3;
> simplify(kPx);
                       2.045307718 10^6
> kPz := E*Pi*r[1]^2*n[1]/h;
> simplify(kPz);
                       9.817477044 10^7
# Spring constant Transverse springs
> kTxL := 2*E*t*w/l[2];
> kTxT := 2*E*t*w^3/l[2]^3;
> kTx := (1/2)*(kTxL+kTxT)*n[2];
```

```
> simplify(kTx);
                         1.888020834 10^7
> kTz := 4*E*w*t^3/l[2]^3*((1/2)*n[2]);
> simplify(kTz);
                         2.604166666 10^5
# Spring constant Cross springs
> kCx := n[c]*(2*E*t*w^3/l[3]^3+2*E*t*w/l[3])*n[3];
> simplify(kCx);
                         9.635416665 10^7
> kCz := 4*n[c]*E*w*t^3*n[3]/l[3]^3;
> simplify(kCz);
                         5.208333332 10^6
# Spring constant pillars on the Crosses
> kCPx := 3*E*Pi*r[3]^4*n[3]/h^3;
> simplify(kCPx);
                         5.113269295 10^5
> kCPz := E*Pi*r[3]^2*n[3]/h;
> simplify(kCPz);
                         2.454369261 10^7
# Combined spring constants
# Combined spring constant Crosses and pillars
> k3x := 1/(1/kCPx+1/kCx);
> simplify(k3x);
                         5.086277715 10^5
> k3z := 1/(1/kCPz+1/kCz);
> simplify(k3z);
                         4.296572361 10^6
# Total spring constants
> kx := kPx+kTx+k3x;
> simplify(kx);
                         2.143414382 10^7
> kz := kPz+kTz+k3z;
> simplify(kz);
                         1.027317595 10^8
# Displacements
# Total displacement
> x := Fx/kx;
> simplify(x);
                         4.665453438 10^-7
> z := Fz/kz;
> simplify(z);
                         4.867044062 10^-7
# Stresses
# Forces on the Load bearing pillars
> FPx := kPx*x/n[1];
> simplify(FPx);
                         0.009542287924
> FPz := kPz*z/n[1];
> simplify(FPz);
                         0.4778209334
# Stress in the Load bearing pillars
> sigmaPx := 2*FPx*h/(Pi*r[1]^3);
> simplify(sigmaPx);
                         1.166363360 10^8
> sigmaPz := FPz/(Pi*r[1]^2);
> simplify(sigmaPz);
                         2.433522031 10^8
# Forces on the Transversal springs
```

```
> FTxT := kTxT*x;
> simplify(FTxT);
                         0.002024936388
> FTxL := kTxL*x;
> simplify(FTxL);
                         0.2915908399
> FTz := kTz*z/n[2];
> simplify(FTz);
                         0.002112432318
# Stress in the Transversal springs
> sigmaTxT := 3*FTxT*l[2]/(2*t*w^2);
> simplify(sigmaTxT);
                         5.831816798 10^7
> sigmaTxL := FTxL/(2*t*w);
> simplify(sigmaTxL);
                         2.332726719 10^8
> sigmaTz := 3*FTz*l[2]/(4*w*t^2);
> simplify(sigmaTz);
                         3.041902539 10^7
# Forces on the Crosses and pillars
> F3x := k3x*x/n[3];
> simplify(F3x);
                         0.009491916746
> F3z := k3z*z/n[3];
> simplify(F3z);
                         0.08364642800
# Stress in the Crosses and pillars
# Stress in the pillars
> sigma3Px := 2*F3x*h/(Pi*r[3]^3);
> simplify(sigma3Px);
                         1.160206440 10^8
> sigma3Pz := F3z/(Pi*r[3]^2);
> simplify(sigma3Pz);
                         4.260077595 10^7
# Stress in the Cross
> sigma3Cz := 3*F3z*l[3]/(4*n[c]*w*t^2);
> simplify(sigma3Cz);
                         2.007514272 10^8
# Buckling
# Buckling load of the pillars
> P[cr1] := E*Pi^3*r[1]^4/(4*h^2);
> simplify(P[cr1]);
                         5.046594514
> simplify(FPz/P[cr1]);
                         0.09468185565
> P[cr3] := E*Pi^3*r[3]^4/(4*h^2);
> simplify(P[cr3]);
                         5.046594514
> simplify(F3z/P[cr3]);
                         0.01657482640
>
```

Appendix B

CleWin mask

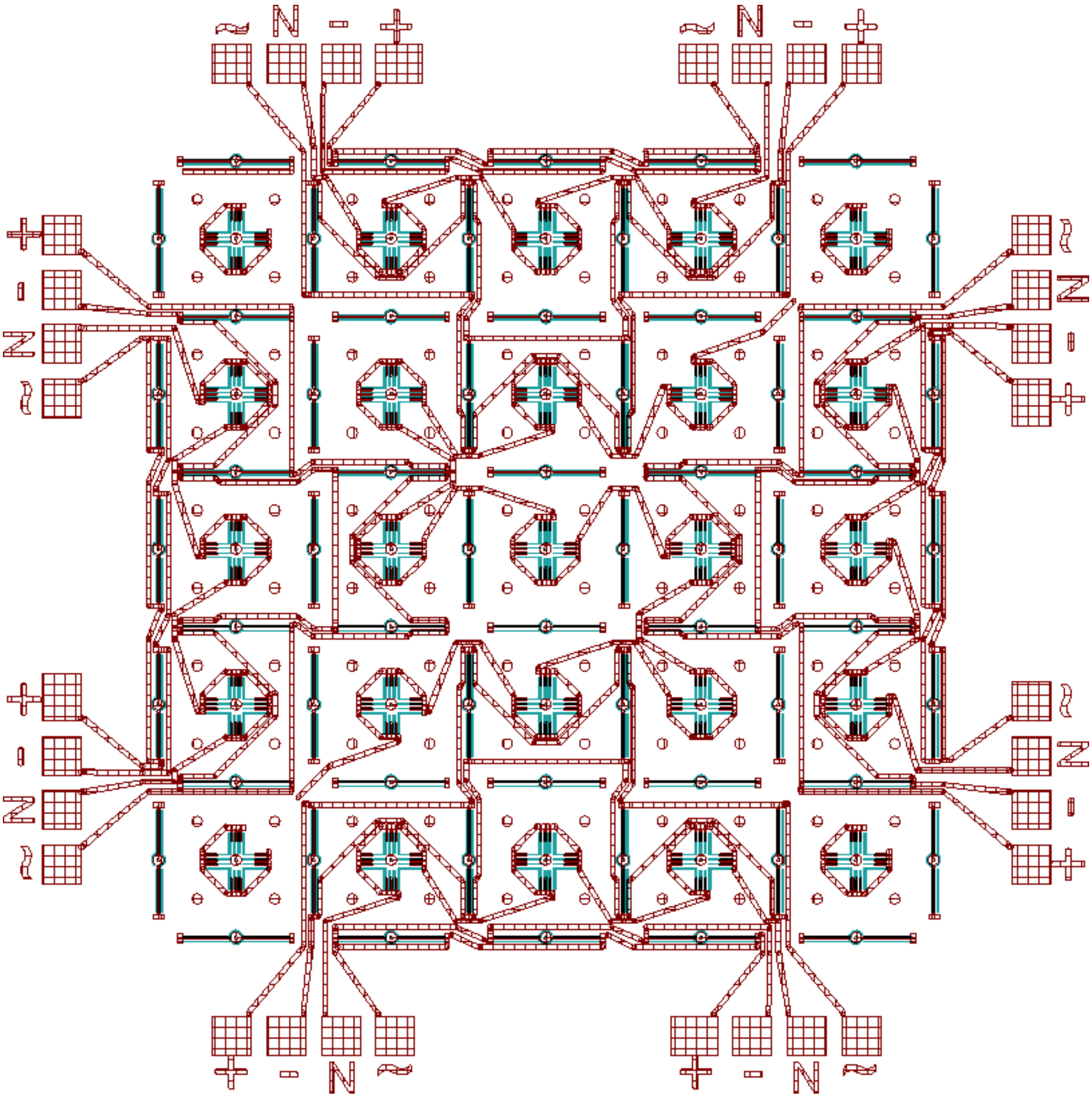

Appendix C

Process flows

C.1 Surface reaction experiment

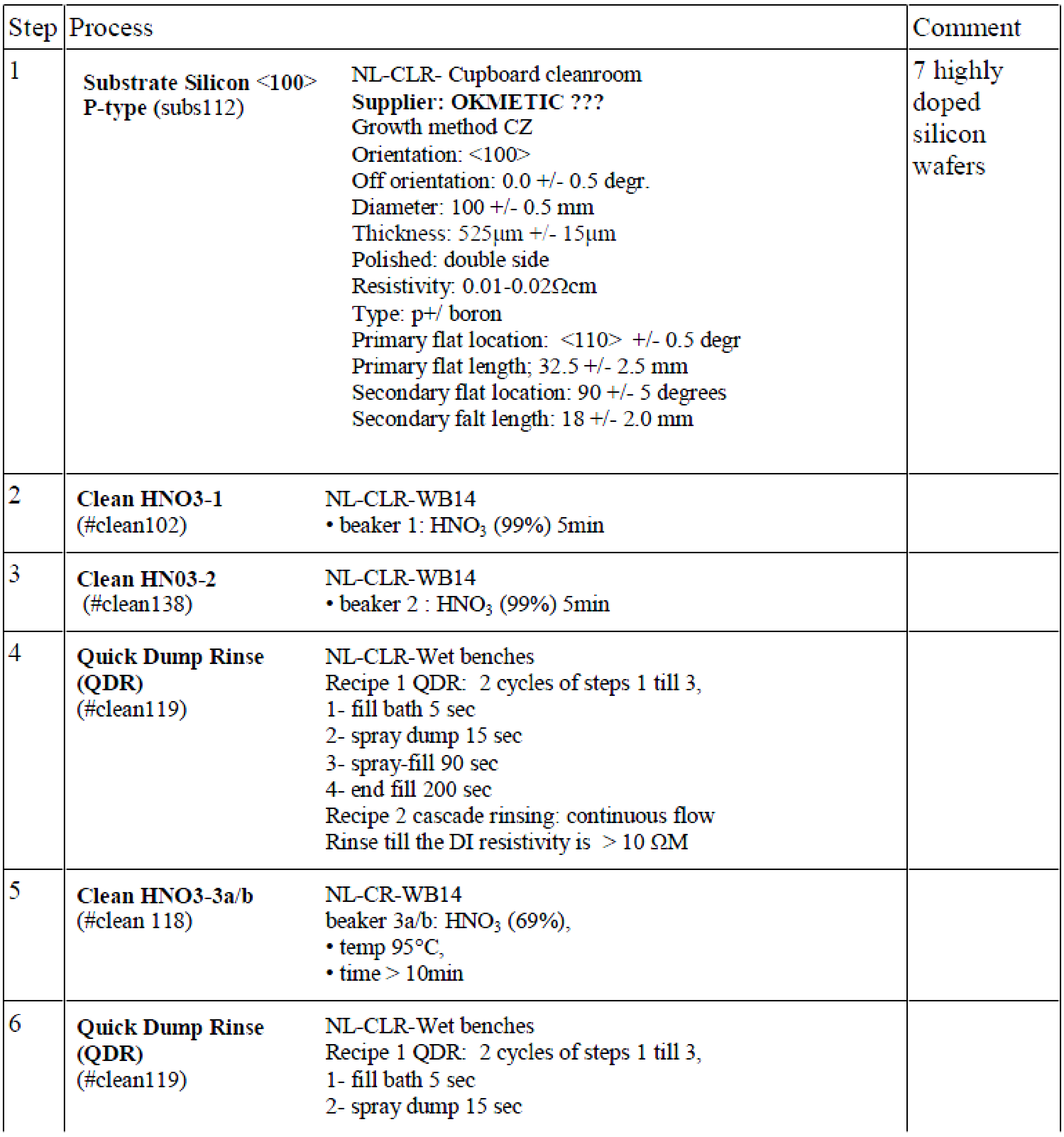

Step	Process	Comment
1	**Substrate Silicon** <100> **P-type** (subs112) NL-CLR- Cupboard cleanroom **Supplier: OKMETIC ???** Growth method CZ Orientation: <100> Off orientation: 0.0 +/- 0.5 degr. Diameter: 100 +/- 0.5 mm Thickness: 525µm +/- 15µm Polished: double side Resistivity: 0.01-0.02Ωcm Type: p+/ boron Primary flat location: <110> +/- 0.5 degr Primary flat length; 32.5 +/- 2.5 mm Secondary flat location: 90 +/- 5 degrees Secondary falt length: 18 +/- 2.0 mm	7 highly doped silicon wafers
2	**Clean HNO3-1** (#clean102) NL-CLR-WB14 • beaker 1: HNO$_3$ (99%) 5min	
3	**Clean HN03-2** (#clean138) NL-CLR-WB14 • beaker 2 : HNO$_3$ (99%) 5min	
4	**Quick Dump Rinse (QDR)** (#clean119) NL-CLR-Wet benches Recipe 1 QDR: 2 cycles of steps 1 till 3, 1- fill bath 5 sec 2- spray dump 15 sec 3- spray-fill 90 sec 4- end fill 200 sec Recipe 2 cascade rinsing: continuous flow Rinse till the DI resistivity is > 10 ΩM	
5	**Clean HNO3-3a/b** (#clean 118) NL-CR-WB14 beaker 3a/b: HNO$_3$ (69%), • temp 95°C, • time > 10min	
6	**Quick Dump Rinse (QDR)** (#clean119) NL-CLR-Wet benches Recipe 1 QDR: 2 cycles of steps 1 till 3, 1- fill bath 5 sec 2- spray dump 15 sec	

		3- spray-fill 90 sec 4- end fill 200 sec Recipe 2 cascade rinsing: continuous flow Rinse till the DI resistivity is > 10 ΩM	
7	**Etching in HF 1% (metal free)** (#etch127)	NL-CLR-WB15 use beaker HF 1% • time variable • native oxide strip: > 1 min or hydrofobic surface etchrate: TEOS **H3 (new)** = 28 nm/min Si3N4 **H2 (new)** = 0.33 nm/min	
8	**Quick Dump Rinse (QDR)** (#clean119)	NL-CLR-Wet benches Recipe 1 QDR: 2 cycles of steps 1 till 3, 1- fill bath 5 sec 2- spray dump 15 sec 3- spray-fill 90 sec 4- end fill 200 sec Recipe 2 cascade rinsing: continuous flow Rinse till the DI resistivity is > 10 ΩM	
9	**Substrate rinsing/drying Semitool** (#clean121)	NL-CLR-Wet Benches Semitool spin rinser dryer Use dedicated wafer carrier of rinser dryer Parameters/step • rinse in DI: 30 sec: 600 rpm • rinse in DI: 12.0 MΩ; 600 rpm • N2 purge: 30sec; 600 rpm • drying 1: 150 sec; 1600 rpm • drying 2: 0000 - 0000 Unload wafers	
10	**Sputtering of Ti** (#film116)	**NL-CLR-sputterke-nr. 37** Ti Target (gun #: see mis logbook) • Use Ar flow to adjust sputter pressure • Base pressure: < 1.0 e-6mbar • Sputter pressure: 6.6 e-3mbar • power: 200W • Depositionrate = 13 nm/min	Three wafers with: 10 nm, 50 nm, 100 nm Ti; Three wafers with: 10 nm, 50 nm, 100 nm Cr; One wafer only gold, no Ti or Cr
11	**Sputtering of Cr** (#film117)	**NL-CLR-Sputterke Eq.Nr. 37** Cr Target (gun #: see mis logbook) • Use Ar flow to adjust process pressure. • Base pressure: < 1.0 e-6mbar • Sputter pressure: 6.6 e-3mbar • power: 200W • Depositionrate = 15 nm/min	Three wafers with: 10 nm, 50 nm, 100 nm Ti; Three wafers with: 10 nm, 50 nm, 100 nm Cr; One wafer only

			gold, no Ti or Cr
12	**Sputtering of Au** (#film136)	**NL-CLR-Eq.Nr. 37 / Sputterke** Au Target (gun #: see mis logbook) • use Ar flow to adjust pressure • Base pressure: < 1.0 e-6mbar • Sputter pressure: 6.6 e-3mbar • power: 200W • Depositionrate = 45-50 nm/min. • MAX THICKNESS: 250 NM	100 nm
13	**Dicing of a Silicon wafer** (#back101)	**Nl-CLR- Disco DAD dicing saw** Applications: Silicon wafers, bonded silicon-silicon wafers (max 1.1mm) See #back103 for laminate of Nitto STW T10 dicing foil (80 µm) See #back104 for laminate of UV dicing foil (250µm) **Parameters dicing**: Wafer work size: 110 mm for a standard 100 mm silicon wafer Max. Feed speed: 10 mm/sec X, Y values: correspond respectively to Ch1 and Ch2 and those values are determined by mask layout Saw type NBC-Z 2050 Select in blade menu: **NBC-Z-2050** **Blade info:** Exposure 1.3 mm (maximum dicing depth for a new blade) Width: 50 um Spindle revolutions: 30. 000 rpm Depth settings: Maximum cut depth: 1.1 mm Foil thickness: See foil info Min. blade heigth: 50 µm	Breaking wafer into 4 parts (all 7)
14	**Annealing of glas, silicon and metal E2** (#therm116)	NL-CLR-Furnace E2 Contaminated furnace!! Amtech tempress omega junior (2-stack) • temp range 400, 450,500, etc up to 1100°C • gas N_2, flow 4 SLM • wafer 100mm	Annealing at 400degC in N2 for 0, 15, 30 and 170 min.
15	**Inspection by optical microscopic** (#metro102)	NL-CLR- 6 microscopes • olympus Microscope (4) • leica Microscope (2)	Inspection by microscope and making photograph of each separate wafer

C.2 Advanced bond strength experiment

C.2.1 Bottom wafer

Step	Process	Comment
1	**Substrate Silicon** <100> **P-type** (subs112) NL-CLR- Cupboard cleanroom **Supplier: OKMETIC ???** Growth method CZ Orientation: <100> Off orientation: 0.0 +/- 0.5 degr. Diameter: 100 +/- 0.5 mm Thickness: 525µm +/- 15µm Polished: double side Resistivity: 0.01-0.02Ωcm Type: p+/ boron Primary flat location: <110> +/- 0.5 degr Primary flat length; 32.5 +/- 2.5 mm Secondary flat location: 90 +/- 5 degrees Secondary falt length: 18 +/- 2.0 mm	7 highly doped silicon wafers
2	**Clean HNO3-1** (#clean102) NL-CLR-WB14 • beaker 1: HNO_3 (99%) 5min	
3	**Clean HN03-2** (#clean138) NL-CLR-WB14 • beaker 2 : HNO_3 (99%) 5min	
4	**Quick Dump Rinse (QDR)** (#clean119) NL-CLR-Wet benches Recipe 1 QDR: 2 cycles of steps 1 till 3, 1- fill bath 5 sec 2- spray dump 15 sec 3- spray-fill 90 sec 4- end fill 200 sec Recipe 2 cascade rinsing: continuous flow Rinse till the DI resistivity is > 10 ΩM	
5	**Clean HNO3-3a/b** (#clean 118) NL-CR-WB14 beaker 3a/b: HNO_3 (69%), • temp 95°C, • time > 10min	
6	**Quick Dump Rinse (QDR)** (#clean119) NL-CLR-Wet benches Recipe 1 QDR: 2 cycles of steps 1 till 3, 1- fill bath 5 sec 2- spray dump 15 sec 3- spray-fill 90 sec 4- end fill 200 sec Recipe 2 cascade rinsing: continuous flow Rinse till the DI resistivity is > 10 ΩM	
7	**Etching in HF 1% (metal free)** (#etch127) NL-CLR-WB15 use beaker HF 1% • time variable • native oxide strip: > 1 min or hydrofobic surface etchrate: TEOS **H3 (new)** = 28 nm/min Si3N4 **H2 (new)** = 0.33 nm/min	

8	**Quick Dump Rinse (QDR)** (#clean119)	NL-CLR-Wet benches Recipe 1 QDR: 2 cycles of steps 1 till 3, 1- fill bath 5 sec 2- spray dump 15 sec 3- spray-fill 90 sec 4- end fill 200 sec Recipe 2 cascade rinsing: continuous flow Rinse till the DI resistivity is > 10 ΩM	
9	**Substrate rinsing/drying Semitool** (#clean121)	NL-CLR-Wet Benches Semitool spin rinser dryer Use dedicated wafer carrier of rinser dryer Parameters/step • rinse in DI: 30 sec: 600 rpm • rinse in DI: 12.0 MΩ; 600 rpm • N2 purge: 30sec; 600 rpm • drying 1: 150 sec; 1600 rpm • drying 2: 0000 - 0000 Unload wafers	
10	**Sputtering of Ti** (#film116)	**NL-CLR-sputterke-nr. 37** Ti Target (gun #: see mis logbook) • Use Ar flow to adjust sputter pressure • Base pressure: < 1.0 e-6mbar • Sputter pressure: 6.6 e-3mbar • power: 200W • Depositionrate = 13 nm/min	Three wafers with: 10 nm, 50 nm, 100 nm Ti; Three wafers with: 10 nm, 50 nm, 100 nm Cr; One wafer only gold, no Ti or Cr
11	**Sputtering of Cr** (#film117)	**NL-CLR-Sputterke Eq.Nr. 37** Cr Target (gun #: see mis logbook) • Use Ar flow to adjust process pressure. • Base pressure: < 1.0 e-6mbar • Sputter pressure: 6.6 e-3mbar • power: 200W • Depositionrate = 15 nm/min	Three wafers with: 10 nm, 50 nm, 100 nm Ti; Three wafers with: 10 nm, 50 nm, 100 nm Cr; One wafer only gold, no Ti or Cr
12	**Sputtering of Au** (#film136)	**NL-CLR-Eq.Nr. 37 / Sputterke** Au Target (gun #: see mis logbook) • use Ar flow to adjust pressure • Base pressure: < 1.0 e-6mbar • Sputter pressure: 6.6 e-3mbar • power: 200W • Depositionrate = 45-50 nm/min. • MAX THICKNESS: 250 NM	100 nm

C.2.2 Top Wafer

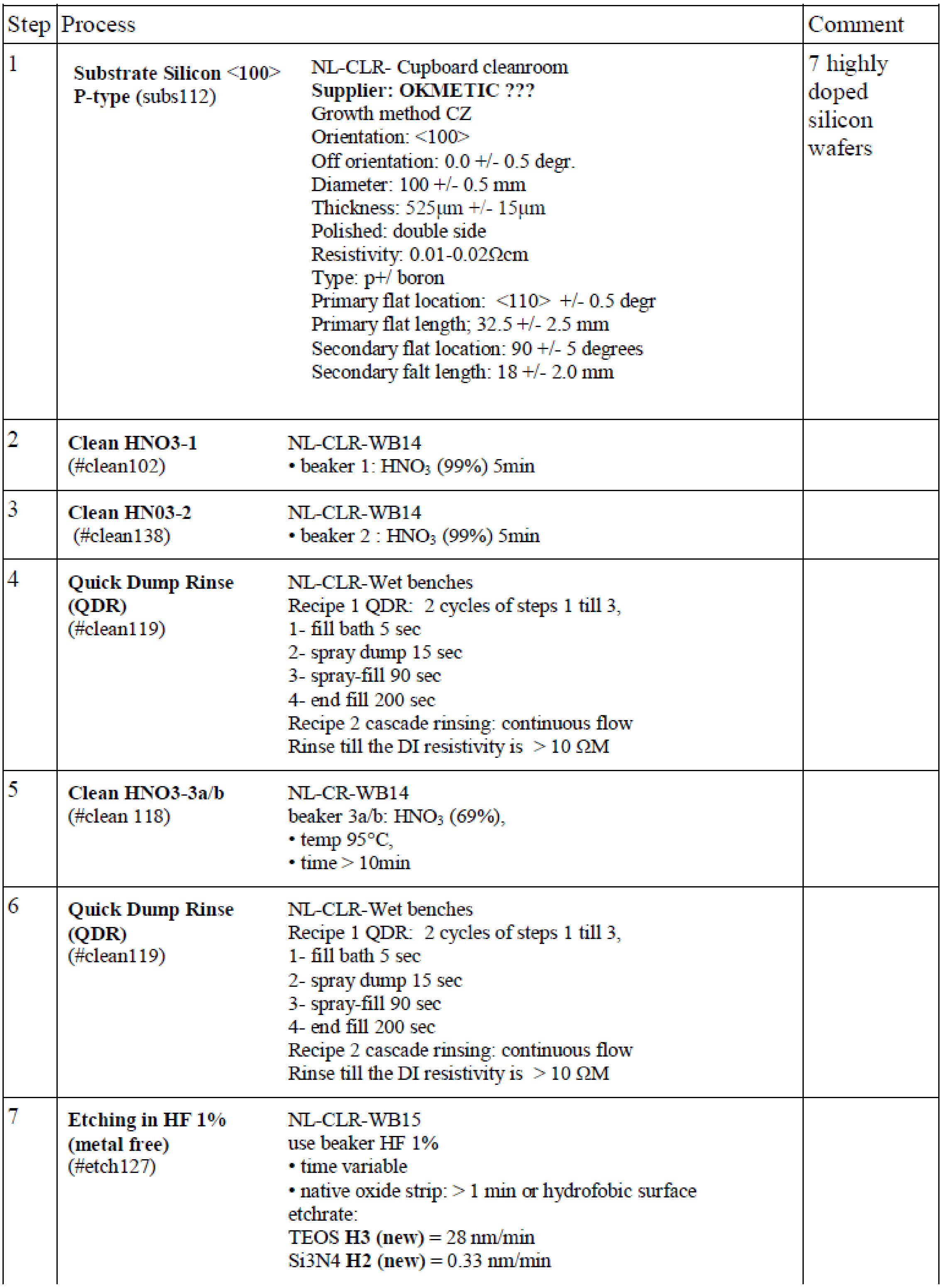

Step	Process		Comment
1	**Substrate Silicon** <100> **P-type** (subs112)	NL-CLR- Cupboard cleanroom **Supplier: OKMETIC ???** Growth method CZ Orientation: <100> Off orientation: 0.0 +/- 0.5 degr. Diameter: 100 +/- 0.5 mm Thickness: 525µm +/- 15µm Polished: double side Resistivity: 0.01-0.02Ωcm Type: p+/ boron Primary flat location: <110> +/- 0.5 degr Primary flat length; 32.5 +/- 2.5 mm Secondary flat location: 90 +/- 5 degrees Secondary falt length: 18 +/- 2.0 mm	7 highly doped silicon wafers
2	**Clean HNO3-1** (#clean102)	NL-CLR-WB14 • beaker 1: HNO_3 (99%) 5min	
3	**Clean HN03-2** (#clean138)	NL-CLR-WB14 • beaker 2 : HNO_3 (99%) 5min	
4	**Quick Dump Rinse (QDR)** (#clean119)	NL-CLR-Wet benches Recipe 1 QDR: 2 cycles of steps 1 till 3, 1- fill bath 5 sec 2- spray dump 15 sec 3- spray-fill 90 sec 4- end fill 200 sec Recipe 2 cascade rinsing: continuous flow Rinse till the DI resistivity is > 10 ΩM	
5	**Clean HNO3-3a/b** (#clean 118)	NL-CR-WB14 beaker 3a/b: HNO_3 (69%), • temp 95°C, • time > 10min	
6	**Quick Dump Rinse (QDR)** (#clean119)	NL-CLR-Wet benches Recipe 1 QDR: 2 cycles of steps 1 till 3, 1- fill bath 5 sec 2- spray dump 15 sec 3- spray-fill 90 sec 4- end fill 200 sec Recipe 2 cascade rinsing: continuous flow Rinse till the DI resistivity is > 10 ΩM	
7	**Etching in HF 1% (metal free)** (#etch127)	NL-CLR-WB15 use beaker HF 1% • time variable • native oxide strip: > 1 min or hydrofobic surface etchrate: TEOS **H3 (new)** = 28 nm/min Si3N4 **H2 (new)** = 0.33 nm/min	

8	**Quick Dump Rinse (QDR)** (#clean119)	NL-CLR-Wet benches Recipe 1 QDR: 2 cycles of steps 1 till 3, 1- fill bath 5 sec 2- spray dump 15 sec 3- spray-fill 90 sec 4- end fill 200 sec Recipe 2 cascade rinsing: continuous flow Rinse till the DI resistivity is > 10 ΩM	
9	**Substrate rinsing/drying Semitool** (#clean121)	NL-CLR-Wet Benches Semitool spin rinser dryer Use dedicated wafer carrier of rinser dryer Parameters/step • rinse in DI: 30 sec: 600 rpm • rinse in DI: 12.0 MΩ; 600 rpm • N2 purge: 30sec; 600 rpm • drying 1: 150 sec; 1600 rpm • drying 2: 0000 - 0000 Unload wafers	
10	**Dehydration bake** (#lith102)	NL-CLR-WB21/22 dehydration bake at hotplate • temp. 120°C • time: 5min	Continue immedialy with priming the step!
11	**Priming (liquid)** (#lith101)	NL-CLR-WB21/22 Primer: HexaMethylDiSilazane (HMDS) use spincoater: • program: 4000 (4000rpm, 30sec)	
12	**Coating Olin Oir 907-17** (#lith105)	NL-CLR-WB21 Coating: Primus spinner • olin oir 907-17 • spin Program: 4000 (4000rpm, 30sec) Prebake: hotplate • time 90 sec • temp 95 °C	use spacer on hotplate for prebake
13	**Priming (liquid)** (#lith101)	NL-CLR-WB21/22 Primer: HexaMethylDiSilazane (HMDS) use spincoater: • program: 4000 (4000rpm, 30sec)	
14	**Lithography - Coating Olin OiR 908-35** (#lith106)	NL-CLR- WB21 Coating: Primus coater • Olin OiR 908-35 • Spin Program: 4000 (4000rpm, 30sec) Prebake: Hotplate • Time 120s • temp 95 °C	use spacer on hotplate for prebake
15	**Alignment & Exposure Olin OiR 907-17** (#lith121)	NL-CLR- EV620 Electronic Vision Group EV620 Mask Aligner • Hg-lamp: 12 mW/cm^2 • Exposure Time: 4sec	exposure time: 4 sec.
16	**Postbake Olin OiR resist**	NL-CLR-WB21 postbake: Hotplate	1 min.

<table>
<tr><td></td><td>(#lith109)</td><td>• temp 120°C
• time 10min</td><td></td></tr>
<tr><td>17</td><td>Development Olin OiR resist
(#lith111)</td><td>NL-CLR-WB21
After exposurebBake : hotplate
• time 60sec
• temp 120°C
development: developer: OPD4262
• time: 30sec in beaker 1
• time: 15-30sec in beaker 2</td><td>30 sec. + 15 sec.</td></tr>
<tr><td>18</td><td>Substrate drying
(#clean120)</td><td>NL-CLR-WB
Single wafer dryer
• speed: 2500 rpm, 60 sec with 30 sec N_2 flow</td><td></td></tr>
<tr><td>19</td><td>Alignment & Exposure Olin 908-35
(#lith122)</td><td>NL-CLR- EV620
• Electronic Vision Group EV620 Mask Aligner
• Hg lamp: 12 mW/cm ^{2}
• Exposure Time: 9sec</td><td>exposure time: 9 sec.</td></tr>
<tr><td>20</td><td>Postbake Olin OiR resist
(#lith109)</td><td>NL-CLR-WB21
postbake: Hotplate
• temp 120°C
• time 10min</td><td>1 min.</td></tr>
<tr><td>21</td><td>Development Olin OiR resist
(#lith111)</td><td>NL-CLR-WB21
After exposurebBake : hotplate
• time 60sec
• temp 120°C
development: developer: OPD4262
• time: 30sec in beaker 1
• time: 15-30sec in beaker 2</td><td>30 sec. + 15 sec.</td></tr>
<tr><td>22</td><td>Postbake Olin OiR resist
(#lith109)</td><td>NL-CLR-WB21
postbake: Hotplate
• temp 120°C
• time 10min</td><td>hardbake for 3 hours for wafer-trough etching</td></tr>
<tr><td>23</td><td>Inspection by optical microscope
(#metro101)</td><td>NL-CLR- Nikon Microscope
• dedicated microscope for lithography inspection</td><td>check pattern</td></tr>
<tr><td>24</td><td>DRIE of of Si pulsed C4F8 at -40°C
(#etch175)</td><td>NL-CLR-Adixen SE
Application: trenches, wafer through using thick photoresist (908-35)
Use: C4F8 flow and CCP for tuning process.
<table>
<tr><th>Parameters</th><th>Etch</th><th>Deposition</th></tr>
<tr><td>Gas</td><td>SF_6</td><td>C_4F_8</td></tr>
<tr><td>Flow (sccm)</td><td>400</td><td>10 - 40</td></tr>
<tr><td>Time (sec)</td><td>4</td><td>0.5</td></tr>
<tr><td>Priority</td><td>2</td><td>1</td></tr>
<tr><td>APC %</td><td>15</td><td>15</td></tr>
<tr><td>ICP (Watt)</td><td>2500</td><td>2500</td></tr>
<tr><td>CCP (Watt)</td><td>nvt</td><td>20</td></tr>
</table>
</td><td>10 micron, pillar side</td></tr>
</table>

<table>
<tr>
<td></td>
<td></td>
<td>
<table>
<tr><td>Pulsed (msec)</td><td>nvt</td><td>20on/180off</td></tr>
<tr><td>SH (mm)</td><td>110</td><td>110</td></tr>
<tr><td>Electrode temp.</td><td>-40 °C</td><td>-40 °C</td></tr>
<tr><td>He (bar)</td><td>10</td><td>10</td></tr>
</table>
<table>
<tr><th>CCP [w]</th><th>On/off[msec]</th><th>C4F8 [sscm]</th><th>Er resist nm/min</th><th>silicon {um/min]</th></tr>
<tr><td>20</td><td>20/180</td><td>20</td><td>33-50</td><td>10</td></tr>
<tr><td>20</td><td>35/165</td><td>25</td><td>80</td><td>10</td></tr>
</table>
</td>
<td></td>
</tr>
<tr>
<td>25</td>
<td>Dupont MX 5020 foil for DRIE
(#lith192)</td>
<td>NL-CLR-
Material: Dupont MX5020 foil
Application: wafer through etching using Adixen SE
Procedure: appling MX5020
• Start with the lithography process for etching mask
• remove plastic protection (has no color) from backside of the foil
• Apply the foil to the wafer with a roller
• Avoid air bubbles, retract the foil if bubbles are present
• Protect the photoresist mask with a blue tissue or bare silicon wafer during laminating
• Guide the wafer with foil by hand through the laminator, Temp 90°C, speed 2
• Before DRIE etching remove the plastic protection foil!
DRIE Adixen: Temperature range: -100°C up to 20 °C.
Removal of MX5020
• Start with O2 plasma in Tepla 300 or 300E (metals are allowed)
• Continue with HN03 (99%) WB6
• Use a piranha clean: private use (WB9)</td>
<td>Laminate on pillar side. Use A4 CR paper to protect the silicon side of the wafer, no A4 paper on the foil side to maintain good heat-transfer</td>
</tr>
<tr>
<td>26</td>
<td>DRIE of of Si pulsed C4F8 at -40°C
(#etch175)</td>
<td>NL-CLR-Adixen SE
Application: trenches, wafer through using thick photoresist (908-35)
Use: C4F8 flow and CCP for tuning process.
<table>
<tr><th>Parameters</th><th>Etch</th><th>Deposition</th></tr>
<tr><td>Gas</td><td>SF_6</td><td>C_4F_8</td></tr>
<tr><td>Flow (sccm)</td><td>400</td><td>10 - 40</td></tr>
<tr><td>Time (sec)</td><td>4</td><td>0.5</td></tr>
<tr><td>Priority</td><td>2</td><td>1</td></tr>
<tr><td>APC %</td><td>15</td><td>15</td></tr>
<tr><td>ICP (Watt)</td><td>2500</td><td>2500</td></tr>
<tr><td>CCP (Watt)</td><td>nvt</td><td>20</td></tr>
<tr><td>Pulsed (msec)</td><td>nvt</td><td>20on/180off</td></tr>
<tr><td>SH (mm)</td><td>110</td><td>110</td></tr>
<tr><td>Electrode temp.</td><td>-40 °C</td><td>-40 °C</td></tr>
<tr><td>He (bar)</td><td>10</td><td>10</td></tr>
</table>
<table>
<tr><th>CCP [w]</th><th>On/off[msec]</th><th>C4F8 [sscm]</th><th>Er resist nm/min</th><th>silicon {um/min]</th></tr>
<tr><td>20</td><td>20/180</td><td>20</td><td>33-50</td><td>10</td></tr>
<tr><td>20</td><td>35/165</td><td>25</td><td>80</td><td>10</td></tr>
</table>
</td>
<td>Temp: -40 degC, Time: 40 min.</td>
</tr>
<tr>
<td>27</td>
<td>Stripping of resist in</td>
<td>NL-CLR- Tepla 300E</td>
<td>2 hours,</td>
</tr>
</table>

	oxygen plasma (#lith117)	• Barrel Etcher (2.45 GHz) • Multipurpose sytem • O_2 flow: 200sccm (50%) • Power: 500W • Pressure: 1.2 mbar Values for olin oir resist: • Time: 10 min for 1-3 wafers, 400 nm/min • Time: 20 min for 4-10 wafers • End point detection by visual inspection of the plasma color. • Blue color means still photoresist on the wafer, purple means clean.	check if foil is removed
28	**Cleaning piranha** (#clean117)	NL-CLR-WB18 Mixture: H_2SO_4 :H_2O_2 (3:1) vol% • start fill; bath is filled H_2SO_4 • continue; the H_2O_2 is added • temperature will increase till (?) 130°C, set point is 85°C • cleaning time 15min • Quick Dump Rinse $<0.1\mu S$ for spin drying • Quick Dump Rinse short for Semitool Rinse Dryer	20 min.
29	**Etching in HF 1%** **(metal free)** (#etch127)	NL-CLR-WB15 use beaker HF 1% • time variable • native oxide strip: > 1 min or hydrofobic surface etchrate: TEOS **H3 (new)** = 28 nm/min Si3N4 **H2 (new)** = 0.33 nm/min	
30	**Quick Dump Rinse (QDR)** (#clean119)	NL-CLR-Wet benches Recipe 1 QDR: 2 cycles of steps 1 till 3, 1- fill bath 5 sec 2- spray dump 15 sec 3- spray-fill 90 sec 4- end fill 200 sec Recipe 2 cascade rinsing: continuous flow Rinse till the DI resistivity is $> 10\ \Omega M$	
31	**Substrate rinsing/drying Semitool** (#clean121)	NL-CLR-Wet Benches Semitool spin rinser dryer Use dedicated wafer carrier of rinser dryer Parameters/step • rinse in DI: 30 sec: 600 rpm • rinse in DI: 12.0 MΩ; 600 rpm • N2 purge: 30sec; 600 rpm • drying 1: 150 sec; 1600 rpm • drying 2: 0000 - 0000 Unload wafers	
32	**Sputtering of Ti** (#film116)	**NL-CLR-sputterke-nr. 37** Ti Target (gun #: see mis logbook) • Use Ar flow to adjust sputter pressure • Base pressure: < 1.0 e-6mbar • Sputter pressure: 6.6 e-3mbar • power: 200W • Depositionrate = 13 nm/min	Three wafers with: 10 nm, 50 nm, 100 nm Ti; Three wafers with: 10 nm, 50 nm, 100 nm

		Cr; One wafer only gold, no Ti or Cr
33	**Sputtering of Cr** (#film117) **NL-CLR-Sputterke Eq.Nr. 37** Cr Target (gun #: see mis logbook) • Use Ar flow to adjust process pressure. • Base pressure: < 1.0 e-6mbar • Sputter pressure: 6.6 e-3mbar • power: 200W • Depositionrate = 15 nm/min	Three wafers with: 10 nm, 50 nm, 100 nm Ti; Three wafers with: 10 nm, 50 nm, 100 nm Cr; One wafer only gold, no Ti or Cr
34	**Sputtering of Au** (#film136) **NL-CLR-Eq.Nr. 37 / Sputterke** Au Target (gun #: see mis logbook) • use Ar flow to adjust pressure • Base pressure: < 1.0 e-6mbar • Sputter pressure: 6.6 e-3mbar • power: 200W • Depositionrate = 45-50 nm/min. • MAX THICKNESS: 250 NM	100 nm

C.2.3 Bonding

Step	Process	Comment
1	**EV501 Anodic bonding** (#bond105) NL-CLR-EVG /EV501 bond tool • Temperature 400°C • Vacuum better then 10^{-1} mbar • High voltage 1000 Volt • Pressure 300 N • Total process time 2 hours • First wafer Silicon • Second wafer Pyrex/Borofloat glass • Alignment can be done with EV620 maskaligner	Pillar wafer at the bottom. Recipe: Kees

Appendix D

Surface reaction images

D.1 Surfaces after annealing

D.1.1 100 nm Au

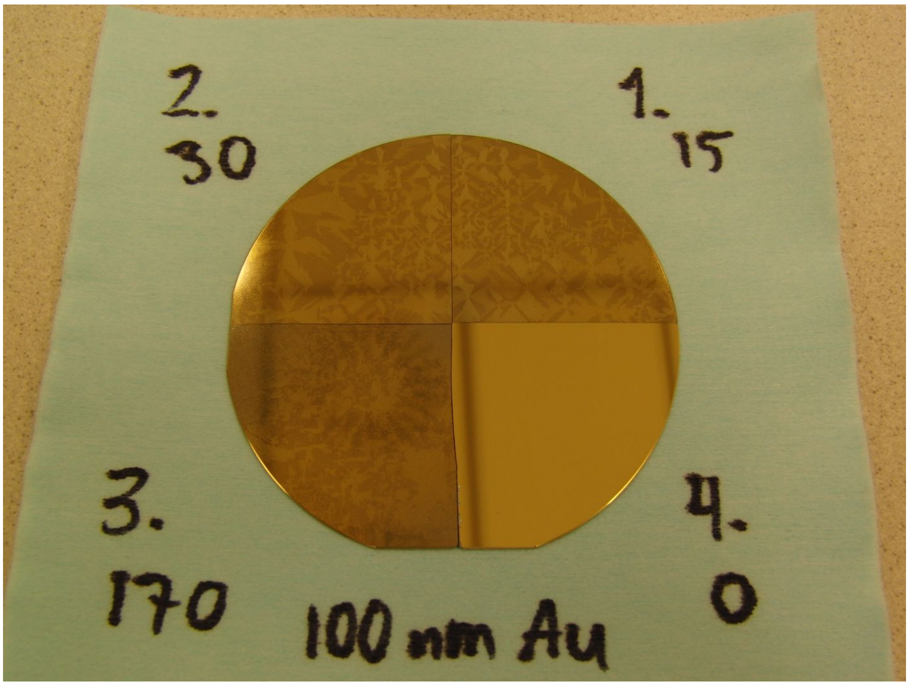

Figure D.1

D.1.2 10 nm Ti, 100 nm Au

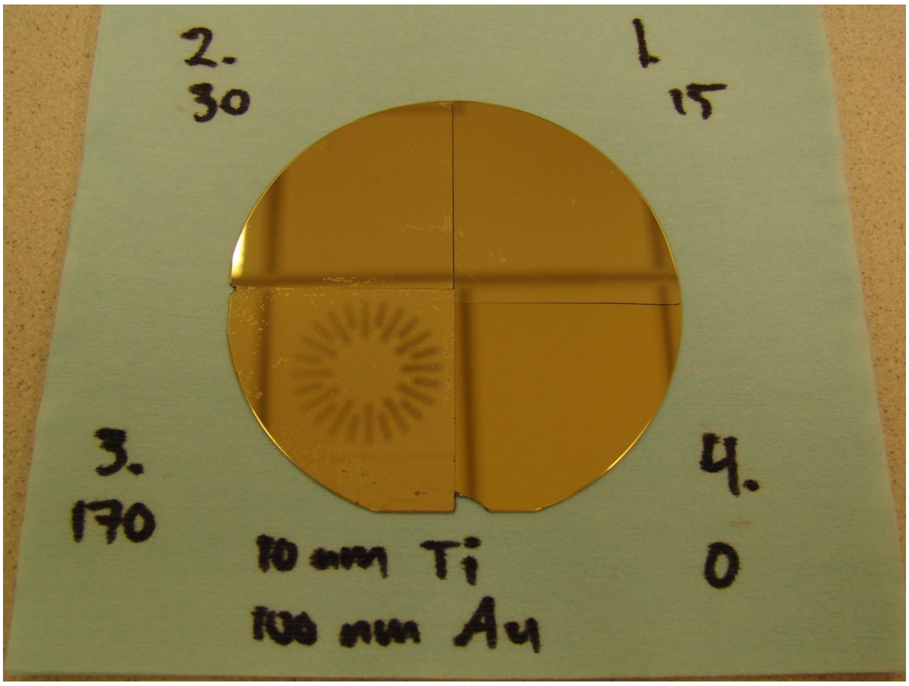

Figure D.2

D.1.3 50 nm Ti, 100 nm Au

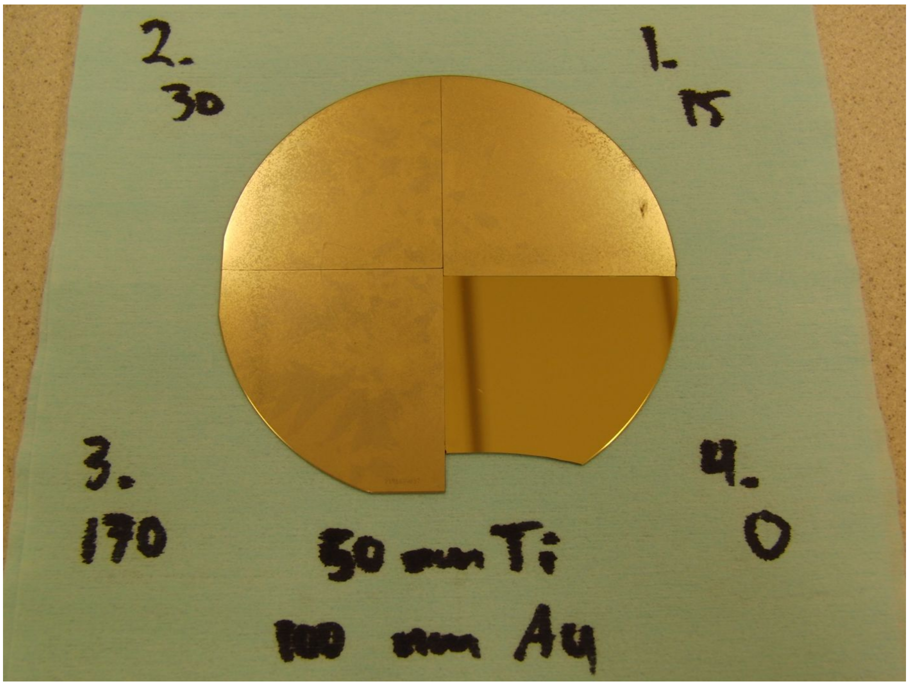

Figure D.3

D.1.4 100 nm Ti, 100 nm Au

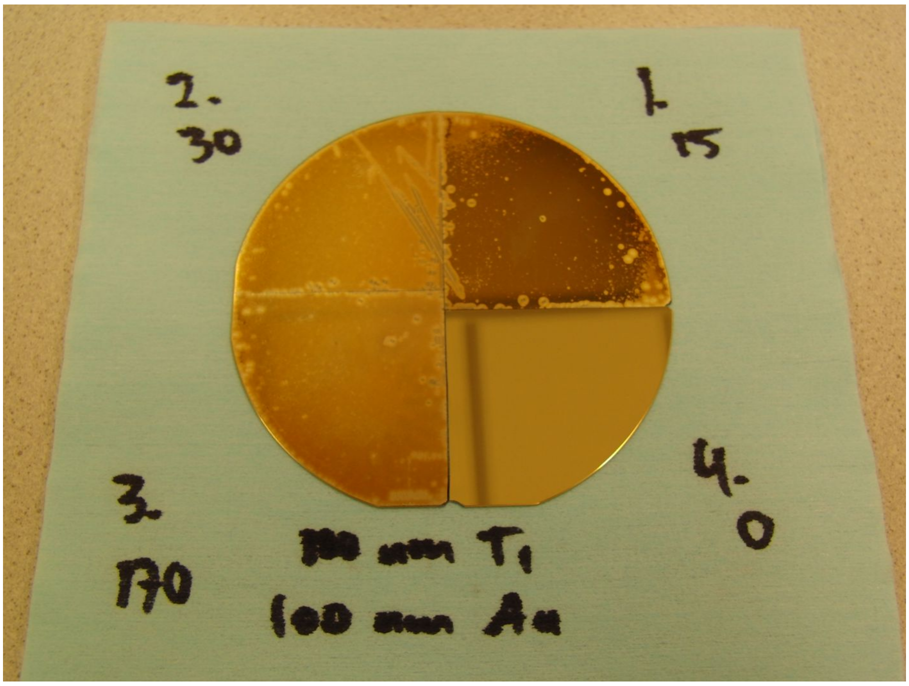

Figure D.4

D.1.5 10 nm Cr, 100 nm Au

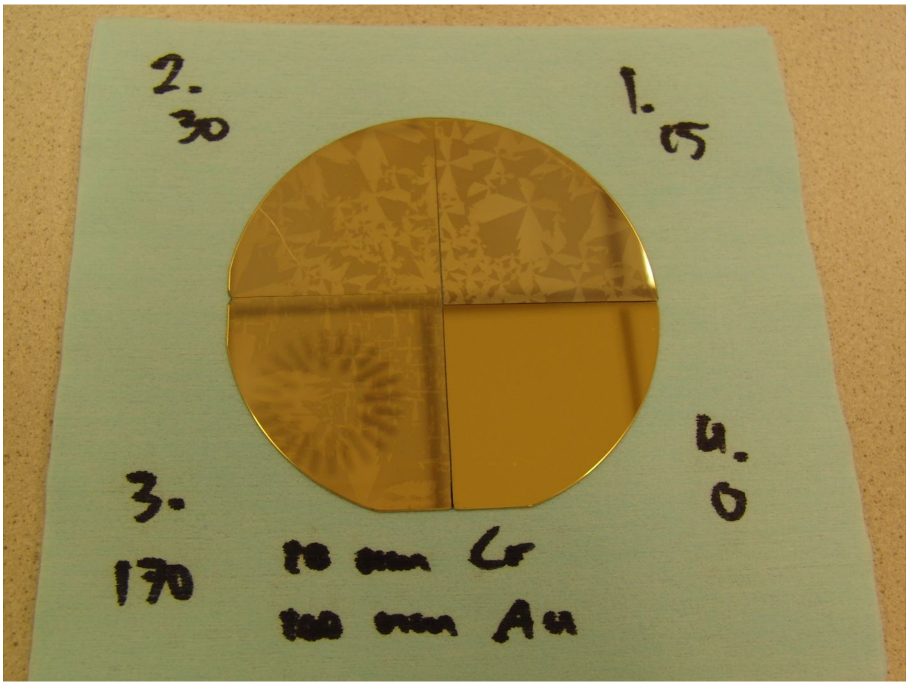

Figure D.5

D.1.6 50 nm Cr, 100 nm Au

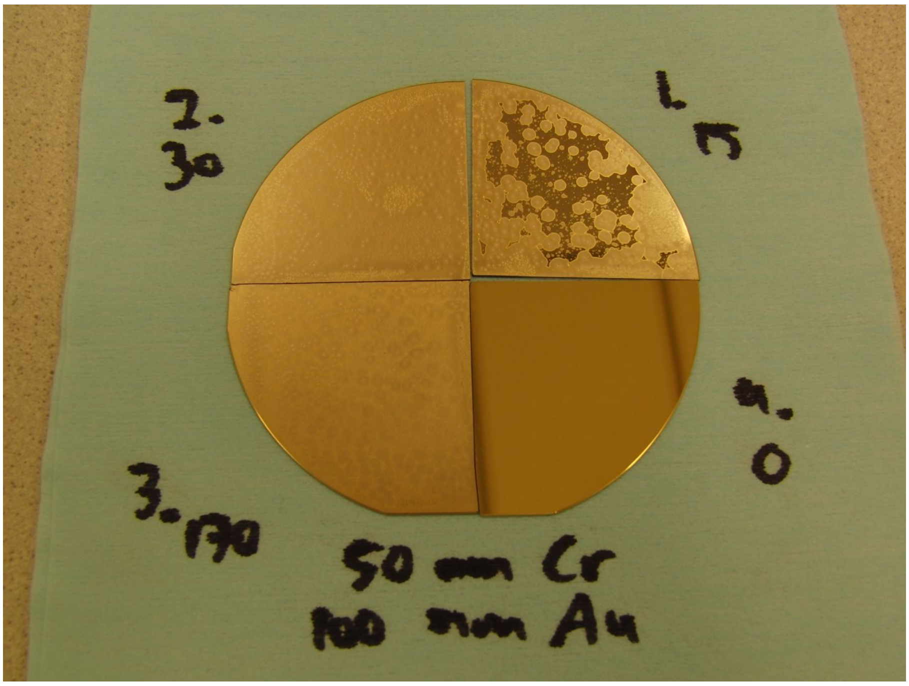

Figure D.6

D.1.7 100 nm Cr, 100 nm Au

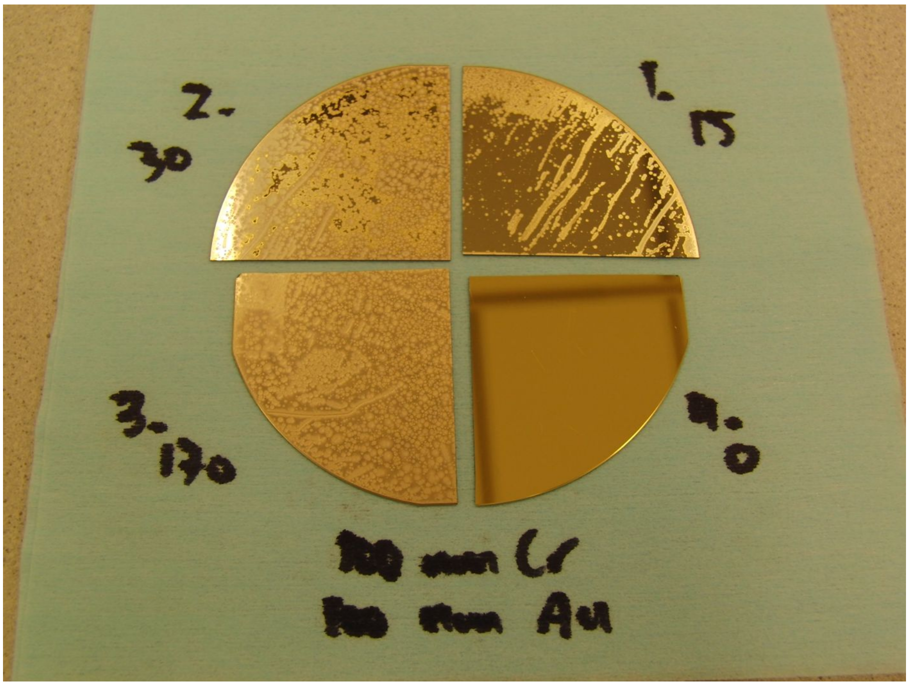

Figure D.7

D.2 Surfaces after etching

D.2.1 100 nm Au

Annealing time: 15 min.

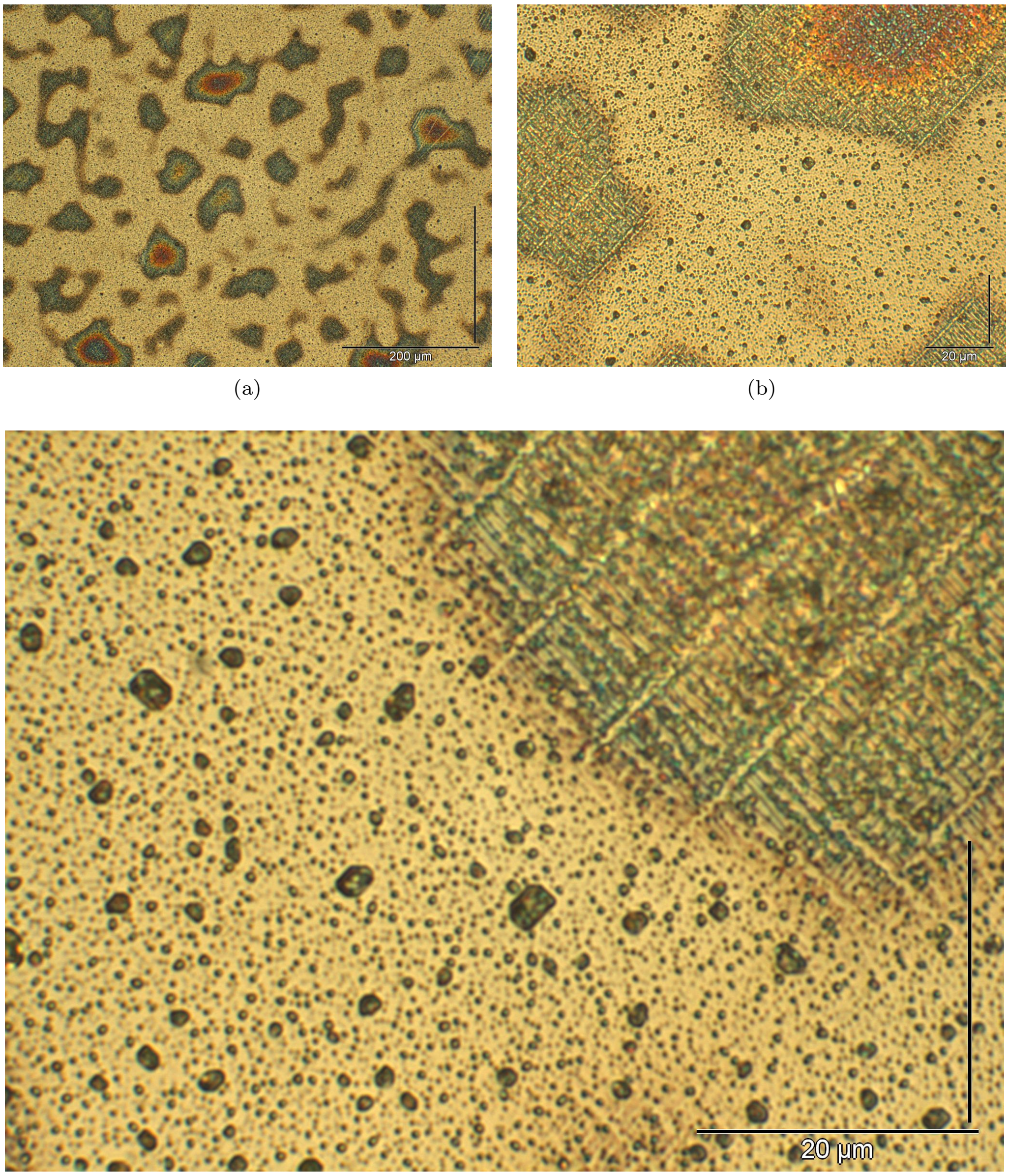

(a) (b)

(c)

Figure D.8

Annealing time: 30 min.

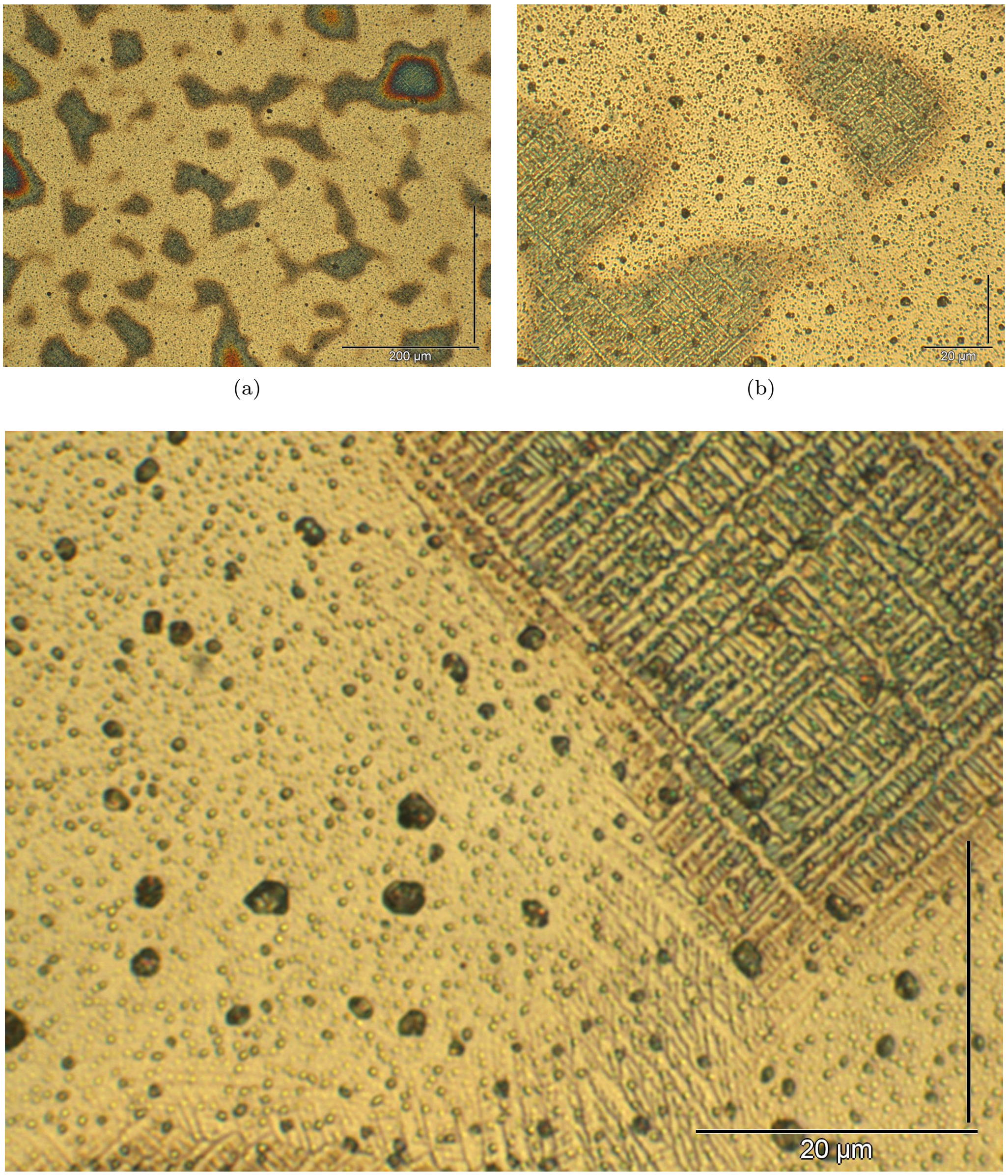

(a) (b)

(c)

Figure D.9

Annealing time: 170 min.

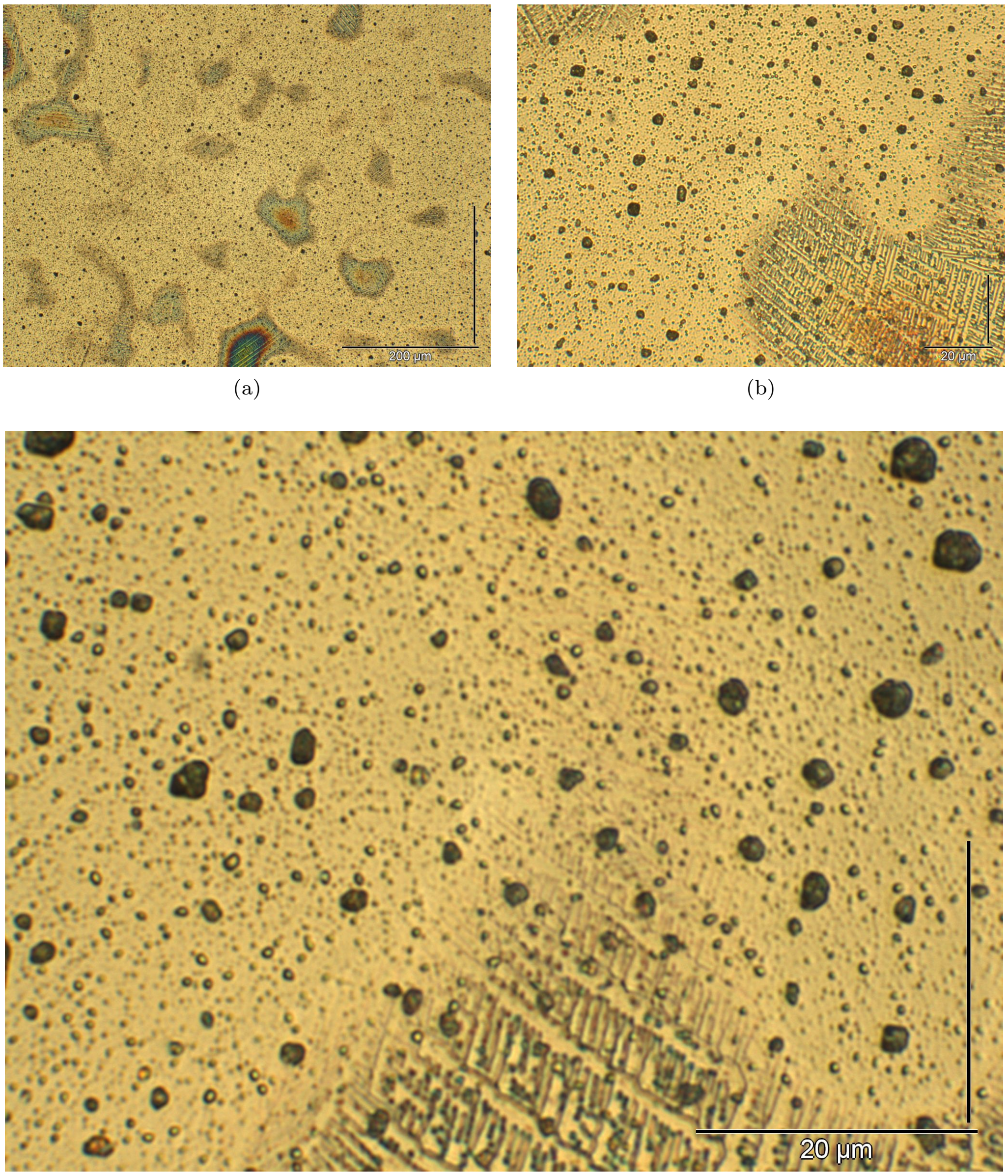

(a) (b)

(c)

Figure D.10

D.2.2 10 nm Ti, 100 nm Au

Annealing time: 15 min.

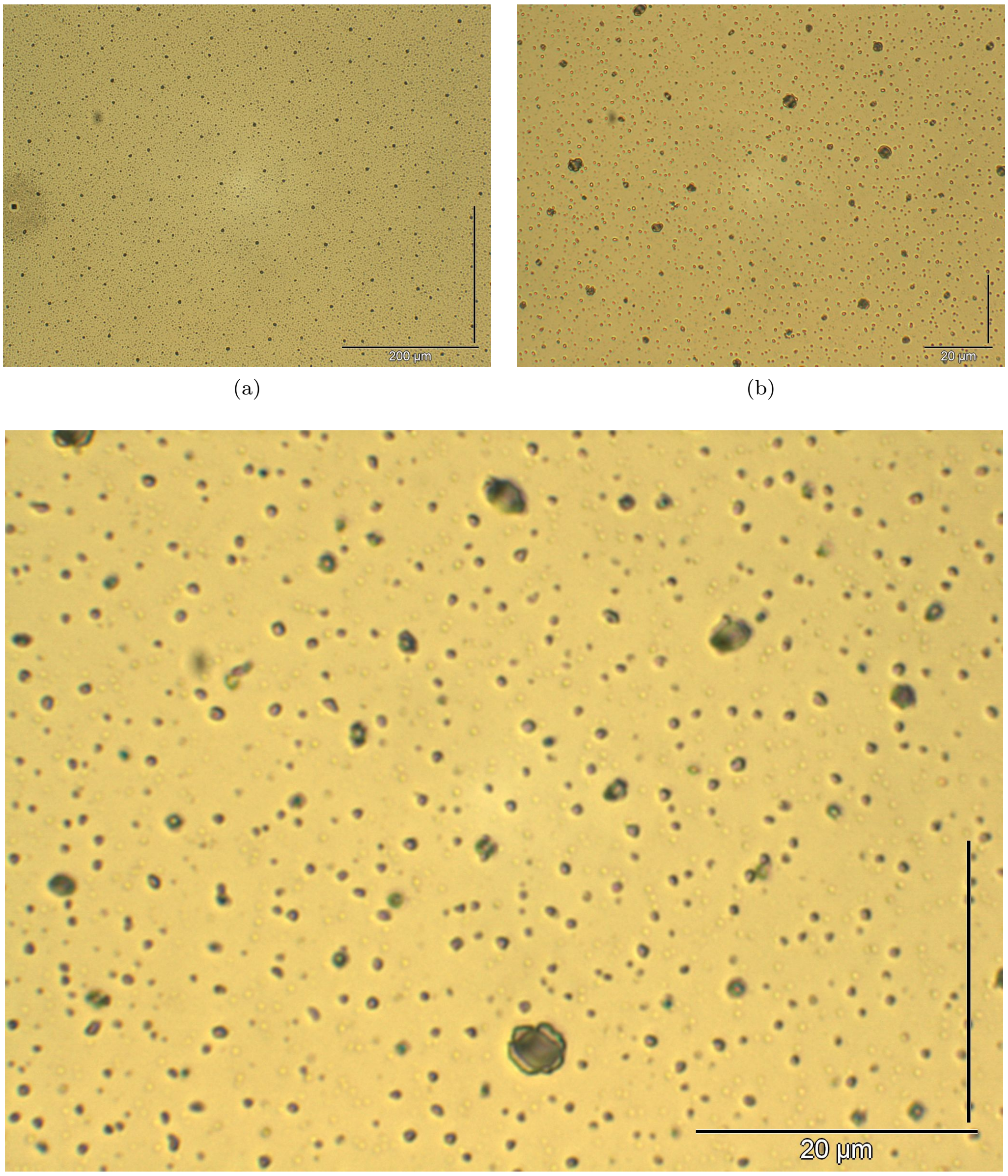

(a) (b)

(c)

Figure D.11

Annealing time: 30 min.

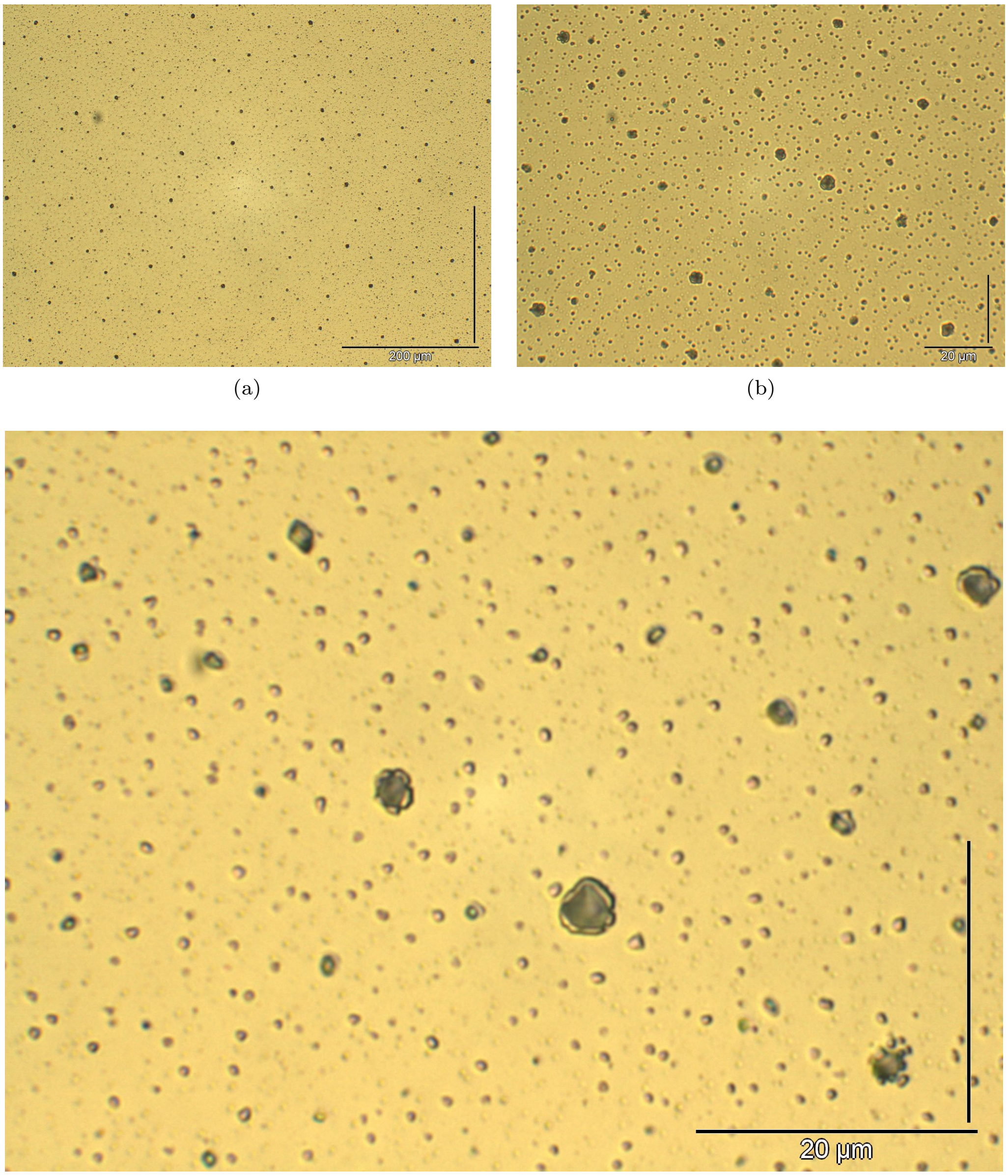

(a)

(b)

(c)

Figure D.12

Annealing time: 170 min.

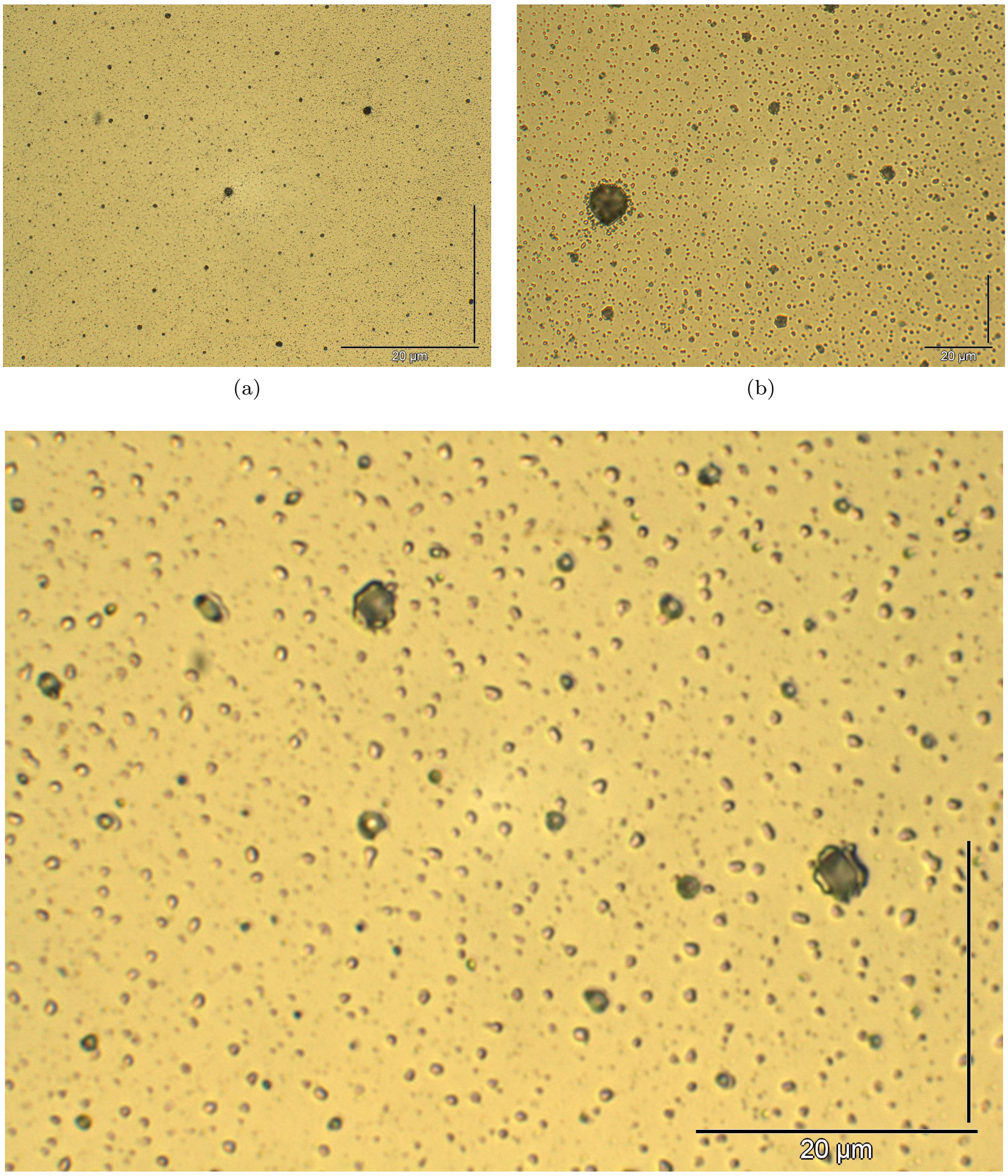

(a) (b)

(c)

Figure D.13

D.2.3 50 nm Ti, 100 nm Au

Annealing time: 15 min.

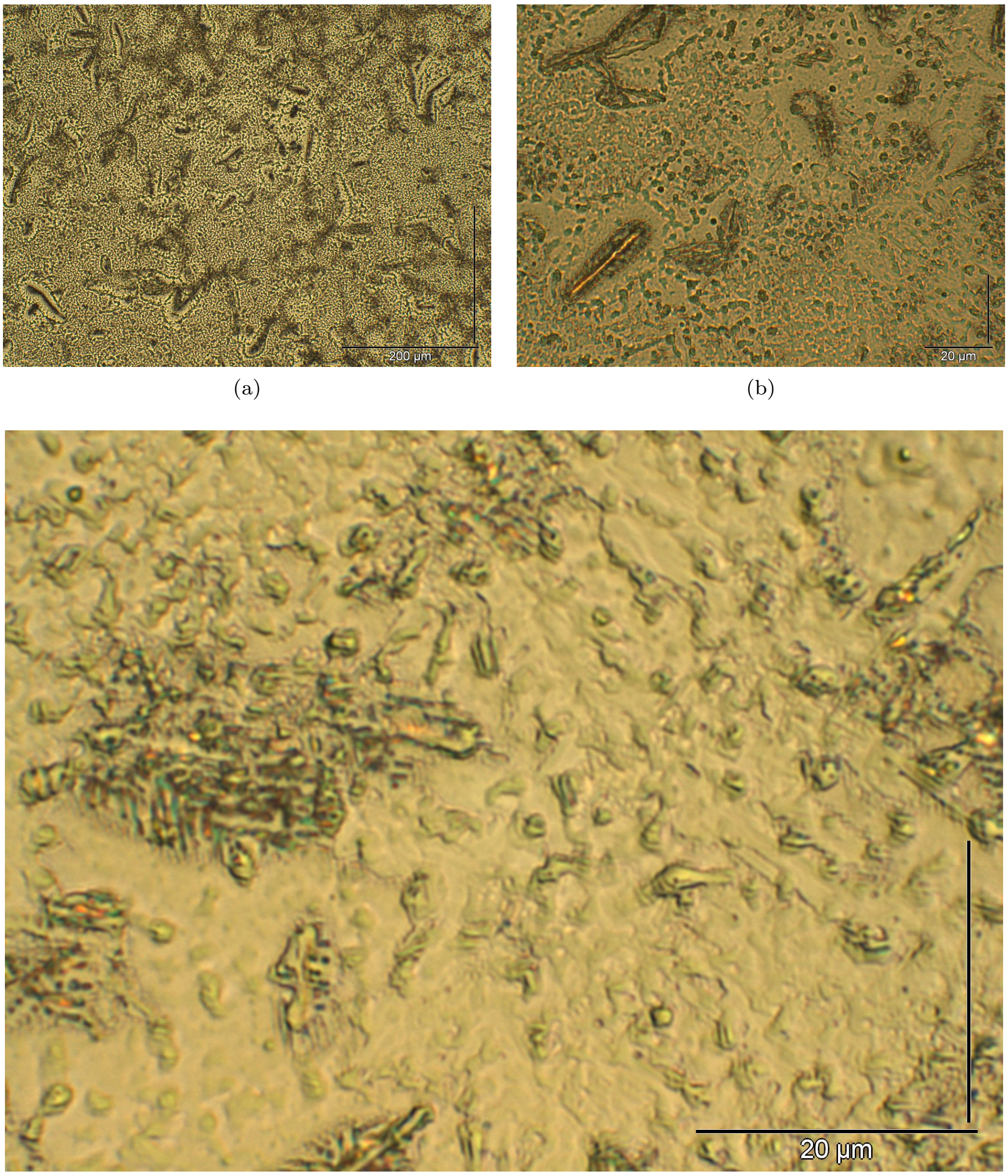

(a) (b)

(c)

Figure D.14

Annealing time: 30 min.

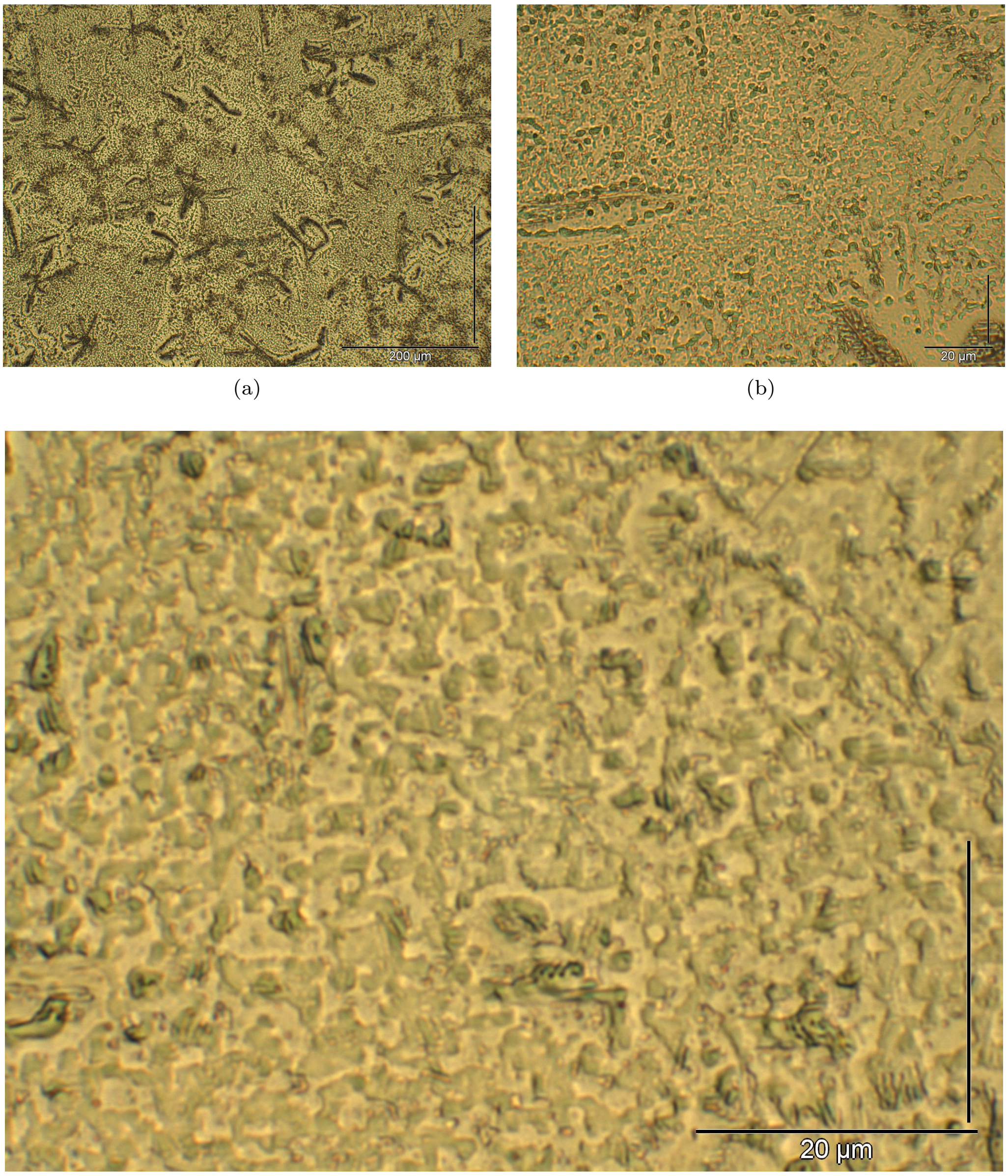

(a) (b)

(c)

Figure D.15

Annealing time: 170 min.

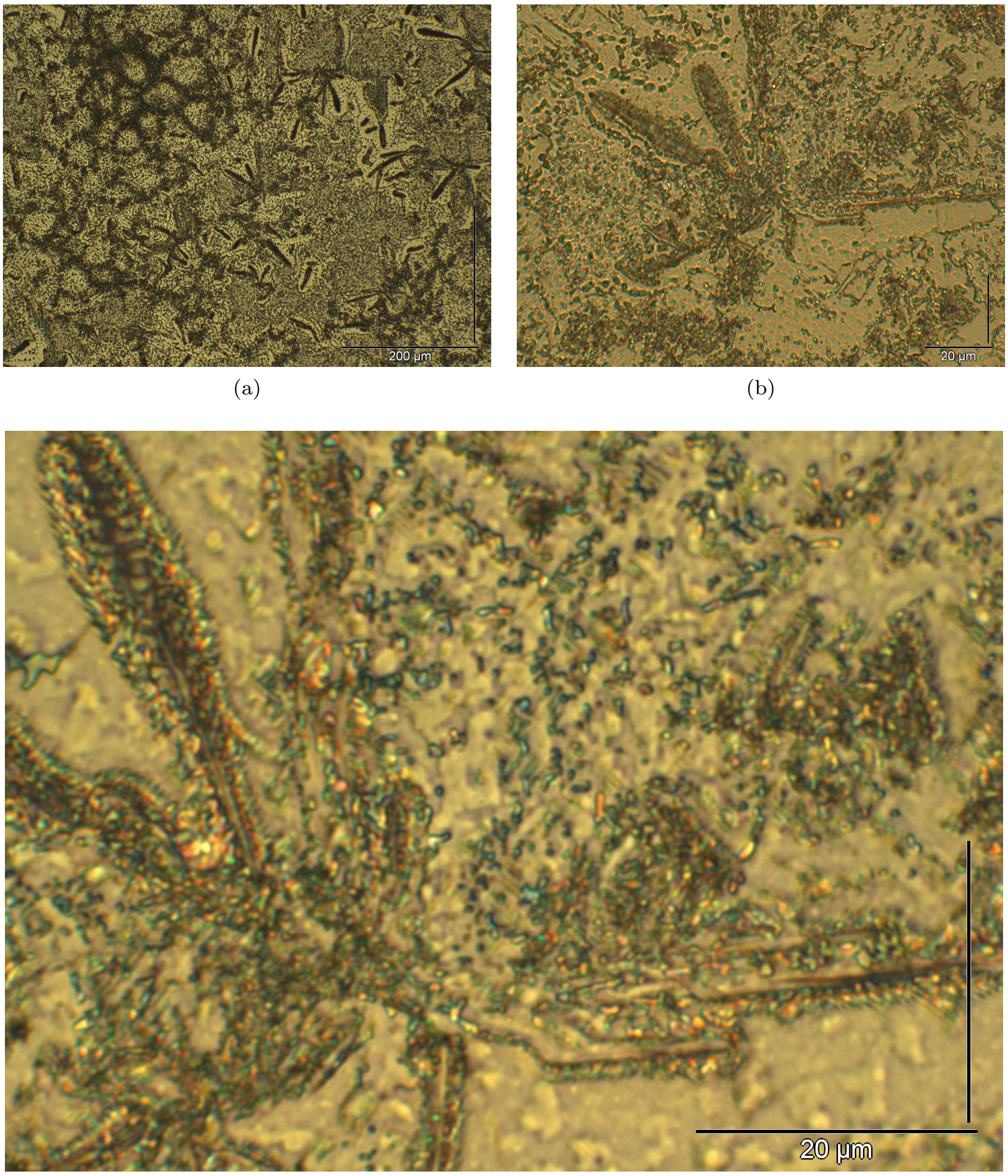

(a) (b)

(c)

Figure D.16

D.2.4 100 nm Ti, 100 nm Au

Annealing time: 15 min.

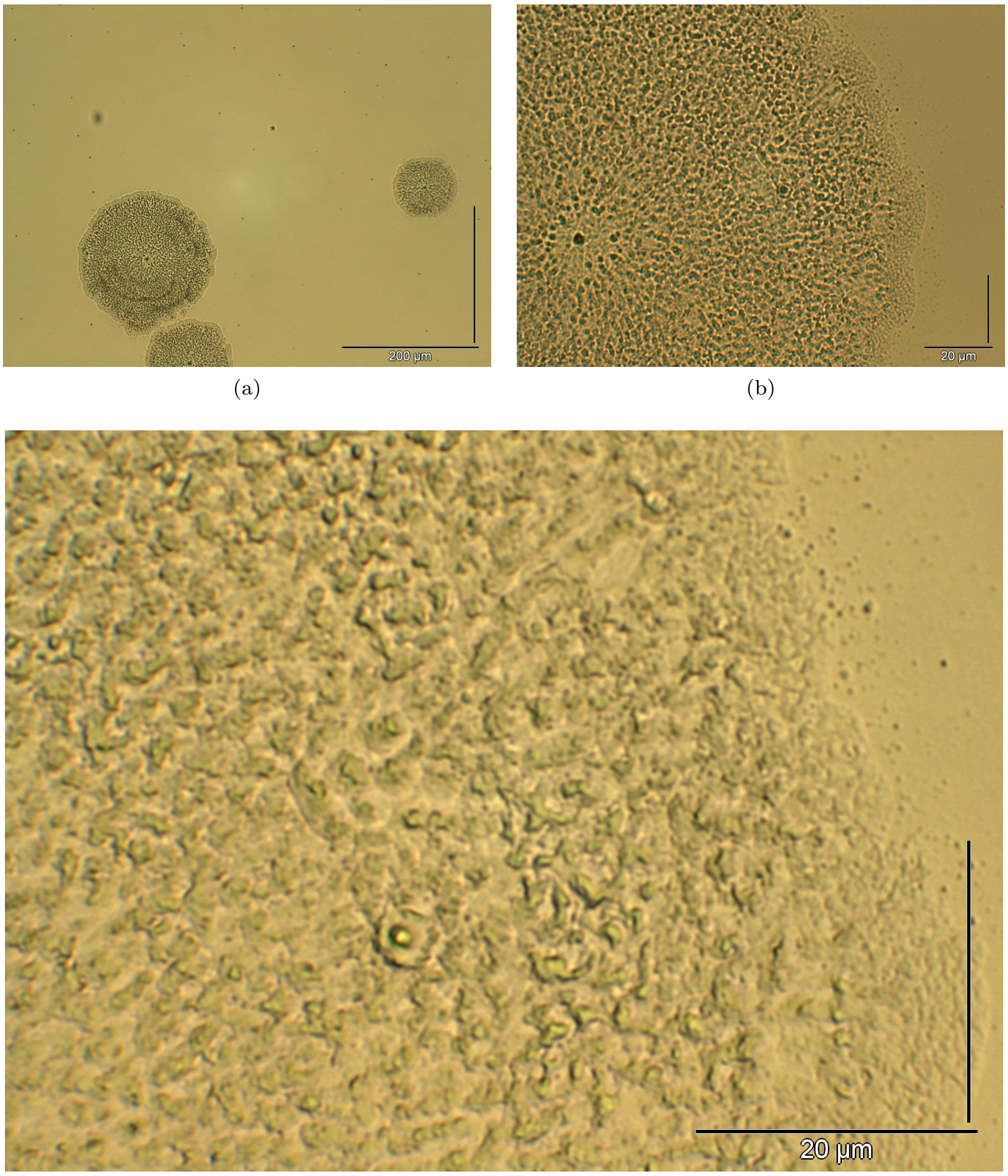

(a) (b)

(c)

Figure D.17

Annealing time: 30 min.

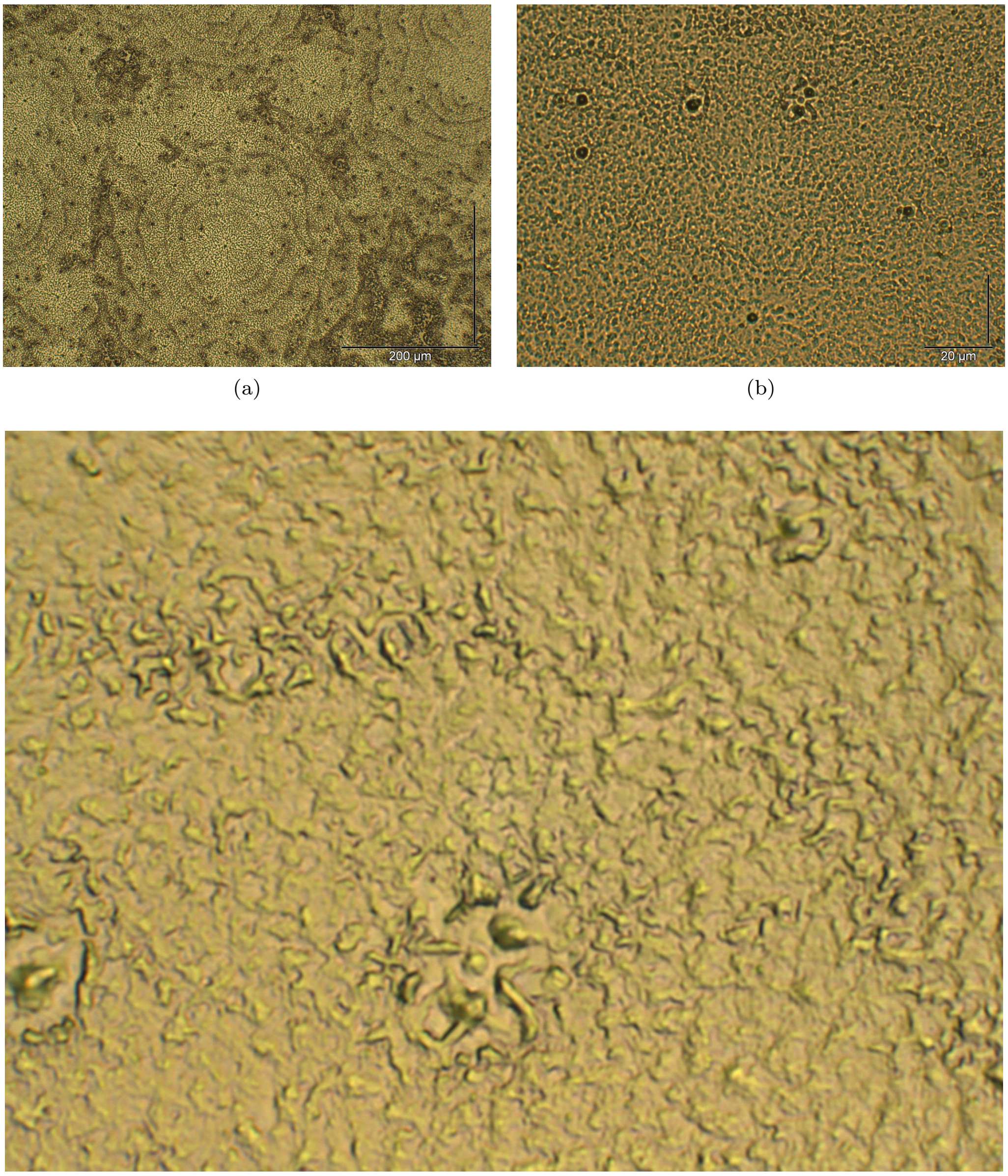

(a) (b)

(c)

Figure D.18

Annealing time: 170 min.

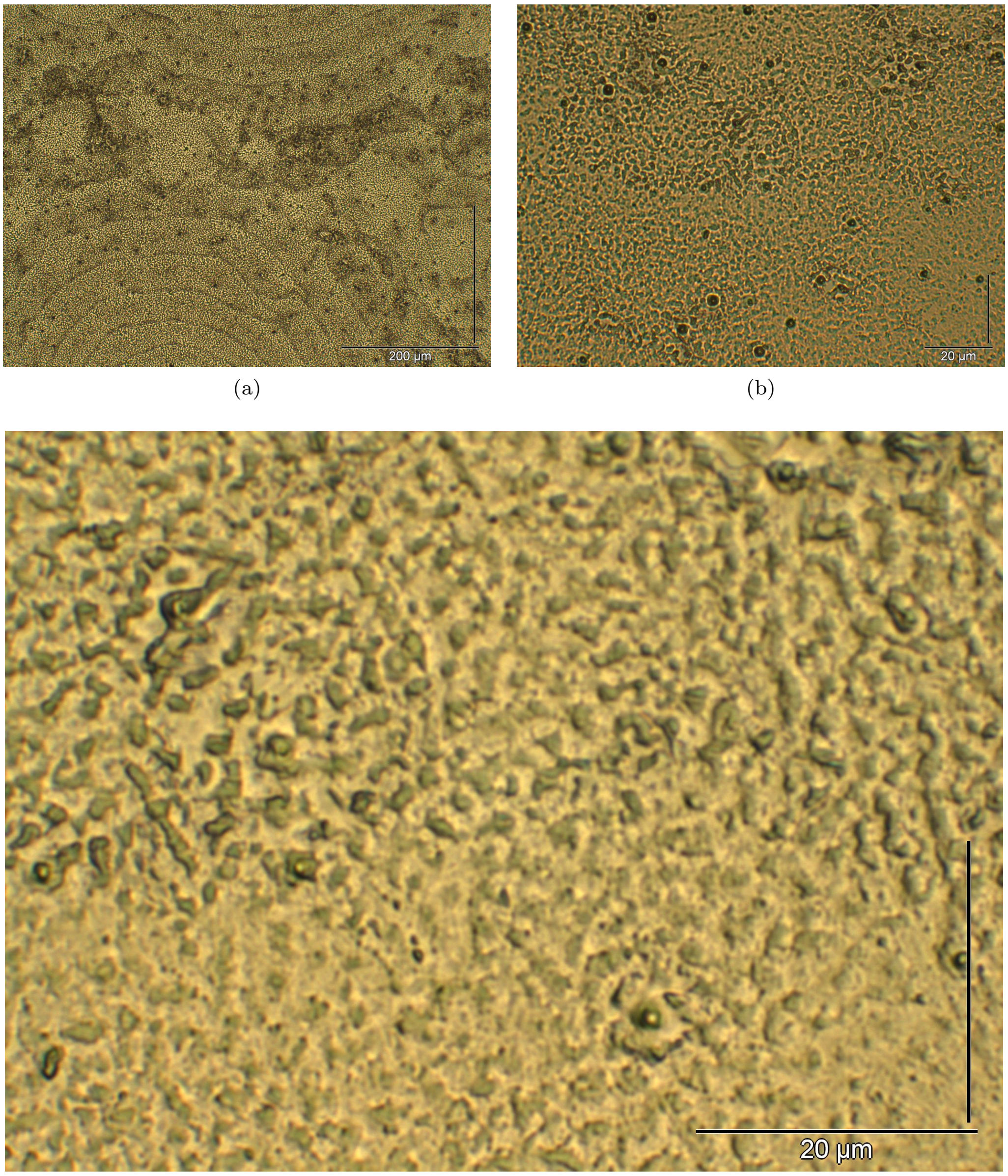

(a)

(b)

(c)

Figure D.19

D.2.5 10 nm Cr, 100 nm Au

Annealing time: 15 min.

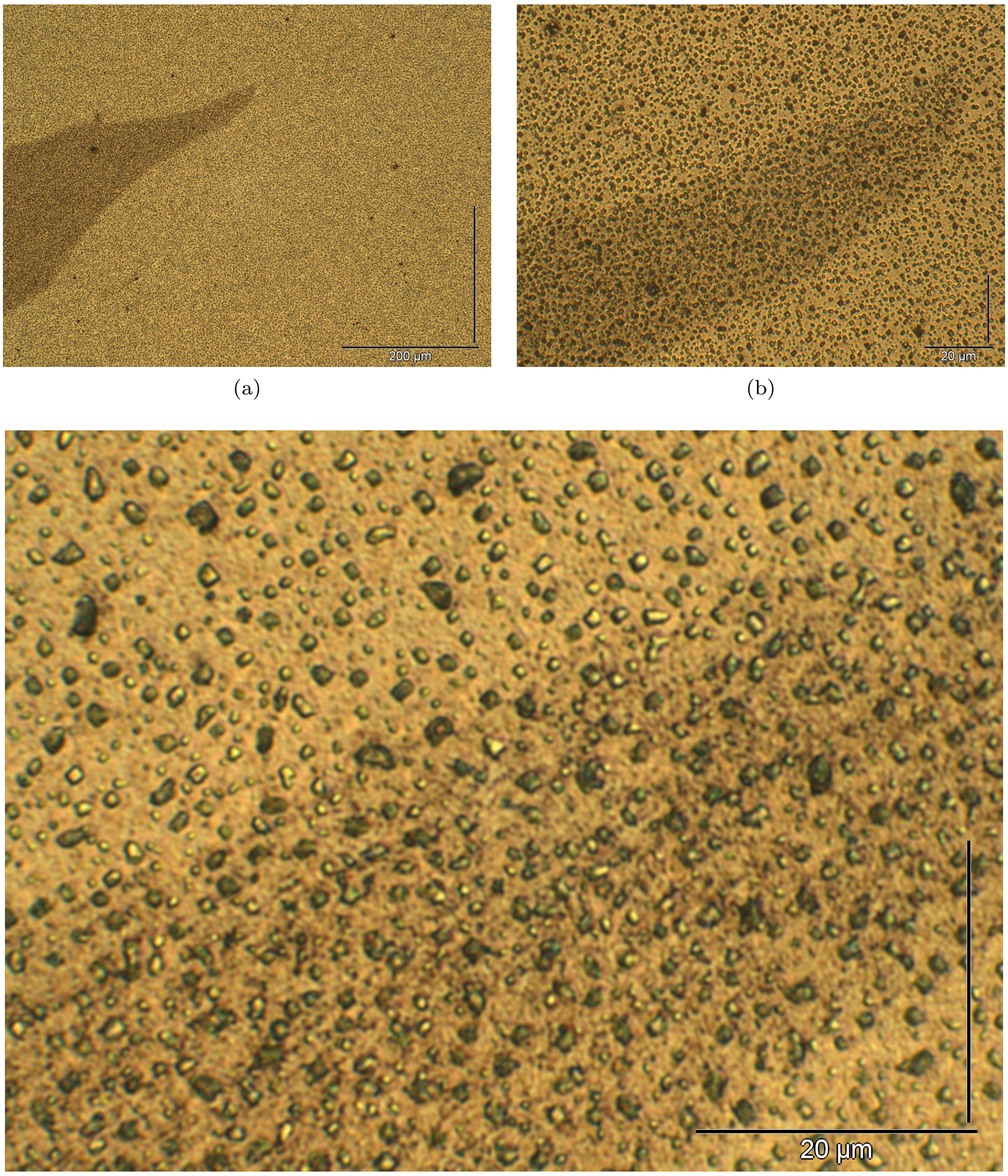

(a) (b)

(c)

Figure D.20

Annealing time: 30 min.

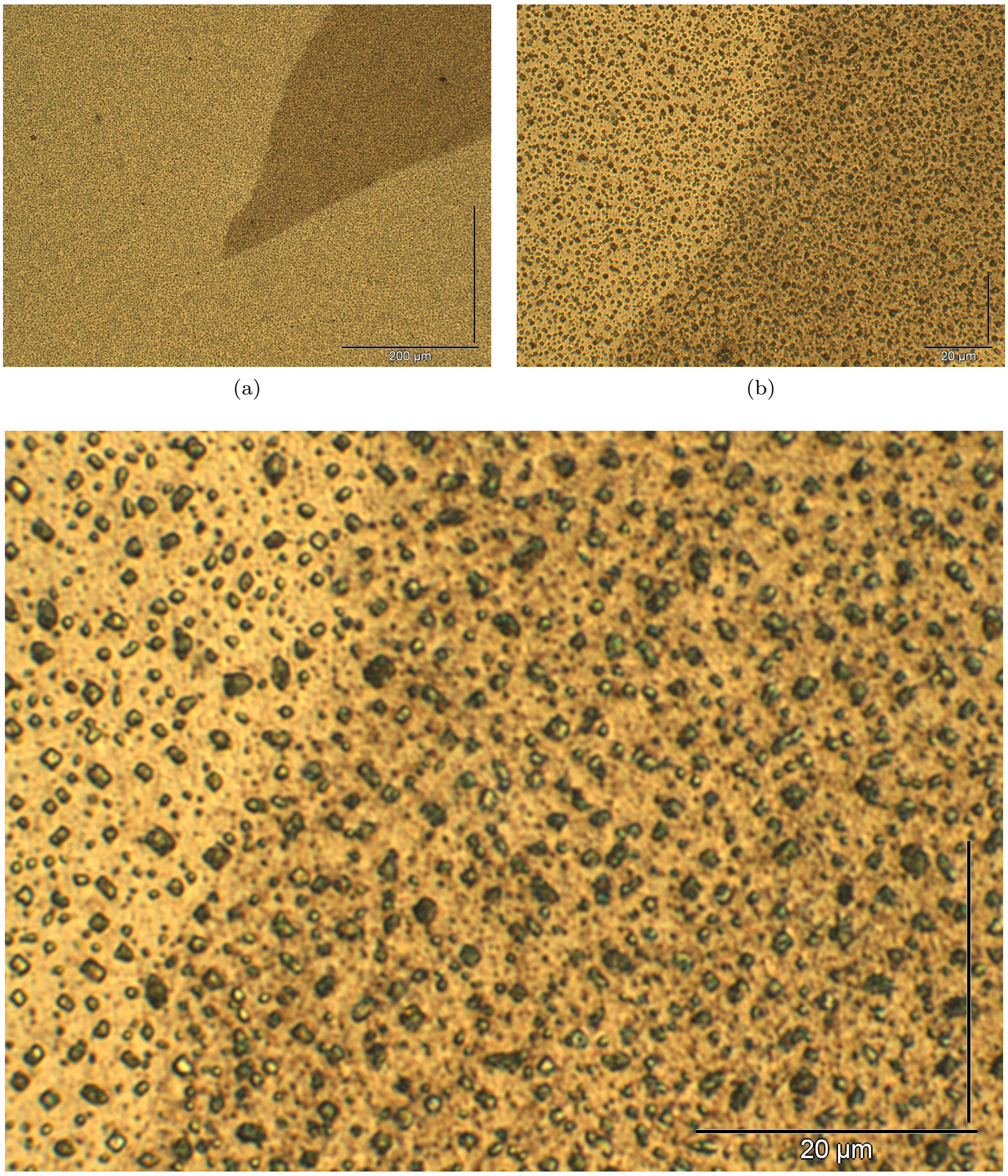

(a)

(b)

(c)

Figure D.21

Annealing time: 170 min.

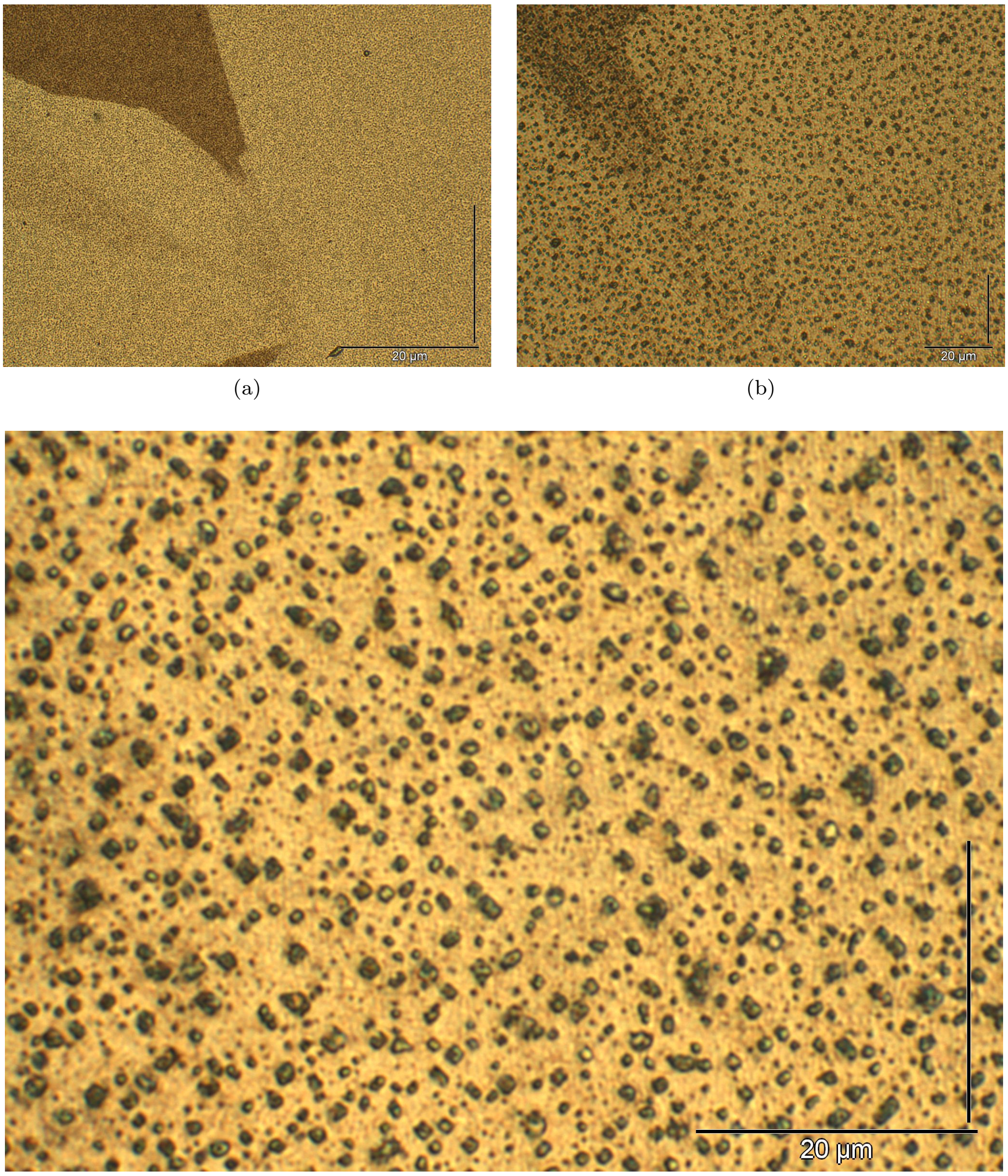

(a) (b)

(c)

Figure D.22

D.2.6 50 nm Cr, 100 nm Au

Annealing time: 15 min.

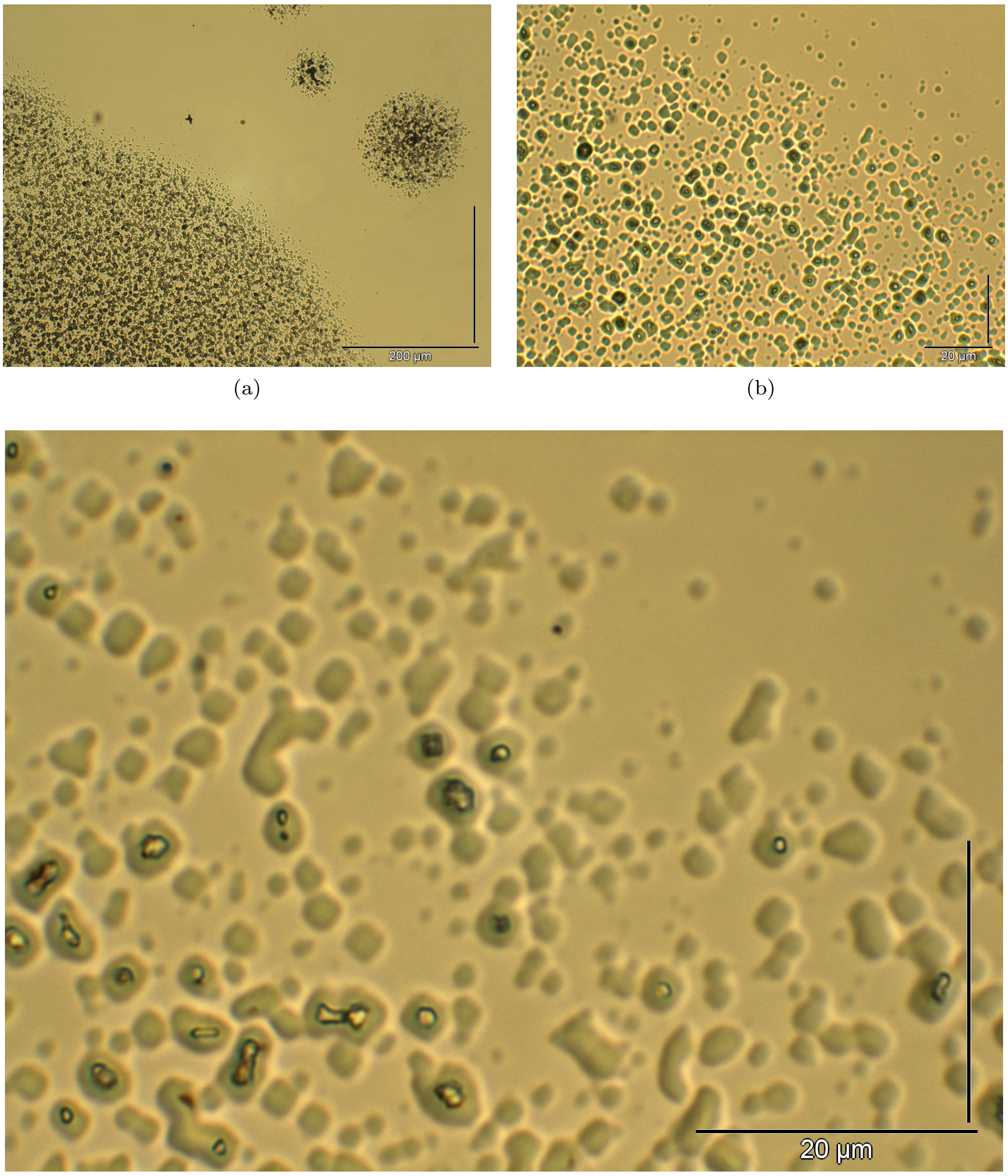

(a) (b)

(c)

Figure D.23

Annealing time: 30 min.

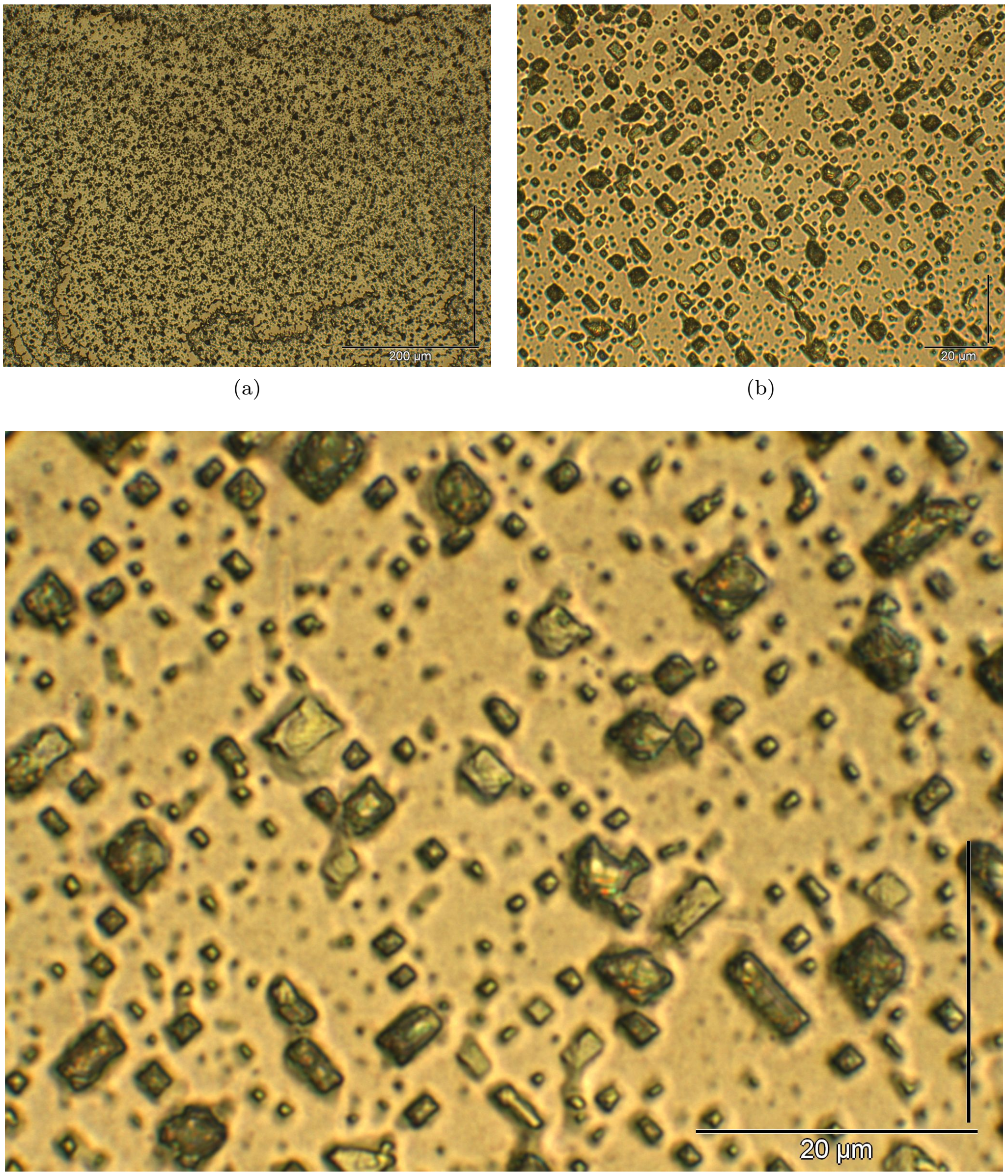

(a) (b)

(c)

Figure D.24

Annealing time: 170 min.

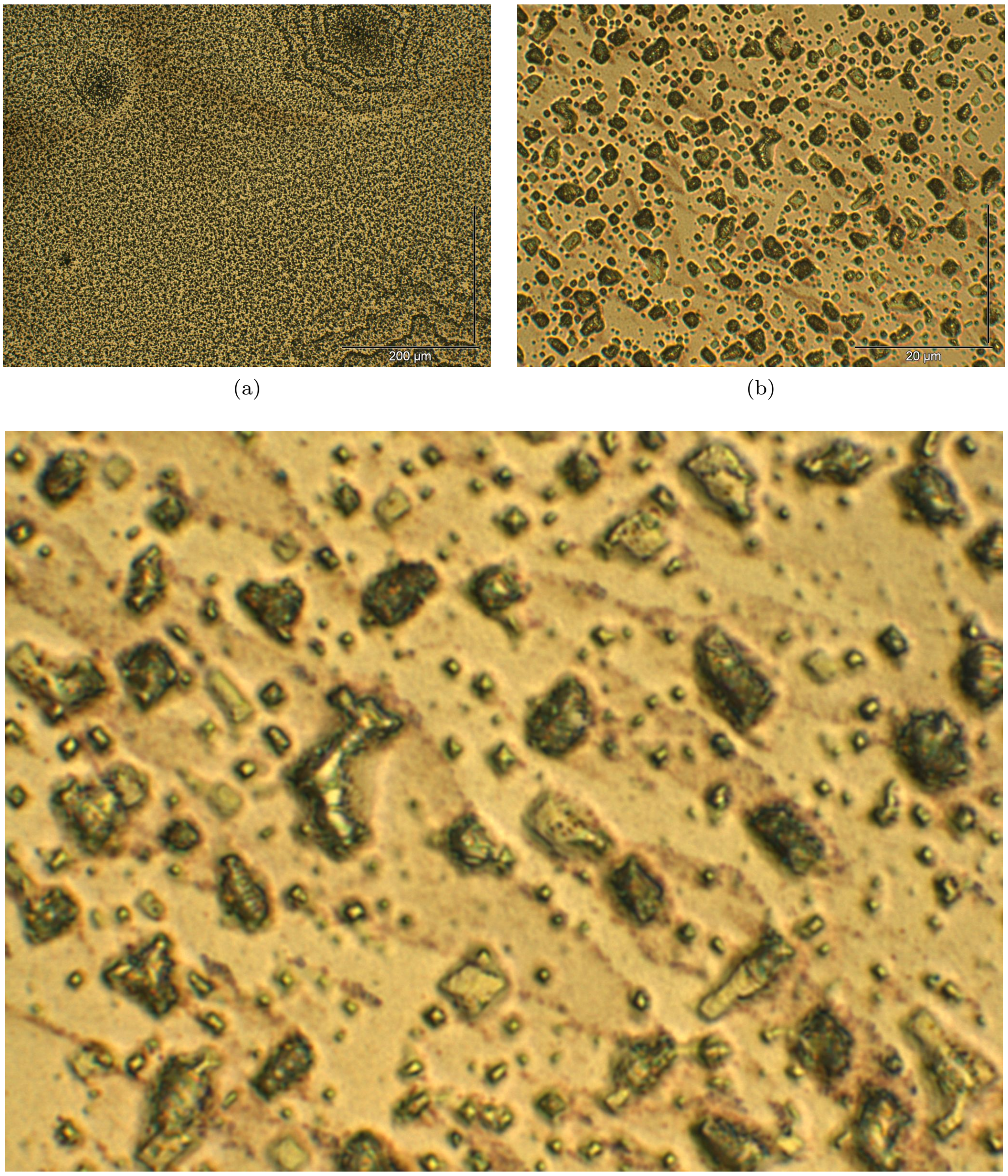

(a) (b)

(c)

Figure D.25

D.2.7 100 nm Cr, 100 nm Au

Annealing time: 15 min.

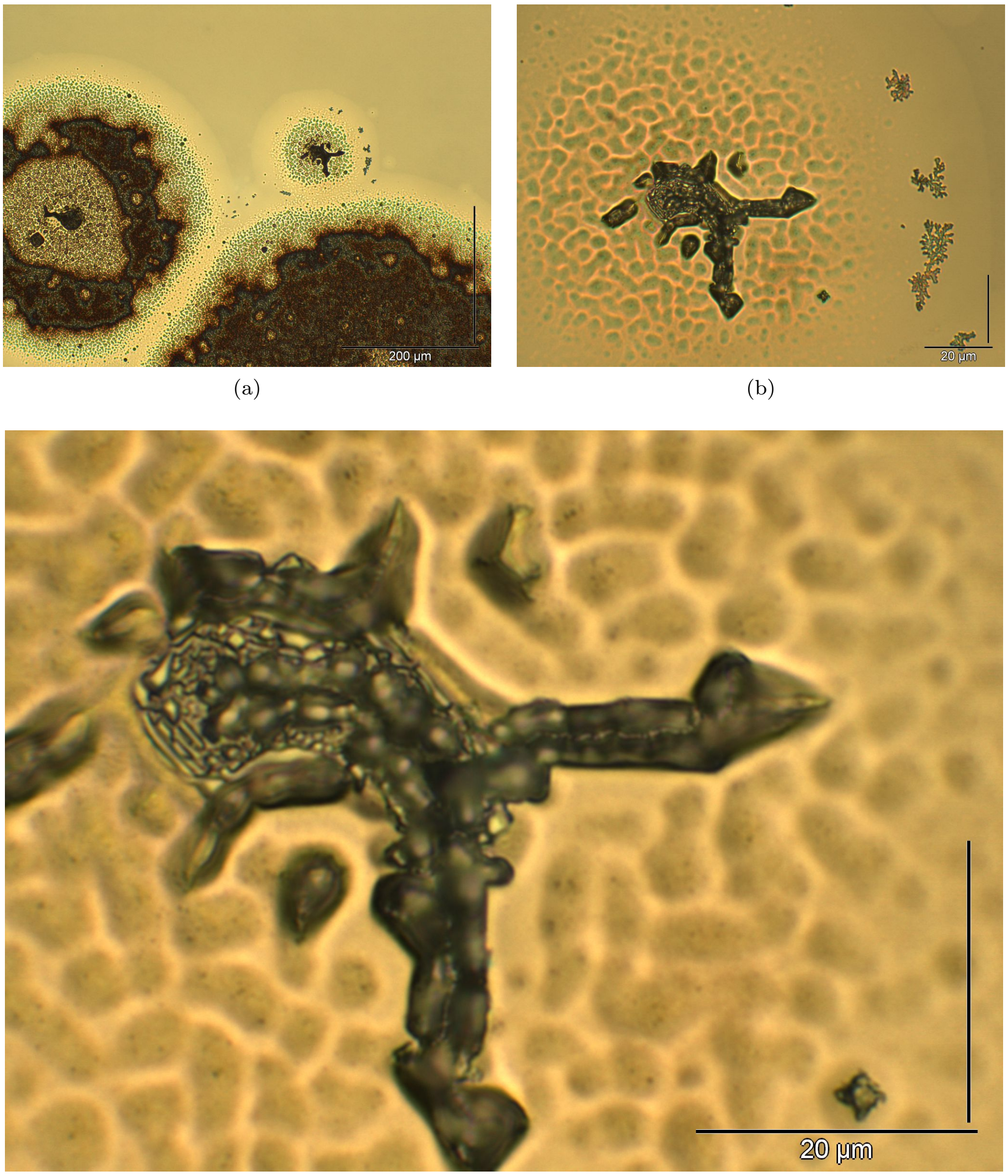

(a) (b)

(c)

Figure D.26

Annealing time: 30 min.

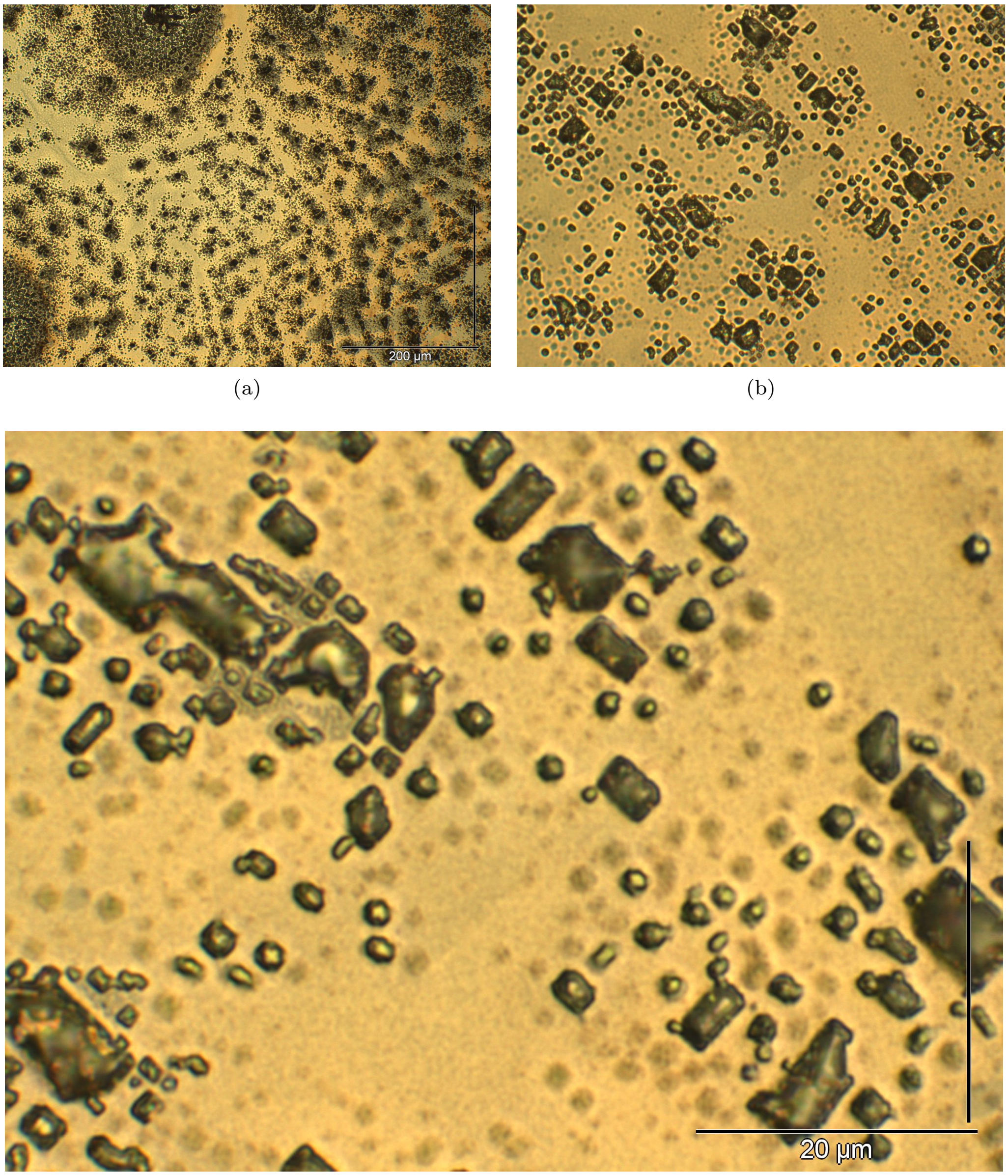

(a)

(b)

(c)

Figure D.27

Annealing time: 170 min.

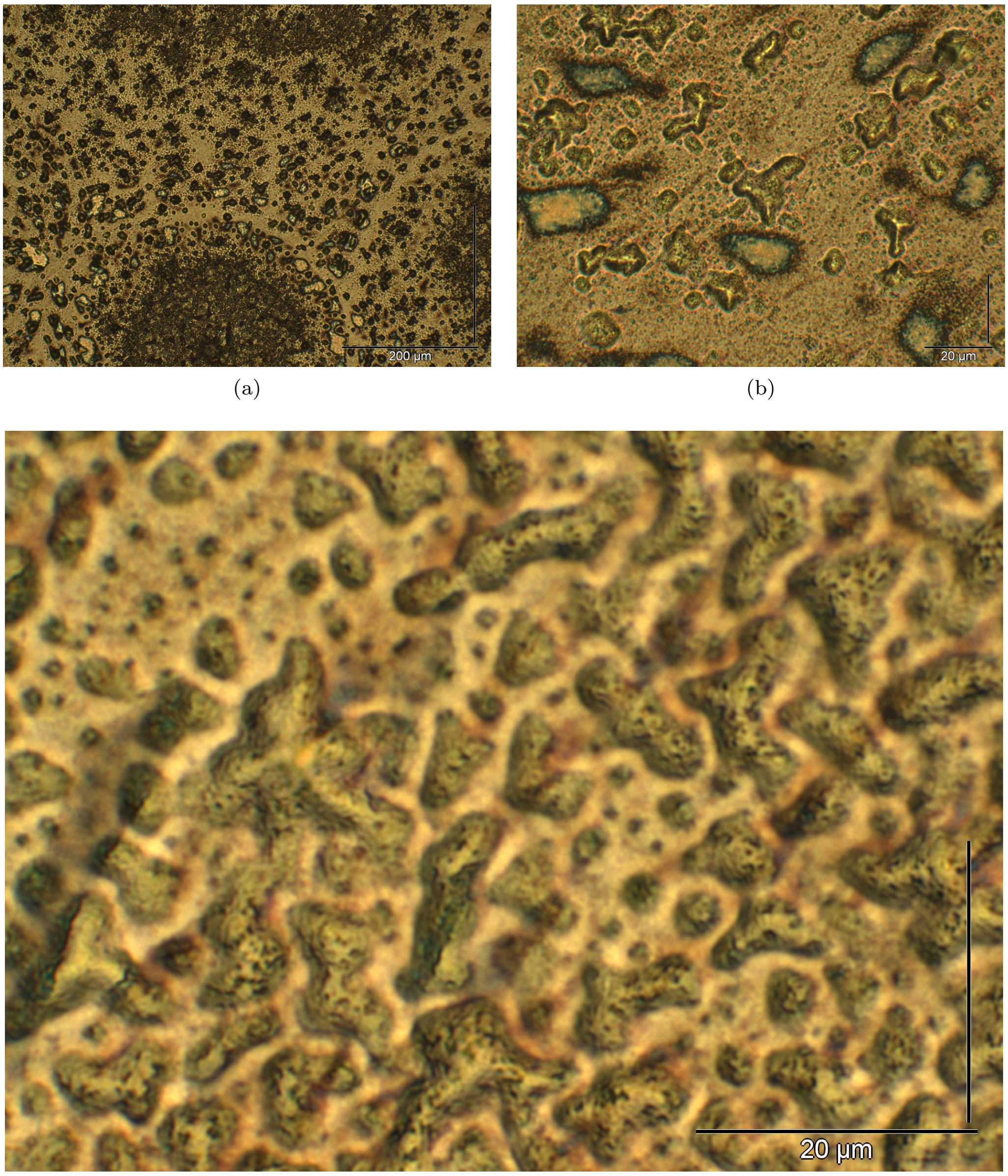

(a)

(b)

(c)

Figure D.28

Appendix E

Pull-bench data

Sample	Pillars	Radius [μm]	Fracture force [N]	Fracture stress [MPa]
B3	100	35	13,8	35,9
B6	100	35	34,2	88,9
E6	100	35	46,2	120
E8	100	35	3	7,80
C1	196	35	115	152
D3	196	35	60	79,5
G6	196	35	82,6	110
H6	196	35	19	25,2

Table E.1: 100 nm Au

Sample	Pillars	Radius [μm]	Fracture force [N]	Fracture stress [MPa]
E1	100	35	30,5	79,3
E3	100	35	33,2	86,3
E6	100	35	40,5	105
E8	100	35	45,5	118
B6	100	35	43,5	113
B3	100	35	46,6	121
C1	196	35	67,5	89,5
D3	196	35	74,9	99,3
D6	196	35	85	113
G6	196	35	50	66.3
H6	196	35	92,5	123

Table E.2: 10 nm Ti, 100 nm Au

Sample	Pillars	Radius [μm]	Fracture force [N]	Fracture stress [MPa]
E1	100	35	20	52,0
E3	100	35	20,3	52,7
E6	100	35	4,4	11,4
B3	100	35	32,1	83,4
E5	100	25	4,4	22,4
B5	100	25	6,31	32,1
D3	196	35	72,8	96,5
C1	196	35	49,3	65,4
G3	196	35	69	91,5
H6	196	35	64,6	85,6
G6	196	35	67,2	89,1
D5	196	25	26	67,6
G5	196	25	35,6	92,5

Table E.3: 50 nm Ti, 100 nm Au

Sample	Pillars	Radius [μm]	Fracture force [N]	Fracture stress [MPa]
E1	100	35	13,7	35,6
E3	100	35	20,4	53,0
E6	100	35	7	18,2
E8	100	35	1	2,6
B6	100	35	25,6	66,5
B3	100	35	28,1	73,0
C1	196	35	36,6	48,5
D3	196	35	95,9	127
D6	196	35	46,4	61,5
G6	196	35	32,9	43,6
H6	196	35	76,6	102

Table E.4: 100 nm Ti, 100 nm Au

Sample	Pillars	Radius [μm]	Fracture force [N]	Fracture stress [MPa]
E1	100	35	28,7	74,6
B3	100	35	19,8	51,4
B6	100	35	20	52,0
E6	100	35	30,8	80,0
E8	100	35	24	62,4
H6	196	35	43,1	57,1
G6	196	35	33,3	44,1
G3	196	35	45,8	60,7
D3	196	35	57	75,6
C1	196	35	42,8	56,7

Table E.5: 10 nm Cr, 100 nm Au

Sample	Pillars	Radius [μm]	Fracture force [N]	Fracture stress [MPa]
B6	100	35	39,6	103
B3	100	35	48,2	125
E3	100	35	28,2	73,3
E6	100	35	35	90,9
D6	196	35	105	139
H6	196	35	63,9	84,7
C1	196	35	93,4	124

Table E.6: 50 nm Cr, 100 nm Au

Sample	Pillars	Radius [μm]	Fracture force [N]	Fracture stress [MPa]
E1	100	35	34,6	89,9
B3	100	35	4,6	12,0
B6	100	35	1	2,6
E6	100	35	1	2,6
E8	100	35	13,8	35,9
H6	196	35	32,5	43,1
G6	196	35	38,5	51,0
G3	196	35	27,9	37,0
D3	196	35	12,7	16,8
C1	196	35	30,5	40,4

Table E.7: 100 nm Cr, 100 nm Au

Appendix F

Advanced bond strength surfaces

F.1 100 nm Au

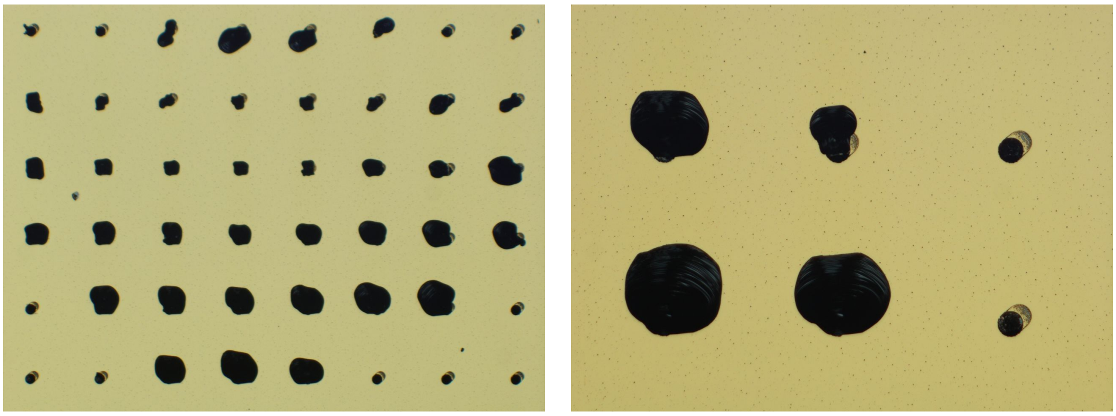

(a) (b)

Figure F.1: Sample B6 (a) 2.000 x; (b) 5.000 x.

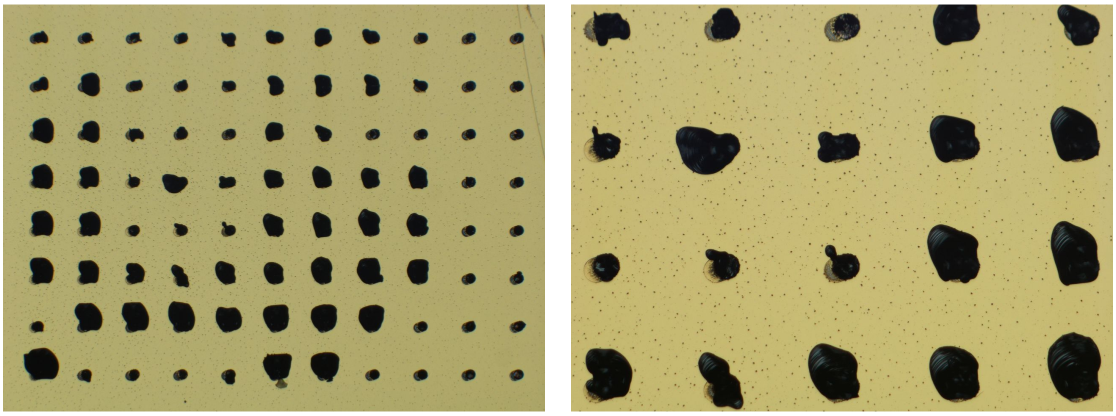

(a) (b)

Figure F.2: Sample G3 (a) 2.000 x; (b) 5.000 x.

F.2 10 nm Ti, 100 nm Au

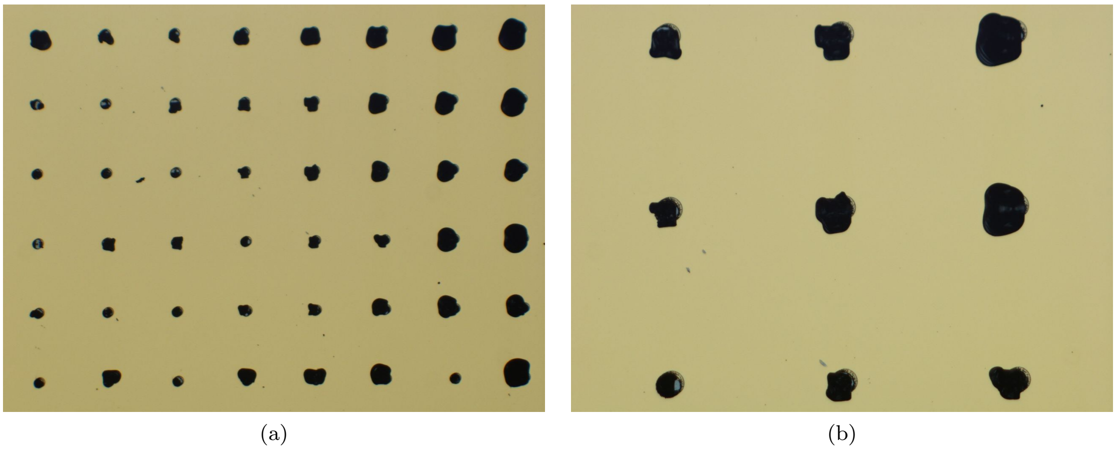
(a) (b)

Figure F.3: Sample B6 (a) 2.000 x; (b) 5.000 x.

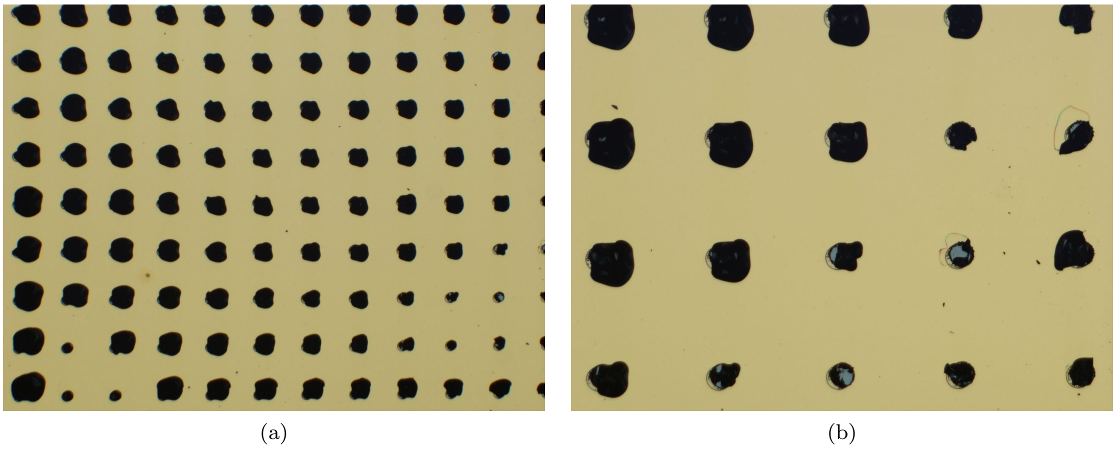
(a) (b)

Figure F.4: Sample G3 (a) 2.000 x; (b) 5.000 x.

F.3 50 nm Ti, 100 nm Au

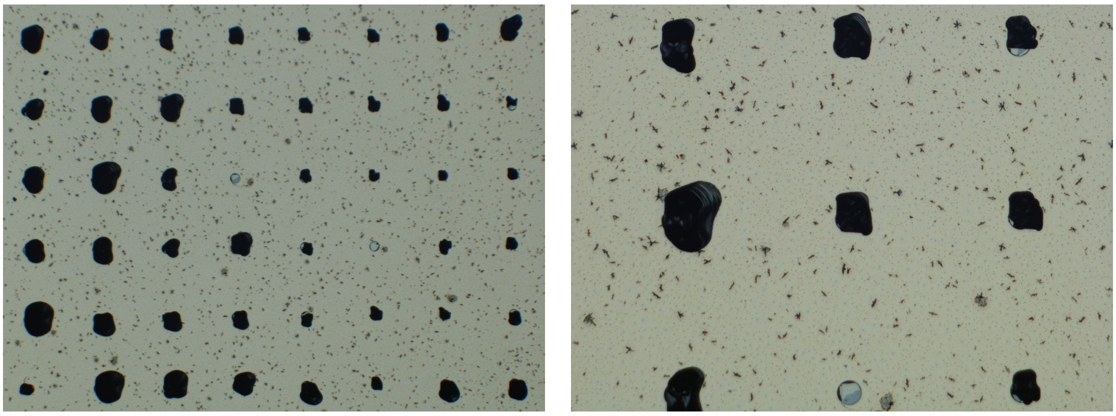

(a) (b)

Figure F.5: Sample B6 (a) 2.000 x; (b) 5.000 x.

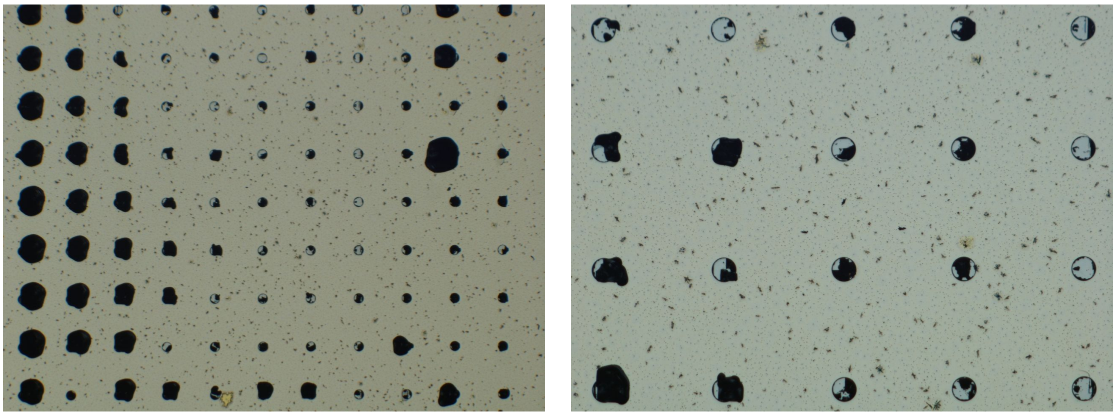

(a) (b)

Figure F.6: Sample G3 (a) 2.000 x; (b) 5.000 x.

F.4 100 nm Ti, 100 nm Au

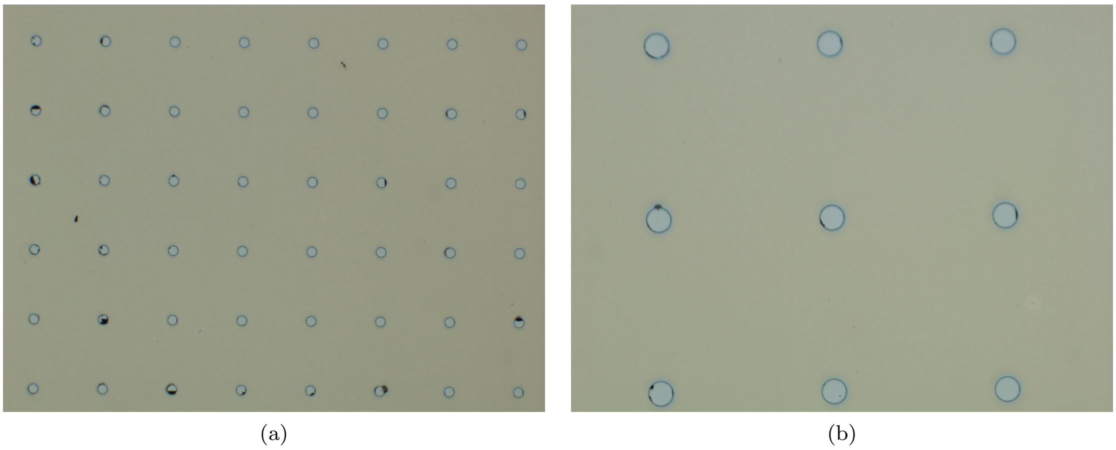
(a) (b)

Figure F.7: Sample B6 (a) 2.000 x; (b) 5.000 x.

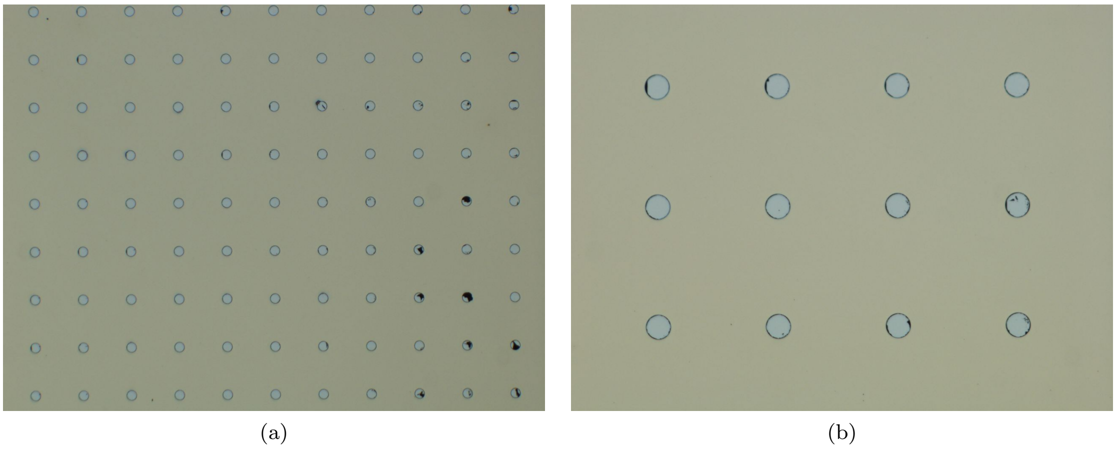
(a) (b)

Figure F.8: Sample G3 (a) 2.000 x; (b) 5.000 x.

F.5 10 nm Cr, 100 nm Au

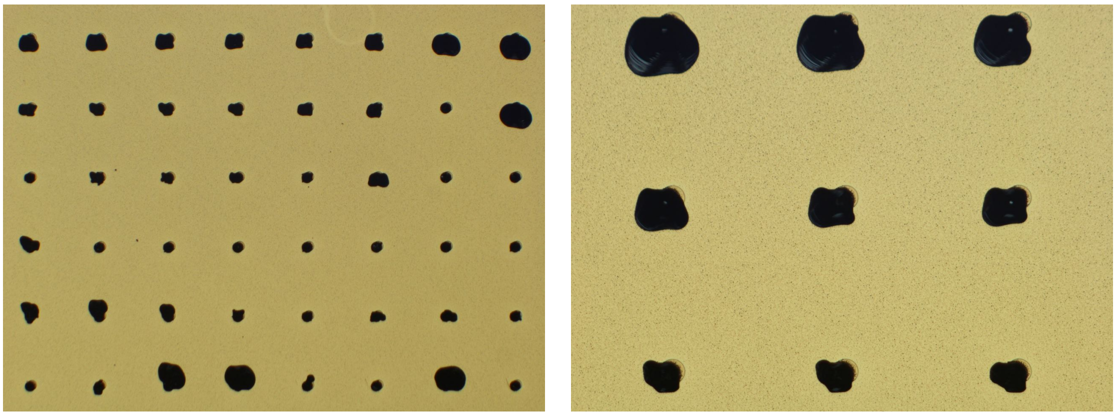

(a) (b)

Figure F.9: Sample B6 (a) 2.000 x; (b) 5.000 x.

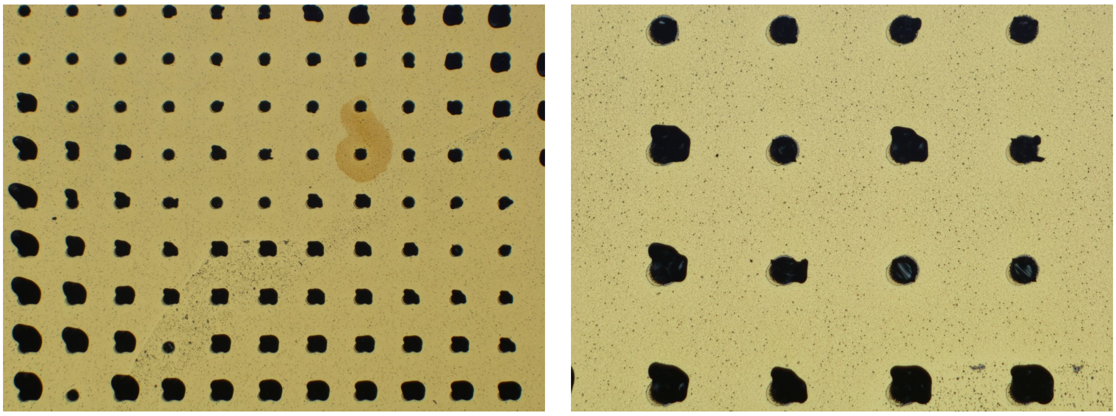

(a) (b)

Figure F.10: Sample G3 (a) 2.000 x; (b) 5.000 x.

F.6 50 nm Cr, 100 nm Au

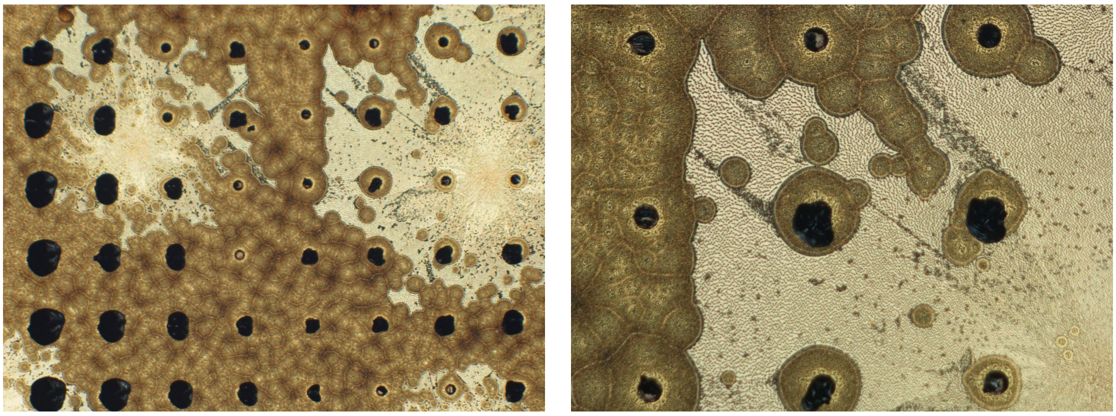

(a) (b)

Figure F.11: Sample B6 (a) 2.000 x; (b) 5.000 x.

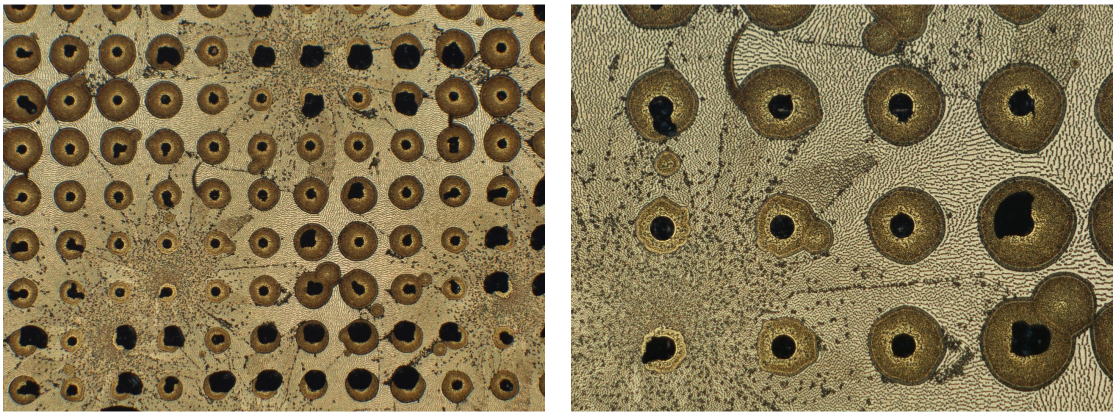

(a) (b)

Figure F.12: Sample D2 (a) 2.000 x; (b) 5.000 x.

F.7 100 nm Cr, 100 nm Au

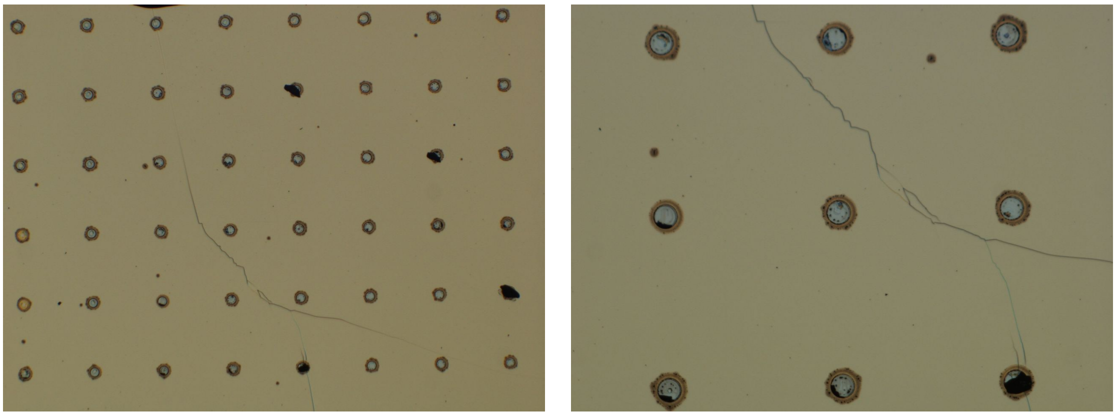
(a) (b)

Figure F.13: Sample B6 (a) 2.000 x; (b) 5.000 x.

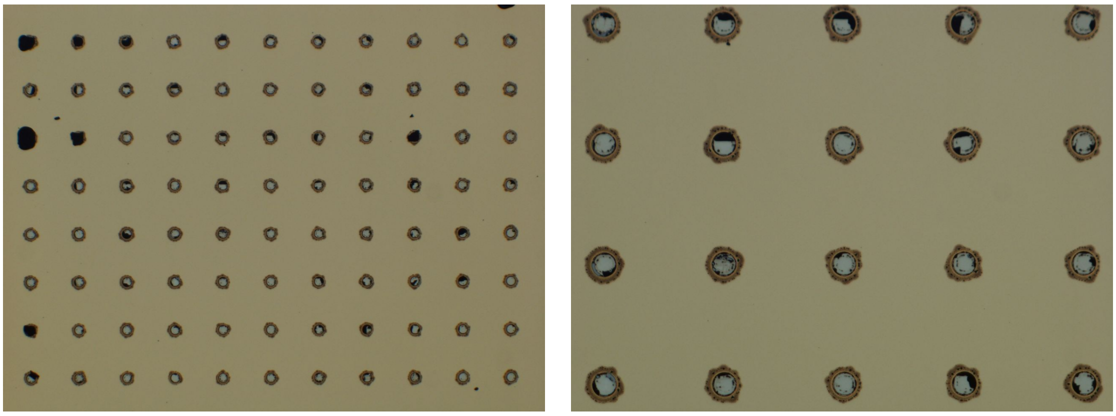
(a) (b)

Figure F.14: Sample G3 (a) 2.000 x; (b) 5.000 x.